Unfolding Piecewise-Smooth Dynamics in a Single Inductor Multiple-Output Switching Converter

by

Vanessa Moreno Font

Thesis Supervisor:

Luis Benadero García-Morato

June 2009

Technical University of Catalonia (UPC)

To my husband

and

friends.

Acknowledgements

Abstract

Switching power converters are known to be appropriate solutions to supply energy to electronic devices owing to their high efficiency and low cost. Their extensive use in the last decades has motivated researches to improve their designs and to go deeply into the comprehension of their behavior which, like most power electronic devices, exhibit nonlinear dynamics. More recently, electronic equipments containing multiple loads have been arisen such as PDA, mobile phones, MP3... These applications frequently require multiple supplies with different polarities. Single-Inductor Multiple-Input Multiple-Output (SIMIMO) switching dc-dc converters are becoming as solutions to supply low power devices as LCD displays and to charge batteries due to the significant reduction of size because the use of a single inductor.

The inherent switching nature of these systems classifies their dynamics into the field of Variable Structure Systems (VSS), which are also known as Piecewise-Smooth (PWS) systems. Due to the fact that their dynamics cannot be completely explained with the classical smooth theory, in the last years a lot of effort has been addressed towards the research on a theory of non-smooth dynamics motivated by different fields of application.

This dissertation deals with the dynamical characterization of SIMIMO converters, which can help us to prove their viability. Two strategies of control, both of them based on the widely used Pulse Width Modulation (PWM) control, are discussed. In the first alternative, the control is used to regulate a Two-Input Two-Output (SITITO) converter with opposite polarity. The two required modulating signals are generated synchronizely. This strategy of PWM control is called in this work Single Phase Control (SPC) in contrast to a second strategy, which is noted here as Interleaved Control (IC), capable of driving a generalized single inductor multiple-input multiple-output converters. This control is based on the use of various modulating signals, equal to the number of outputs, which are progressively time delayed.

The dynamics of the SIMIMO converters, just like of the basic dc-dc converters, presents a rich variety of nonlinear phenomena, which covers from smooth bifurcations, such as period-doubling, Saddle-Node or Hopf bifurcations, to non-smooth bifurcations. After proving the existence of stable dynamics if appropriate parameters are selected, this dissertation will deal with the investigation of models to analyze the complex dynamics of the converter in a wide range of parameters. Several models are proposed and analyzed in this work. Averaged models, from which slow scale instability condition can be determined, and discrete-time models, able to prove fast scale instabilities, are used in a complementary way. Besides this, several approaches of these models will be established and validated. Their usefulness will be proved not only in the prediction of the stability, but also in the characterization of the non-smooth bifurcations presents in this converter. It will be shown that simple one-dimensional Piecewise-Linear (PWL) models provide analytical expressions for the existence and stability conditions of fixed points of the discrete-time models. Furthermore, higher dimensional maps are developed to improve the accuracy of the predictions obtained by means of one-dimensional maps and averaged models.

The discrete-time analysis of a SITITO converter driven by each of the two strategies of control has revealed that its dynamics can be modeled by a PWL map with three trams in a specific range of parameters. To our best knowledge, the literature on PWL maps includes continuous and discontinuous maps but is limited to two trams. Therefore, this dissertation is a contribution in the field of non-smooth dynamics in base to the unfolding of specific dynamics of three-piece maps.

Concerning the IC control, a generalized analysis of the stability is obtained for a SIMIMO converter with a generic number of loads. The stability analysis of the one-dimensional model has revealed the existence of a type of non-smooth bifurcation, which has been classified in this dissertation as a non-smooth pitchfork owing to the appearance of two new fixed points after undergoing the bifurcation. Detailed analysis in higher dimensional maps associates this bifurcation to a Neimark-Sacker, whose existence cannot be predicted by averaged models.

This dissertation also includes some experimental results obtained with a SITITO dc-dc converter prototype, to validate some of the scenarios found in the analysis.

Contents

List of Figures

List of Tables

Chapter 1

Introduction

1.1 Motivation

Nowadays, switching power converters are widely used in electronic devices as power supplies, motor controls, light controls, etc. Their benefits rely in their high efficiency, in contrast to linear amplifiers, jointly with their small size and low cost. This fact has motivated the research of different strategies of control and the study of the dynamics of the switching converters in different forms of energy transformation: AC/AC, AC/DC, DC/AC and DC/DC.

The simplest configurations of dc-dc switching converters are based on the transference of energy from an unregulated source to an inductor and from this to the load. The buck, boost and buck-boost are illustrations of these simple switching regulators (see Fig. 1.1). The buck or step-down converter reduces the output voltage regarding to the source while the boost or step-up converter increases this voltage. The buck-boost permits the regulation of lower and higher voltages, although in the simplest configuration the output voltage is inverted. They permit the conversion of the energy from one level to another avoiding, theoretically, losses in their components. Thus, the aim of the regulation is to force the averaged output voltage to a desired value in presence of external disturbances. This conversion can carry an increase or decrease in the input source, including a feasible inversion of its polarity. The regulation is achieved by alternating suitably the operation of the converter between two topologies, by means of a controlled switch S (ON or OFF). In addition, the presence of diodes in the circuitry of the converters forces the inductor current to be positive. Hence, the converter operates in Discontinuous Conduction Mode (DCM) when the inductor

(a) Buck

(b) Boost

(c) Buck-Boost
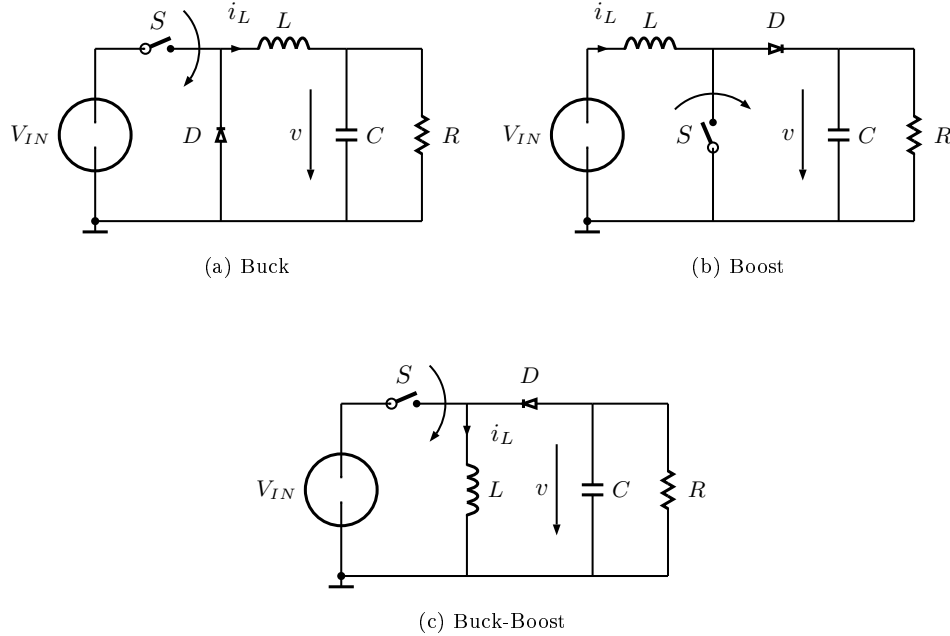
Figure 1.1. Schematics of the three basic power dc-dc converters.

current drops to 0 during the switching cycle. Otherwise, the converter is said to be operating in Continuous Conduction Mode (CCM).

The most extended strategy of control used in the literature is the Pulse Width Modulation (PWM) [64, 69, 83], whose structure includes the following elements: an external clock fixing the switching period, a sawtooth signal synchronized with the clock, an output voltage error obtained as a linear combination of the capacitor voltage and the inductor current and a comparator, whose inputs are the voltage error and the sawtooth signal. The resulting control signal of this comparator determines the duty cycle of the controlled switch S, which is defined as the ratio of the ON state to the period of an external modulated signal T.

Two approaches of PWM control are commonly used in dc-dc converters: Voltage Mode Control (VMC) and Current Mode Control (CMC). In the first case, the regulation is reached directly as the result of the comparison between the voltage error and the sawtooth signals, which will establish the state ON or OFF of the switch. Conversely, in CMC the inductor current is added to the feedback thus forcing the addition of a bistable flip-flop to avoid sliding dynamics.

Besides the basic dc-dc switching regulators, converters including more complex configurations have been emerged, which include multiple active components [19, 54, 36, 53, 12]. Converters composed by multiple cells (multi-cell converters) can supply high voltages regarding to the input source [42, 99]. There exists another group of converters composed by parallel connections of the same elemental converter, which allow supply high current in the loads [60, 59]. In most applications, only a single stabilized output is required. Nevertheless, recent applications as mobile phones, MP3 players PDA and GPS often include several loads as LCD displays, memories, universal series bus (USB) or hard drives, whose operation require different voltages. These requirements could be solved by using several independent dc-dc converters, which lead to an increment in the number of magnetic components and switches.

Conversely, in the range of lower power applications a new structure that uses a single inductor shared by several outputs is now emerging. These Single-Inductor Multiple-Input Multiple-Output (SIMIMO, also known as SIMO in the literature) converters are useful when multiple outputs must be regulated and, despite the management of low power, a high efficiency is also required. From 2001, there exist some different registered patents of dc-dc converters using a single inductor. Moreover, some integrators using this kind of converter have been commercialized: Texas Instruments (TPS65136), which are used in AMOLED displays of mobile phones or SmartPhone devices, and Maxim (MAX685) for components of digital cameras, camcorder and notebooks. Different topologies of SIMIMO converters exist depending on the combination of elemental converters and control [75, 67, 100, 95, 104]. Concerning the regulation of the converter, the simplest strategy is based on time multiplexing [79, 80], which assigns an active interval for each channel. Nevertheless, in order to guarantee the stability and avoid the regulation interference among channels, the converter must operate partially in DCM in the time interval associated to every channel. As a result, each output is independently controlled despite sharing the inductor. A pseudo-continuous conduction mode is proposed in [78], which uses a constant value for the inductor current to operate in CCM. Besides the analog controls mentioned, in [103] a digital control is proposed to regulate the converter is CCM which reduces the cross-regulation problem.

Finally, the control proposed in [15], based in PWM, allows the operation in CCM and permits the generalization of the control to regulate a SIMIMO converter with an arbitrary number of outputs. This thesis deals with the study of the viability of this type of converters jointly with the analysis of their dynamical behavior.

1.2 Nonlinear phenomena in power electronic converters

The dynamics of power electronics systems is known to be highly nonlinear [43]. A rich variety of phenomena, for instance subharmonics, quasiperiodicity and chaotic dynamics, has been reported in systems that include switches, saturations or even hysteresis. In particular, the operation of the switching regulators is characterized by transitions between different topologies, which classifies these systems into the group of Variable Structure Systems (VSS) also known as Piecewise-Smooth (PWS) systems. Consequently, despite the fact that each topology can be described by means of a set of smooth equations, the existence of boundaries increases the complexity of their behavior. Actually, it is known that PWS dynamics cannot be analyzed by using the well-known theory of smooth systems. Apart from the bifurcations characteristic of smooth systems, PWS systems can exhibit bifurcations which are exclusive of them. As an example, we can mention the border-collision bifurcations. There exists an extensive literature reporting the nonlinear phenomena in power electronics, including some relevant books [107, 11, 34]. A more specific literature about non-smooth phenomena can be found in Chapter 3.

Let us now present a brief review of the earlier works dealing with nonlinear phenomena in power electronics. The first focussing in power electronic converters appeared at the beginning of the Eighties. In 1980, Baillieul proved in [6] the existence of chaotic dynamics in power electronic circuits. Few years later, Brockett and Wood showed in [16] the existence of chaos in a dc-dc converter. Chua, in a special issue in [24], presents a study of chaos in power electronics.

A first analysis of these nonlinear phenomena was presented in 1988 by Hamill and Jefferies [56]. Herein, the authors showed, by means of a one-dimensional discrete-time map, the existence of subharmonics, bifurcation and chaos dynamics in a first-order PWM voltage control converter. Later, Jefferies in [63] shows that a RL-diode circuit can exhibit a great variety of nonlinear scenarios despite being characterized by simple systems. In 1989, Krein and Bass proved analytically and experimentally the existence of multiple limit cycles [70] and later the same authors reported in [71] three types of instability in dc-dc power electronic converters: unboudness, chattering and chaos. The phenomenon of hysteresis is also mentioned in the work.

In [26, 27], Deane and Hamill proved experimentally the existence of chaos in a Buck converter. Fossas and Olivar in [49] analyzed the stability by means of characteristic multipliers of the one and two-periodic orbits in the Buck converter, in which an strange attractor is shown as dynamics. In 1998 di Bernardo [32] introduces a new discrete-time map related to the asynchronous switching to identify the presence of periodic orbits and bifurcations in the basic switching regulators. The nonlinearity has also been proved in converters with sliding mode control. Calvente in 1996, showed

in [20] the existence of subharmonics and chaotic behavior in a Boost converter using this control. Later, El Aroudi in [39] included a deep analysis of the period-two orbit. The occurrence of nonlinear phenomena and chaos in switching regulators operating in DCM was reported by Tse in 1994 for buck [105] and boost [106] converters.

Concerning the non-smooth phenomena, in 1998 Yuan demonstrated in a work focussed in the Buck converter [111], that most bifurcations which were produced in dc-dc converters are due to a border-collision bifurcations. Since then, non-smooth phenomena in power electronics has attracted the attention of many researches. We can mention the works published in this decade by Banerjee in [10], where a one-dimensional discrete-time analysis is used to study the border-collision bifurcations in Buck and Boost converters. In [94], Parui presented these bifurcations in PWS maps which are two-dimensional in one side of the boundary and one-dimensional in the other. Zhusubaliyev [113] detailed the quasiperiodicity and border-collisions in a two-side PWM buck converter. We finally mention the works in [23, 13, 38, 2].

More recently, in 2008, Giaouris in [51] have reported a Filippov's method to analyze the dynamics of the switching converters, which is useful when the Poincaré map cannot be determined.

The study of the nonlinear phenomena has not been restricted to the elemental converters. This behavior has also been reported by Iu in parallel-connected buck converters [60] and parallel-connected boost converters using averaged models [61], which was also studied by Mazumder in [81]. Finally, more recently, Robert analyzes multi-cell dc-dc converters in [99].

The modelling of switching converters has evolved from two methods: averaged and discrete-time models. The averaging approach for modelling switching converters was developed in 1976 by Milddlebrok and Ćuk [82] and has been commonly used in the stability analysis of switching regulators because it provides simple expressions and makes the analysis easier. Nevertheless, it only contains information about the slow-frequency or slow-scale dynamics and thus, it is unable to predict many non-smooth phenomena. To deal with them, discrete-time models are employed to explain higher periodic orbits, quasiperiodicity or chaotic dynamics, including both existence and stability properties [35]. When the continuous time system uses a fixed frequency modulating signal, the stroboscopic or Poincaré map arises as a practical tool, retaining accurately the information of the dynamical properties of the original continuous system.

1.3 Organization and contribution of this dissertation

Taking into consideration that part of the analysis is focused in the non-smooth phenomenon, Chapter 2 presents an overview of the piecewise-smooth dynamics including the analysis of the dynamics of a piecewise continuous linear maps with two pieces. This chapter includes also a brief review of the basic concepts and bifurcations in smooth dynamical systems. Some relevant literature dealing with non-smooth systems is also provided in this chapter. The nomenclature which will be used in the following chapters is introduced here.

As it will be proved in Chapters 4 and 5, the discrete-time model which describes the dynamics of the converter is composed by three pieces in certain range of the parameters. In order to understand the possible scenarios given in this map, a three-piece piecewise-linear map is analyzed in a restricted set of parameters in Chapter 3. This contribution can be understood as an extension of the analysis of the two-piece map, which has been published in English literature in [31]. Expressions for the existence and stability of the one and two-periodic orbits will be obtained in order to determine the possible patterns of bifurcation. This work was partly realized in the University Federico II in Naples, under the supervision of professor Mario di Bernardo. The results obtained have been presented in the Spanish conference [87] and a report is still on preparation.

In Chapter 4, a Single-Inductor Two-Input Two-Output (SITITO) power electronic dc-dc converter is introduced jointly with the first strategy of control SPC. The converter is governed by means of a pulse width modulation (PWM) with a double voltage feedback, which includes a Proportional Integral (PI) term. Its dynamics is analyzed by using averaged models [14]. Moreover, several discrete-time models, one and five-dimensional, have been developed in order to understand the bifurcations produced by fast dynamics. Some relevant results will be discussed concerning the discrete analysis. Finally, the scenarios found are compared with the results obtained in Chapter 3. Part of the study developed in this chapter has been published in the international conferences [84] and [85], and the report [88].

Chapter 5 deals with the second strategy of control, which will be named Interleaved Control (IC). This control is able to drive a SIMIMO dc-dc converter which was firstly proposed in [15] and analyzed by means of averaging techniques. My contribution in this chapter includes the development of a generalized discrete-time model with different degrees of approach jointly with a generalized existence and stability analysis of the main mode of operation. The one-dimensional analysis reveals an uncommon bifurcation, which has been called non-smooth pitchfork bifurcation. Moreover, the higher dimensional map has also revealed a significant deviation in the prediction of some bifurcations. The results obtained in this chapter have been reported in the

international conferences [40] and the reports [41] and [86]. This last report is still on preparation.

In Chapter 6, several experimental measurements are provided. A prototype of SIM-IMO converter has been built in the laboratory, whose control board permits the programming of different strategies of control without the needed of any change in the power stage. This prototype has allowed us to prove the nonlinear dynamics of both controls analyzed in this dissertation.

Finally, conclusions and future works will be given in Chapter 7.

Chapter 2

Piecewise-smooth dynamical systems

The main objective of this chapter is to provide an overview of the theory of piecewise-smooth dynamical systems. Our discussion begins with a brief introduction of the basic concepts of the well-developed smooth theory, connecting then with the piecewise-smooth theory. The last part of this chapter concerns with the study and classification of the non-smooth bifurcations, which undergo in one-dimensional piecewise-linear maps.

2.1 Brief review of smooth dynamical systems

The classical theory of dynamical systems helps us to understand the behavior of dynamical systems in many areas such as physics, biology, engineering and economics. There exists a well established theory for dynamical systems sufficiently smooth reported in diverse reports and books. For instance, we can mention the books of Kuznetsov [74] and Wiggins [109]. The objective of this section is to introduce some basic nonlinear concepts and notation for the two classes of dynamical systems: flows (continuous-time) and maps (discrete-time).

Let us consider the following *vector field* or *flow* in the form of an *ordinary differential equation*

$$\dot{x} = f(x, t, \mu),$$

where $x \in \mathcal{D} \subset \mathbb{R}^n$, $t \in \mathbb{R}^1$, $\mu \in \mathcal{V} \subset \mathbb{R}^p$, t stands for the independent variable *time*, x is the vector of state variables or phases, the subset $\mathcal{D}$ is called *phase space*, being commonly $\mathcal{D} = \mathbb{R}^n$ and μ is the vector of parameters or fixed coefficients of the system.

A system that does not depend explicitly on time will be called *autonomous*.

A *trajectory* $\Phi(x_0, t)$ is said to be a solution of the flow with given initial condition x_0. A *phase portrait* refers to the set of trajectories of the flow in the phase state.

Similarly, let us consider also the following *map* or discrete-time system

$$x \mapsto g(x, \mu),$$

where $x \in \mathcal{D} \subset \mathbb{R}^n$ and $\mu \in \mathcal{V} \subset \mathbb{R}^p$.

A *map* is a dynamical system where time is discrete. They are also known as *difference equations* or *iterated maps*. Maps are used to model natural or technical phenomena such as electronics, economist and population dynamics. Nevertheless, discrete-time models can also arise from analyzing differential equations through the so-called Poincaré maps. Let us consider the following flow

$$\dot{x} = f(x),$$

where $x \in \mathbb{R}^n$. Let us also consider the $(n-1)$-dimensional surface S, which is transversal to all trajectories of f. Then, we can define the Poincaré map (see Fig. 2.1) as follows

$$P : S \to S,$$

where

$$x \mapsto P(x).$$

Despite the difficulty in finding an explicit expression of P, Poincaré maps can turn difficult problems in differential equations into easier problems. The analysis of existence and stability of limit cycles of flows is given by the study of fixed points in the Poincaré map, which is demonstrated to be equivalent.

2.1.1   Invariant sets

An invariant set can be defined as a set that evolves to itself under the dynamics. We can also define an *attractor* of a dynamical system as a subset of the state space to which orbits tend as time increases. When more than one attractor coexists in the phase space, the *basin of attraction* can be defined as the set of initial conditions leading to long-time behavior that approaches that attractor. The following list shows most important attractors in continuous-time dynamical systems:
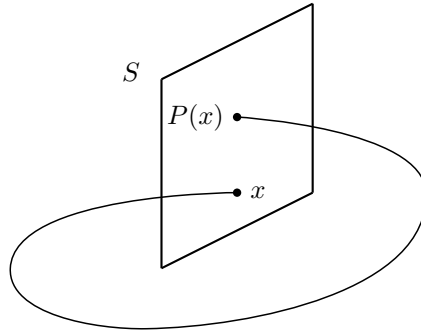
Figure 2.1. Poincaré mapping.

- **Equilibrium points**: x^* is said to be an equilibrium point of f if $f(x^*) = 0$.

- **Limit cycles**: A limit cycle corresponds to a periodic orbit with period T that satisfies $\Phi(x_0, T) = x_0$, being x_0 the initial condition and T the smallest time for which the condition is fulfilled. In the phase space, the limit cycle corresponds to a closed curve.

- **Invariant tori or quasiperiodic orbit**: This attractor contains a finite number of incommensurable frequencies. The trajectories move on the surfaces of a torus.

- **Chaos**: This behavior is characterized by having an aperiodic and, apparently, random trajectory, which is unpredictable in the long term due to its sensitivity to initial conditions.

We can mention also other invariant set as such *homoclinic* or *heteroclinic* orbits which connect a single equilibrium point with itself or two equilibrium points respectively. These invariant sets are involved in the boundary of basins of attraction.

Concerning discrete-time models, the feasible invariant sets are:

- **Fixed point**: x^* is said to be a fixed point of f if $f(x^*) = x^*$. This invariant set corresponds to a closed orbit of a flow.

- **Periodic orbit**: $(x_1^*, x_2^*, ..., x_k^*)$ is a k-periodic orbit, being $k > 0$, of the map f if $f^k(x_1^*) = x_1^*$. In fact, a n-periodic orbit is a fixed point of the nth-iteration of the map.

- **Invariant cycle**: The corresponding invariant set in flows of a torus.

- **Chaos**

It is important to remark that another advantage of the use of Poincaré maps is that the corresponding invariant sets in maps are simpler than in the continuous-time model.

2.1.2   Stability of fixed points

In order to deal with the stability of fixed points, we will consider nonlinear autonomous systems or maps sufficiently smooth. The stability is proven to be equivalent to the stability of a linearization of the system in the neighborhood of the fixed point.

Let us consider the map

$$x \mapsto P(x),$$

where $x \in \mathbb{R}^n$ with x^* as a fixed point of the map and then $x^* = P(x^*)$. Let us also consider the perturbation

$$x = x^* + \epsilon.$$

Then, for small ϵ, the map can be approached in the neighborhood of the fixed point x^* by the first term of its Taylor expansion in x^*. Therefore,

$$x^* + \epsilon' = P(x^* + \epsilon) = P(x^*) + [DP(x^*)]\epsilon + O(\|\epsilon\|^2),$$

where DP is the Jacobian matrix of P at the fixed point x^*. The element ij of the DP matrix is defined as

$$DP_{ij} = \frac{\partial P_i}{\partial x_j}.$$

Then, we obtain

$$\epsilon' \approx [DP(x^*)]\epsilon.$$

The set of *multipliers* $\{\lambda_j, \; j = 1..n\}$ of a fixed point x^* refers to the eigenvalues of the Jacobian matrix DP of the linearized map P associated at this point. The local stability of this fixed point x^* is guarantied so long as

$$|\lambda_j| < 1 \quad \forall j \in [1, n].$$

Similar analysis can be developed to determine the stability condition of an equilibrium point x^* of a flow. In this case, due to the solutions of the linearized system can be expressed as a composition of exponential functions, the stability of x^* is fulfilled if

$$\mathrm{Re}\,\lambda_j < 0 \quad \forall j \in [1, n].$$

2.1.3   Bifurcations of the fixed points

A *bifurcation* is said to occur when a topological change in the phase portrait is produced under variation of some parameters of the system. The set of parameter values at which a bifurcation appears is called a *bifurcation point*.

We must also introduce the concept of *codimension* of a bifurcation, which corresponds to the number of the independent parameters which determine the bifurcation.

Many kind of bifurcations can occur in smooth systems and an extended classification can be found in [74]. In what follows, we will focus on the codimension-one bifurcations of the fixed points for both flows and maps. Concerning discrete-time models, the bifurcations are yielded when one of the multipliers becomes nonhyperbolic, namely, it is placed in the unit cycle. This situation can be reached when DP has an eigenvalue equal to 1, -1, or a complex conjugate pair with unit modulus since the remaining eigenvalues have moduli not equal to 1 (see Fig. 2.2). Otherwise, the bifurcations in flows occur when the real part of the greatest eigenvalue becomes 0, being real or complex. The main bifurcations are listed below:

- **Saddle-Node bifurcation**: Several bifurcations can appear in maps when a real eigenvalue becomes 1. In the Saddle-Node or Fold bifurcation, one multiplier of two fixed points (a pair of stable and unstable fixed points) tends to 1 as one parameters is varied reaching the nonhyperbolicity simultaneously at the critical point, where these points collide and disappear (see Fig. 2.2a). This phenomenon can also occur in flows when two equilibria (one stable and one unstable) have real eigenvalues which simultaneously tend to 0.

- **Transcritical bifurcation**: In contrast to the fold bifurcation, in the transcritical bifurcation a pair of stable and unstable fixed points collides at the critical bifurcation point but not disappear. After the bifurcation, both fixed point exist but with the stability interchanged.

- **Pitchfork bifurcation**: This bifurcation is also detected when a real eigenvalue of a fixed point x^* becomes 1 while the remainder of eigenvalues are inside the unit cycle. There exist two kinds of bifurcations. In the subcritical case, two unstable fixed points which coexist together with the stable fixed point x^* collapse at the critical bifurcation point, when x^* becomes unstable. Similarly, in the supercritical case a pair of stable fixed point appear after the critical point and coexists with the unstable x^*.

  Both transcritical and pitchfork bifurcations can also be given for equilibrium points in flows.

- **Neimark-Sacker/Hopf bifurcation**: In the Neimark-Sacker bifurcation, a pair of complex conjugate eigenvalues crosses the unit cycle and their module

becomes greater than 1 (see Fig. 2.2b). Around the bifurcation, an invariant cycle appears, which can be stable (supercritical case) or unstable (subcritical case). This bifurcation can only appear in maps with dimension greater than 1. Notice that this bifurcation can be produced in a Poincaré map of a limit cycle, generating a two-dimensional torus in its corresponding continuous-time system.

The Hopf bifurcation is the analog of this bifurcation in flows, thus involving the appearance of a limit cycle at the time that an equilibrium point with complex eigenvalue becomes unstable. Similarly, only continuous-time systems with dimension greater than 1 can present a Hopf bifurcation.

- **Flip or period-doubling bifurcation**: This bifurcation is given when one real eigenvalue crosses the unit cycle becoming less than -1. This bifurcation has

(a) Saddle-Node

(b) Flip

(c) Neimark-Sacker

(d) Pitchfork and Transcritical
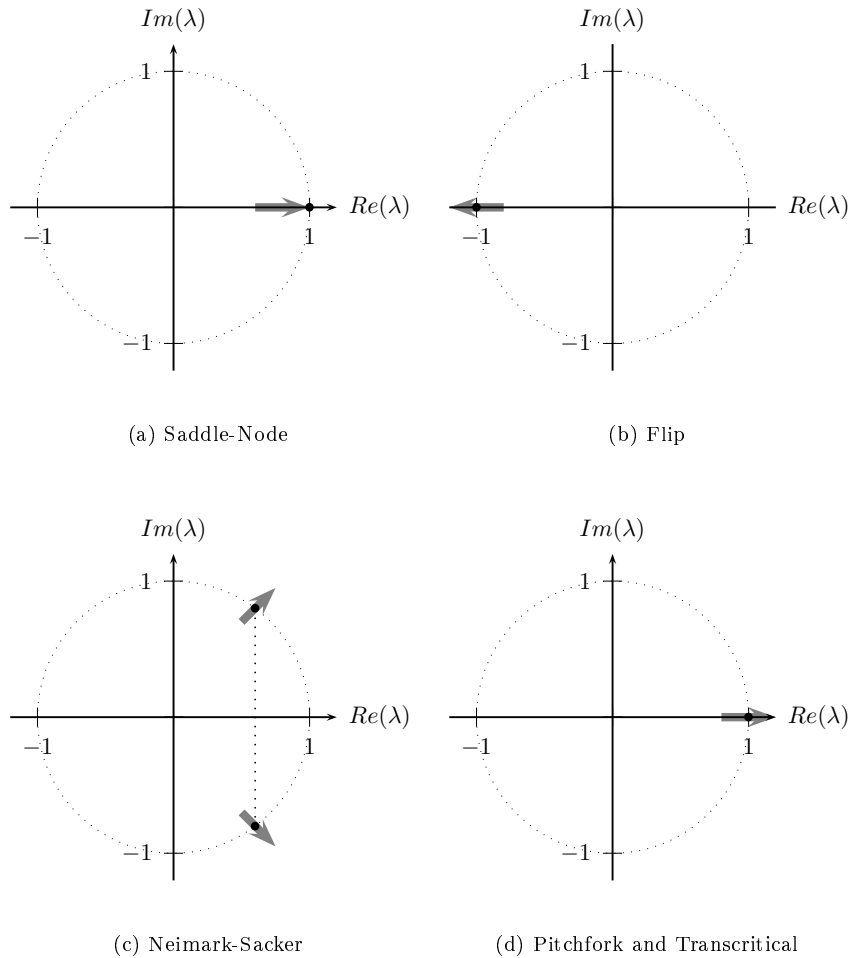
Figure 2.2. Possible bifurcations of the fixed point in maps.

associated a Pitchfork bifurcation in the second order map $P^2(x, \mu)$. In contrast to the mentioned bifurcations, the flip bifurcation does not have analogy with bifurcation of equilibrium points of flows.

2.2   Piecewise-smooth systems

Though the smooth theory is well established and explains properly low dimension nonlinear smooth systems, many applications in engineering or biological systems exhibit diverse bifurcation phenomena which are inexplicable in the frame of the classic smooth bifurcation theory. We can mention, for instance, electronics circuits containing diodes or transistors [11], mechanical systems involving impacts, stick-slip motion in oscillators with friction and hybrid dynamics in control systems. These systems are governed by smooth flows which are interrupted when some event is produced. Therefore, these processes cannot be described by means of simple systems of differential equations and require different mathematical formalisms as piecewise-smooth systems.

The non-smooth systems are known to exhibit a rich variety of bifurcations which has attracted the attention of many researchers; their results have been reported in an extensive literature. The earliest works in which the non-smooth phenomena were reported were published in Russian. We refer to the works of Andronov [1] in equilibrium bifurcations and Feigin [44, 45, 46] in the classification of C-bifurcations. In English literature, we must mention the work of Brogliato [17, 18] in mechanical systems, Zhusubaliyev & Mosekilde [112] in control and electronics systems, Tse [107], Leine [76], Kunke [72], Banerjee [7] and Peterka [96] in impacting systems, where the description of examples exhibiting non-smooth dynamics can be found. More recently, di Bernardo et al. presents in [29] general technics for analyzing the bifurcations which are unique in piecewise-smooth dynamical systems (also known as discontinuity-induced bifurcations).

Alternatively, the dynamical behavior of these systems has also been studied by using other formalisms, such as *differential inclusions* [62, 28] or *complementary systems* [57], which have been useful to describe mechanical systems and a mature analytical theory can be found in [17].

This section deals with the classification of the different non-smooth phenomena. We will provide some of the most relevant results found in the bibliography, mainly in discrete-time models. Similarly to the smooth theory, this section does not provide formal definitions and classification of non-smooth systems, which can be found in the references given. Nevertheless, a detailed analysis of piecewise-linear maps with two pieces will be developed here, which will be extended for three-piece piecewise-linear maps in Chapter 3.

(a) PWS Flows   (b) PWS Maps   (c) Hybrid PWS
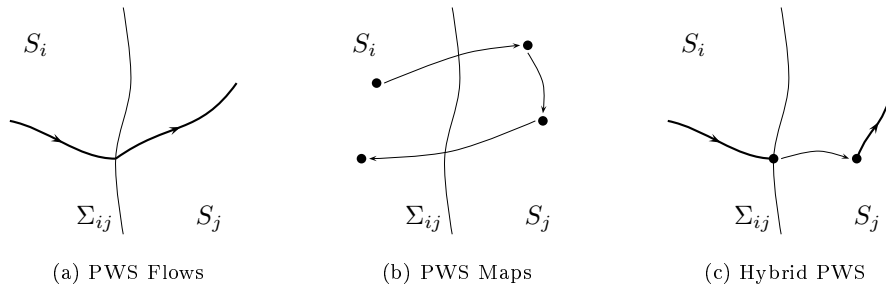
Figure 2.3. Trajectories of the state variable in different classes of piecewise-smooth systems.

2.2.1   Classification of the piecewise-smooth systems

We can describe a *piecewise-smooth* (PWS) system as a dynamical system composed by a set of ordinary differential equations or maps, which are associated to a different regions in the phase space.

Figure 2.3 shows the evolution of a state variable both for flows (see Fig. 2.3a) and for PWS maps (see Fig. 2.3b). Besides these, there exist systems whose dynamics needs to be modelled by using both formalisms: flows and maps. These processes will be called *hybrid* systems (see Fig. 2.3c). The discontinuity boundary Σ_{ij} is defined as the intersection between two sets, S_i and S_j. Σ_{ij} is also known as *discontinuity set* or *switching manifold* (flows) or *border* (maps).

The PWS systems can be classified depending on their *degree of non-smoothness* across the boundary. The discontinuity can be found in the state, vector field or higher derivatives, distinguishing the systems in PWS continuous, Filippov, or impacting systems:

- **Piecewise-smooth continuous systems**

  In the first class considered, the vector field characterizing the dynamics of the systems is continuous at the boundary (see Fig. 2.4a) whereas higher derivatives are discontinuous. Consequently, the boundary cannot act as an attractor or repeller in both sides at the same time which avoids the sliding dynamics.

- **Filippov systems**

  This class covers those PWS systems whose discontinuity is given in the vector field. Due to the normal component of the vector field can have opposite sign in the neighborhood of the boundary, these systems can permit the *sliding* dynamics. *The sliding motion* appears when the trajectories hit the boundary but are forced to continue their evolution in part of the switching manifold, which can become *part* of a periodic solution of the system. The complexity of this

(a) PWS Continuous   (b) Filippov systems   (c) Impacting systems
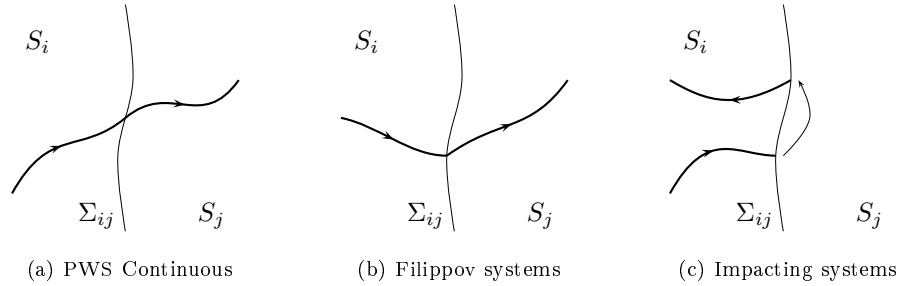
Figure 2.4. Classification of PWS flows depending on their degree of non-smoothness.

phenomenon is given by the loss of information on the initial conditions and their dynamics can be studied by using Filippov's convex [48] or Utkin's equivalent control [108] methods.

One of the examples of Filippov systems are the switching dc-dc converters [11] analyzed in this thesis. Besides these, Filippov systems arise in oscillators with dry friction or relay-feedback systems.

- **Impacting systems**

  In impacting systems, the switching manifold acts as a hard boundary as the region S_j in the phase space is forbidden (see Fig. 2.4c). Therefore, the dynamics of the impacting systems can be described by a smooth flow and a map which modifies the trajectory instantaneously when the trajectory hits the boundary.

  A great variety of examples can be found in mechanical systems as such the impacts oscillators, whose state variables are the position and velocity and the impact implies a change in the sign of the velocity. This phenomenon has drawn the attention of many researchers in the last decades since the early work of Peterka [96].

PWS maps can also be classified depending on their non-smoothness. Figure 2.5 illustrates the diagrams of three one-dimensional piecewise-smooth maps with different discontinuity degrees. In Fig. 2.5a, and Fig. 2.5b *piecewise-linear continuous* and *discontinuous* maps have been depicted respectively. The first map has a discontinuous derivative whereas in the second case the map presents a jump in the state. Another example of PWS maps is illustrated in Fig. 2.5c, which presents a fractional degree of discontinuity [29].

The non-smooth theory for one and two-dimensional smooth continuous maps began with the works developed by Feigin [44, 45, 46]. An English review of these works were translated into English by di Bernardo in 1999 [31]. It must also be mentioned the works of Nusse and Yorke in [89, 91, 90].

(a) PWL continuous   (b) PWL discontinuous   (c) Square-root PWS
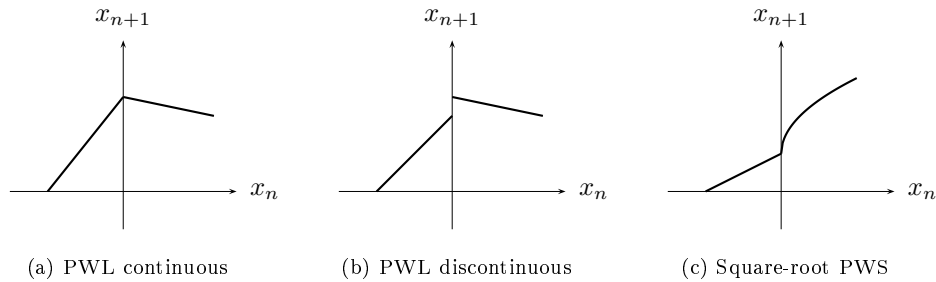
Figure 2.5. Examples of one-dimensional piecewise-smooth maps.

Discontinuous maps arise from Poincaré maps applied to systems involving impact
oscillators with multiple impacts. More examples can be found in the modelling of
irregular heartbeats [66], other biological systems and switching dc-dc converters [93].
The works of Lo Faro [77] and Qu et al. [97] show the existence of period-adding sce-
nario and multiple devil's staircases in these systems respectively are proved. Avrutin
studied a quadratic map with a gap in [3, 4, 5]. Regarding the development of theory
for discontinuous maps, this is still in the first stage. Some results in one-dimensional
maps can be found in [65, 93, 68]. Recently, Hogan et al. in [58] developed a classifica-
tion strategy of the piecewise-linear discontinuous map as extension for discontinuous
maps of the classification done by Feigin. The work is continued by Dutta et al. in
[37].

2.2.2   Bifurcations in PWS systems

Non-smooth systems can exhibit a great variety of bifurcations, including those seen
in smooth systems. Nevertheless, in what follows, we will only pay attention to those
bifurcations which are unique in piecewise-smooth systems and are called *Discontinu-
ity Induced Bifurcations* (DIB) [29]. This class of bifurcations has also been mentioned
in the bibliography as *C-bifurcations, non-smooth bifurcations* or *discontinuous bifur-
cations*.

We will consider as a DIB any topological change involving invariant sets and their
switching manifolds in the phase space. Namely, a DIB includes interactions of fixed
points, equilibrium points and limit cycles with the system switching manifolds. Figure
2.6 shows some representative bifurcations in PWS systems for fixed points in PWS
maps and equilibrium points and limit cycles in PWS flow.

- **Border-collisions (BC)**

  This bifurcation appears when a fixed point or a higher-periodic orbit of a
  piecewise-smooth map hits the boundary Σ at a critical parameter value. This
  class of bifurcations will be analyzed in detail in this dissertation.

(a) Boundary equilibrium

(b) Grazing bifurcation

(c) Sliding and sticking

(d) Corner collision
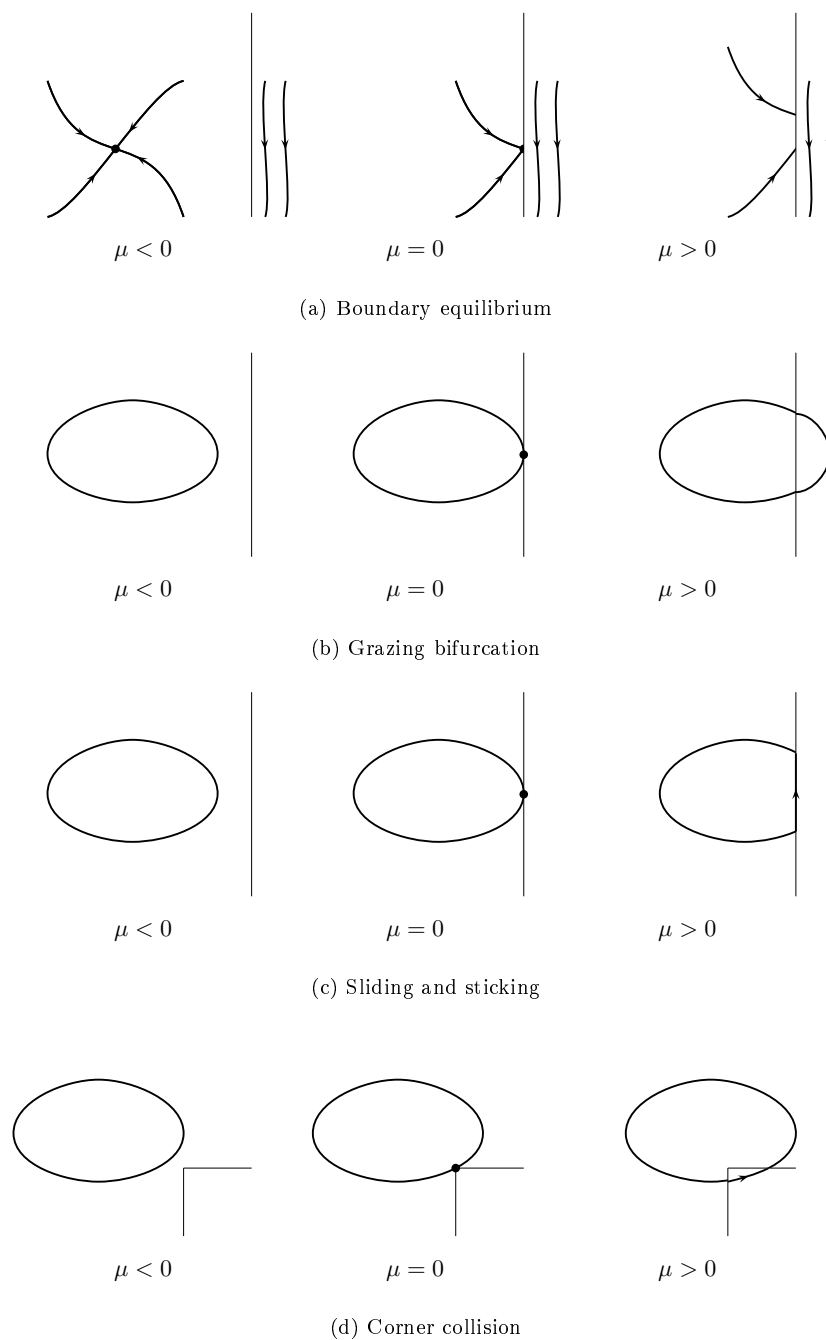
Figure 2.6. Different non-smooth bifurcations in PWS.

- **Boundary equilibrium bifurcations (BEB)**

  In piecewise-smooth flows, the simplest non-smooth bifurcation occurs when an equilibrium point hits the boundary Σ (see Fig. 2.6a). There not exists a complete strategy of classification of the possible scenarios. The existence of different scenarios after a BEB was firstly reported by Bautin & Leontovich and also shown in [50, 76]. In [33] an extension of the Feigin's classification is presented and extended. Regarding Filippov systems, an overview of the phenomena in planar systems by Kuznetsov et al. in [73] is presented.

  We will give few examples of the feasible phenomena after undergoing a BEB. When a boundary equilibrium in a PWS system is perturbed, this invariant set can *persist* or disappear in a *non-smooth fold*. More complex scenario is given when a limit cycle appears after a BEB. These phenomena can also be seen in Filippov or Hybrid systems with sliding, but there include new phenomena for instance *pseudo-equilibria*.

- **Grazing bifurcations of limit cycles**

  A grazing bifurcation occurs when a limit cycle of a flow becomes tangent to the discontinuity boundary (see Fig. 2.6b). This phenomenon is commonly seen in applications modelled with PWS systems.

  One of the technique used to study these non-smooth bifurcations is based in the use of *Discontinuity Mappings* [25]. This map was introduced by Nordmark in 1999 and now there exists a strategy to derive this map in n-dimensional systems.

- **Sliding bifurcations**

  Another class of DIBs covers the interactions between equilibrium points or limit cycles with sliding regions. In Fig. 2.6c, a limit cycle with part of its orbit in the switching boundary is generated after the sliding bifurcation. Some examples of this dynamics can be seen in certain models of the basic dc-dc converters, such as the Buck converter [92].

  A classification of sliding bifurcations of equilibrium points in planar Filippov Systems can also be found in [73]. Concerning bifurcations of limit cycles, early results were presented in [47].

- **Boundary intersection crossing/corner collision**

  Finally, we consider another kind of DIB given when an equilibrium point or limit cycle hits a $(n-2)$-dimensional surface formed by the intersection of two different discontinuity manifolds (see Fig. 2.6d).

  Some dynamics observed in dc-dc converters can be yielded by the intersection of a limit cycle with a *corner* in a switching manifold. An example of this phenomenon can be seen in [11], where a Buck converter exhibits a sudden transition from a periodic orbit to a large-amplitude chaos undergone by a corner-collision bifurcation.

2.2.3 Piecewise-smooth continuous maps

We now consider the family of maps which are locally continuous piecewise-linear and draw our attention to a local region in which there exists only one boundary. Therefore, we can define the following map

$$x \mapsto f(x,\mu) = \begin{cases} F_A(x,\mu), & \text{if } H(x,\mu) \leq 0, \\ F_B(x,\mu), & \text{if } H(x,\mu) > 0. \end{cases} \tag{2.1}$$

where $x \in \mathcal{D} \subset \mathbb{R}^n$, $F_A, F_B : \mathbb{R}^n \times \mathbb{R} \mapsto \mathbb{R}^n$, $\mu \in \mathbb{R}$ and $H : \mathbb{R}^n \mapsto \mathbb{R}$ are sufficiently smooth and differentiable functions of x. The condition $H(\mu) = 0$ define implicitly the boundary

$$\Sigma_{AB} = \{x \in \mathcal{D} : H(x,\mu) = 0\},$$

which divides the region $\mathcal{D}$ into

$$S_A = \{x \in \mathcal{D} : H(x,\mu) \leq 0\},$$
$$S_B = \{x \in \mathcal{D} : H(x,\mu) > 0\}.$$

Definition. x_i^* is said to be an *admissible fixed point* of (2.1) if $x_i^* = F_i(x_i^*)$ and $x_i^* \in S_i$. Otherwise, x_i^* is considered a *virtual fixed point* if $x_i^* = F_i(x_i^*)$ and $x_i^* \in S_j$ being $j \neq i$ for $i = A$ or $i = B$.

Definition. x_{ij}^* is said to be a *boundary fixed point* if $F_i(x_i^*) = F_j(x_j^*)$ of (2.1), namely, $x_{ij} \in \Sigma_{ij}$, being $i \neq j$ for $i, j = A$ or $i, j = B$.

Notice that these definitions can be extended easily to piecewise-smooth maps with multiple borders. For the sake of clarity, the stable and unstable fixed points will be denoted by upper (i. e. A, B, ...) and lower (i. e. a, b, ...) case letters respectively. After undergoing the BC bifurcation, there exist four main scenarios involving fixed points or higher dimensional periodic orbits, which will be defined as follows:

- **Persistence**: At the border-collision point, admissible and virtual fixed points placed in S_i turn into virtual and admissible fixed points in S_j.

- **Non-smooth fold**: Two admissible fixed points x_i^* and x_j^*, being $i \neq j$ collapse at bifurcation point as the parameter is varied.

(a) Persistence   (b) Non-smooth fold   (c) Non-smooth period-doubling
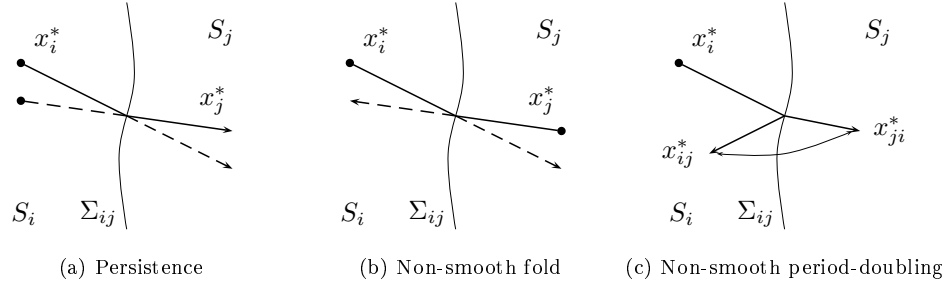
Figure 2.7. Feasible scenarios in a PWS map. Solid and dashed lines represent the evolution of the admissible and virtual fixed points in the phase space, respectively, under the variation of μ.

- **Non-smooth period-doubling**: After the fixed point x_i^* hits the boundary, a periodic orbit which has one fixed point in each region, appears.

- **Non-smooth period multiplying**: Similarly to non-smooth periodic orbit, a n-periodic orbit branches after the border-collision bifurcation.

- **Chaos**: Emerges when no others attractors are possible and the system does not diverge.

An appropriate normal form will be defined in order to develop a strategy of classification. This map can be obtained after linearizing (2.1) in the neighborhood of the bifurcation point and introducing a change of co-ordinates. The resulting normal form corresponds to a n-dimensional piecewise-linear map given by

$$x \mapsto f(x, \mu) = \begin{cases} N_A x + M\mu & \text{if } C^T x \le 0, \\ N_B x + M\mu & \text{if } C^T x > 0, \end{cases} \tag{2.2}$$

where

$$N_A = \frac{\partial F_A}{\partial x}, \quad N_B = \frac{\partial F_B}{\partial x},$$

$$M = \frac{\partial F_A}{\partial \mu} = \frac{\partial F_B}{\partial \mu}, \quad C^T = \frac{\partial H}{\partial x},$$

evaluated at $x = 0$ and $\mu = 0$.

Definition. σ_A^+ (σ_B^+) are defined as the number of real eigenvalues of N_A (N_B) greater than 1. Similarly, σ_A^- (σ_B^-) are said to be the number of real eigenvalues of N_A (N_B) less than -1.

After having defined these parameters, we can present the theorem introduced by Feigin in [44, 45]. The appearance of the following scenarios when the BC occurs will be given if the following conditions are fulfilled:

- **Persistence**: $\sigma_A^+ + \sigma_B^+$ is even.
- **Non-smooth fold**: $\sigma_A^+ + \sigma_B^+$ is odd.
- **Non-smooth period-doubling**: $\sigma_A^- + \sigma_B^-$ is odd.

The theorem will help us to analyze the non-smoothness of a one-dimensional PWL map with two pieces.

$\sigma_A^- + \sigma_B^-$	$\sigma_A^+ + \sigma_B^+$	$\sigma_{AA}^+ + \sigma_{AB}^+$	Scenarios
even	even		$A \leftrightarrow B$
even	odd		$A, b \leftrightarrow \varnothing$
odd	even	even	$A \leftrightarrow b, AB$; $A \leftrightarrow b, ab$
odd	even	odd	$A, ab \leftrightarrow B$; $A, ab \leftrightarrow b$
odd	odd	even	$A, b \leftrightarrow AB$; $A, b \leftrightarrow ab$
odd	odd	odd	$A, b, ab \leftrightarrow \varnothing$

Table 2.1. Classification of the border-collision bifurcations

2.3 Example: Analysis of a one-dimensional PWL map

This section deals with the analysis and classification of the border-collision bifurcations of the fixed points and higher periodic orbits of the simplest piecewise-linear continuous map composed by two pieces. The results presented in this study are considered as a first stage to understand the results presented in Chapter 3, where we analyze a PWL map composed by three pieces.

Let us consider the following piecewise-linear map:

$$x \mapsto f(x) = \begin{cases} \alpha x + \mu & \text{if } x \le 0, \\ \beta x + \mu & \text{if } x > 0, \end{cases} \tag{2.3}$$

where $x \in \mathbb{R}$ and α, β and μ are real parameters of the system.

Accordingly with (2.1) and (2.3), we obtain

$$F_A(x) = \alpha x + \mu \quad \text{and} \quad F_B(x) = \beta x + \mu,$$

(a) $A \leftrightarrow B$ ($\alpha = 0.75$, $\beta = -0.5$).

(b) $A \leftrightarrow b$ ($\alpha = 0.75$, $\beta = -1.5$).

(c) $\varnothing \leftrightarrow a, B$ ($\alpha = 1.5$, $\beta = -0.5$).

(d) $\varnothing \leftrightarrow a, b$ ($\alpha = 1.5$, $\beta = -1.5$).
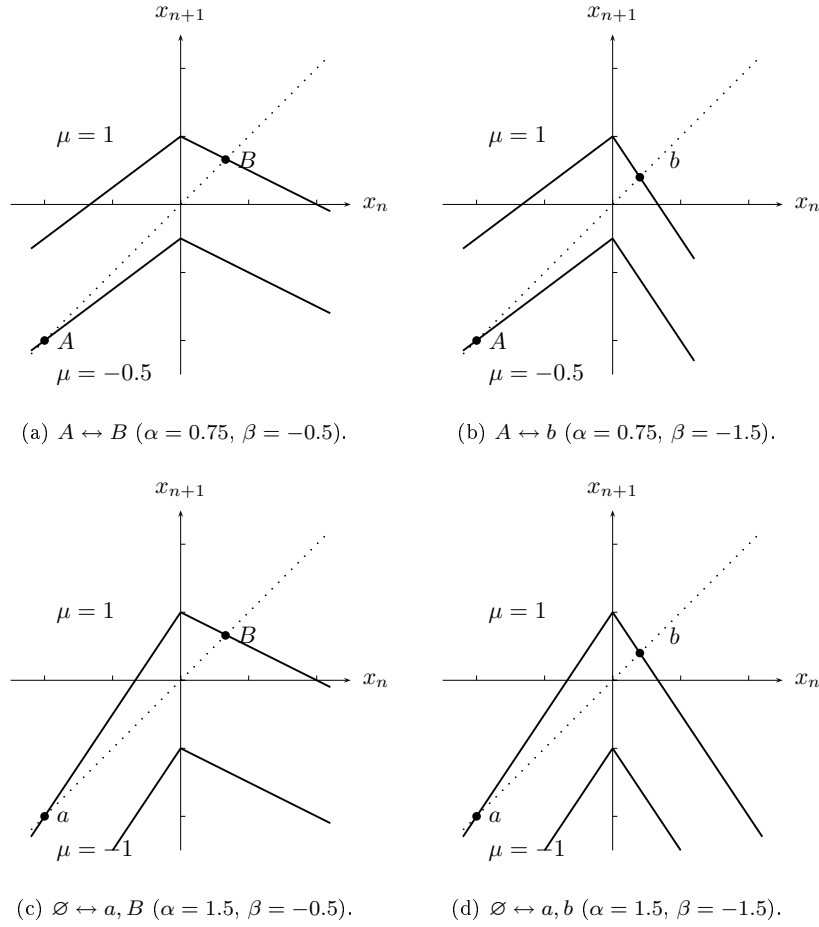
Figure 2.8. Illustrations of the map (2.3) for different values of α, β and μ, representing the four possible scenarios.

$$H(x) = x.$$

and hence

$$S_A = \{x \in R : x \leq 0\},$$
$$S_B = \{x \in R : x > 0\}.$$

Without loss of generality, the parameters α and β will be restricted to positive and negative values respectively.

2.3.1 Existence and stability of fixed points

The feasible fixed points of (2.3), which will be called x_A^* and x_B^* using the nomenclature proposed above, can be obtained applying $F_A(x_A^*) = x_A^*$ and $F_B(x_B^*) = x_B^*$ and
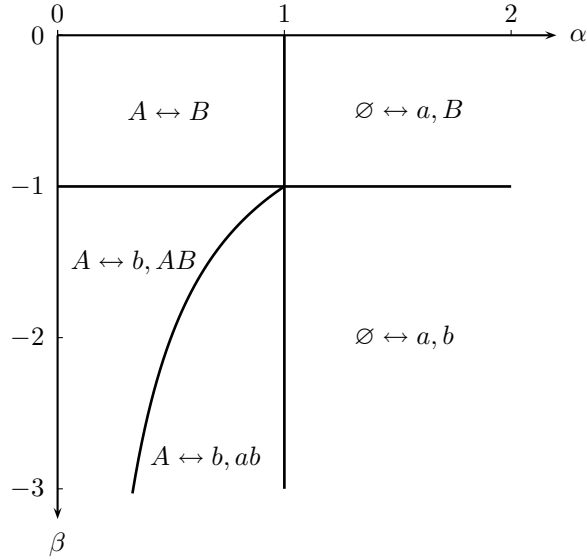
Figure 2.9. Possible scenarios for the one and two-periodic orbits of (2.3).

hence,

$$x_A^* = \frac{\mu}{1-\alpha} \quad \text{and} \quad x_B^* = \frac{\mu}{1-\beta},$$

which will be admissible if

$$x_A^* < 0 \tag{2.4}$$

and

$$x_B^* > 0. \tag{2.5}$$

Therefore, from (2.4) and (2.5), x_A^* and x_B^* will exist for negative and positive values of μ respectively. Dealing with their stability, x_A^* and x_B^* will be stable provided that $\alpha < 1$ and $\beta > -1$ respectively. Then, four different non-smooth scenarios can take place as the parameter μ is varied depending on the parameters α and β:

$$A \leftrightarrow B, \quad A \leftrightarrow b, \quad \varnothing \leftrightarrow a, B \quad \text{and} \quad \varnothing \leftrightarrow a, b,$$

where now the symbol $\leftrightarrow$ means the variation of μ from negative to positive values.

In Fig. 2.8, four diagrams representing the possible scenarios have been depicted for different values of the parameters.

2.3.2 Existence and stability of period-two orbits

Let us now study the existence and stability of period-two orbits. As a result of the linearity of the functions F_A and F_B, orbits such as AA, aa, BB and bb cannot appear.

Consequently, the period-two orbits must have the forms AB or ab, which means that one solution must be placed in S_A (x^*_{AB}) whereas the other solution must be in S_B (x^*_{BA}). From the set of equations

$$x^*_{BA} = \alpha x^*_{AB} + \mu,$$
$$x^*_{AB} = \beta x^*_{BA} + \mu,$$

the following solution is straight forward,

$$x^*_{AB} = \mu \frac{1+\beta}{1-\alpha\beta} \quad \text{and} \quad x^*_{BA} = \mu \frac{1+\alpha}{1-\alpha\beta}.$$

The existence of the period-two orbit is guaranteed if $x^*_{AB} < 0$ and $x^*_{BA} > 0$. Hence, the orbit will only exist for positive values of μ if $\beta < -1$.

Finally, the eigenvalue associated to the second iteration of (2.3) corresponds to $\alpha\beta$ and thus, the stability will be proved if $\alpha\beta > -1$.

The different scenarios which can occur have been depicted in Fig. 2.9 where the condition of existence and stability have been plotted in the parameter space $\{\alpha, \beta\}$.

2.3.3 Existence and stability of higher periodic orbits

Assuming the restrictions of the parameters given above, it has been proved that only the higher periodic orbits with the form $A^{k-1}B$ and $a^{k-1}b$ can exist [31]. These orbits are composed by one point placed in the region S_B, which must be positive to fulfil the existence condition, whereas the remainder points belong to the region S_A and must be positive. The possible scenarios present at the border-collision are proved to be

$$A \leftrightarrow b, ab, ..., a^{k-2}b, A^{k-1}B,$$
$$A \leftrightarrow b, ab, ..., a^{k-2}b, a^{k-1}b,$$
$$\varnothing \leftrightarrow a, b, ab, a^{k-1}b.$$

Therefore, only the periodic orbits $A^{k-1}B$ can be stable in the map. Let us now develop the existence condition of this attractor.

Assuming that the points composing the k-periodic orbit are given by

$$x^*_B, \quad x^*_{A_1}, \quad x^*_{A_2}, \quad ... \quad , \quad x^*_{A_{k-1}},$$

the following set of equations can be easily obtained:

$$x^*_{A_1} = \beta x^*_B + \mu, \tag{2.6}$$
$$x^*_{A_j} = \alpha x^*_{A_{j-1}} + \mu \qquad \text{for } 2 \leq j \leq k-1, \tag{2.7}$$
$$x^*_B = \alpha x^*_{A_{k-1}} + \mu. \tag{2.8}$$

The k-periodic orbit will exist provided that the following conditions are fulfilled:

$$x^*_B \geq 0, \quad x^*_{A_1} \leq 0, \quad x^*_{A_2} \leq 0, \quad ... \quad , x^*_{A_{k-1}} \leq 0.$$

Let us suppose that $x^*_{A_{k-1}} \leq 0$. Then, taking into account that

$$x^*_{A_{k-2}} = \frac{x^*_{A_{k-1}} - \mu}{\alpha},$$

and $\alpha > 0$ and $\mu > 0$, it is easy to prove that all points placed in S_A are also negative. Moreover, according (2.6), x^*_B will positive as $\beta < 0$. Therefore, the existence will be guaranteed if $x^*_{A_{k-1}} \leq 0$. From (2.6), (2.7) and (2.8), the expression for $x^*_{A_{k-1}}$ can be found and is expressed as follows

$$x^*_{A_{k-1}} = \mu \frac{1 + \alpha + ... + \alpha^{k-2} + \alpha^{k-2}\beta}{1 - \alpha^{k-1}\beta} \leq 0. \tag{2.9}$$

Taking into account that $1 - \alpha^{k-1}\beta$ is positive, (2.9) will be fulfilled if

$$\beta < -\left(1 + \frac{1}{\alpha} + \frac{1}{\alpha^2} + ... + \frac{1}{\alpha^{k-2}}\right) = \frac{1 - \alpha^{k-1}}{\alpha^{k-1} - \alpha^{k-2}}.$$

Let us define the function $\psi_k(\alpha)$ as

$$\psi_k(\alpha) = \frac{1 - \alpha^{k-1}}{\alpha^{k-1} - \alpha^{k-2}}. \tag{2.10}$$

The existence of the k-periodic orbit $A^{k-1}B/a^{k-1}b$ is guarantied if $\mu > 0$ and

$$\beta < \psi_k(\alpha).$$

Regarding the stability condition, it can be obtained from the eigenvalue of the iterated map. It is easy to prove that this eigenvalue corresponds to $\alpha^{k-1}\beta$ and hence, considering the following definition of the function $\phi_k(\alpha)$ as

$$\phi_k(\alpha) = -\frac{1}{\alpha^{k-1}}, \tag{2.11}$$

the k-periodic orbit will be stable so long as

$$\beta > \phi_k(\alpha).$$

Curves (2.10) and (2.11) have been depicted in Fig. 2.10 for $k = 2..4$, together with $\alpha = 1$ and $\beta = -1$, to summarize the different scenarios studied in this section.
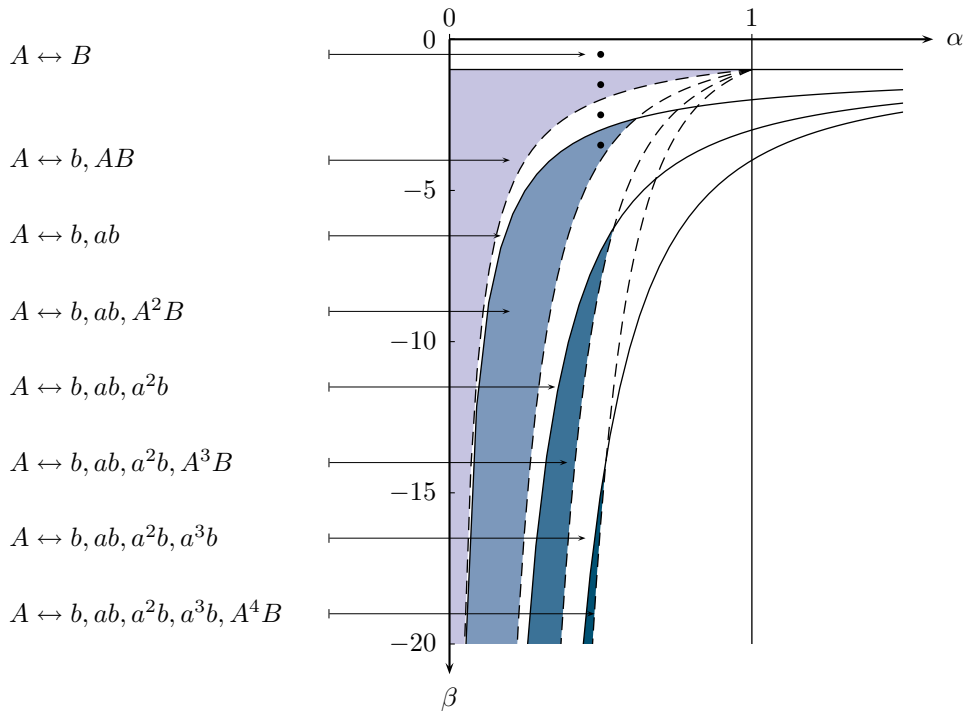
Figure 2.10. Possible scenarios for the k-periodic orbits of (2.3) in the parameter space $\{\alpha, \beta\}$.

Functions $\psi_k(\alpha)$ and $\phi_k(\alpha)$ have been plotted using dashed and solid lines respectively and colored zones stands for regions in which an stable orbit exists. Notice that stable solutions can only take place if $\alpha < 1$. Moreover, for values of α greater than one, the existence of a is restricted to positive values of μ.

The study of the existence of these periodic orbits reveals that stable fixed points and higher-periodic orbit cannot coexist.

2.3.4 Robust chaos. Bifurcation diagrams

Numerical simulations of the map (2.3) reveal the presence of chaotic attractors in the one-dimensional PWL continuous map (see Fig. 2.11d). Their appearance is restricted to zones in which any fixed point or periodic orbit is stable. It is proved that under the conditions

$$\psi_{k-1}(\alpha) < \beta < \psi_k(\alpha) \quad \text{and} \quad \beta > \phi_k(\alpha),$$

the map exhibits robust chaotic dynamics [31]. *Robust* means the no existence of periodic windows, in contrast to nonlinear smooth systems such as the logistic map.

(a) $A \leftrightarrow B$ ($\beta = -0.5$)

(b) $A \leftrightarrow b, AB$ ($\beta = -1.5$)

(c) $A \leftrightarrow b, ab$ ($\beta = -2.5$)

(d) $A \leftrightarrow b, ab, A^2B$ ($\beta = -3.5$)
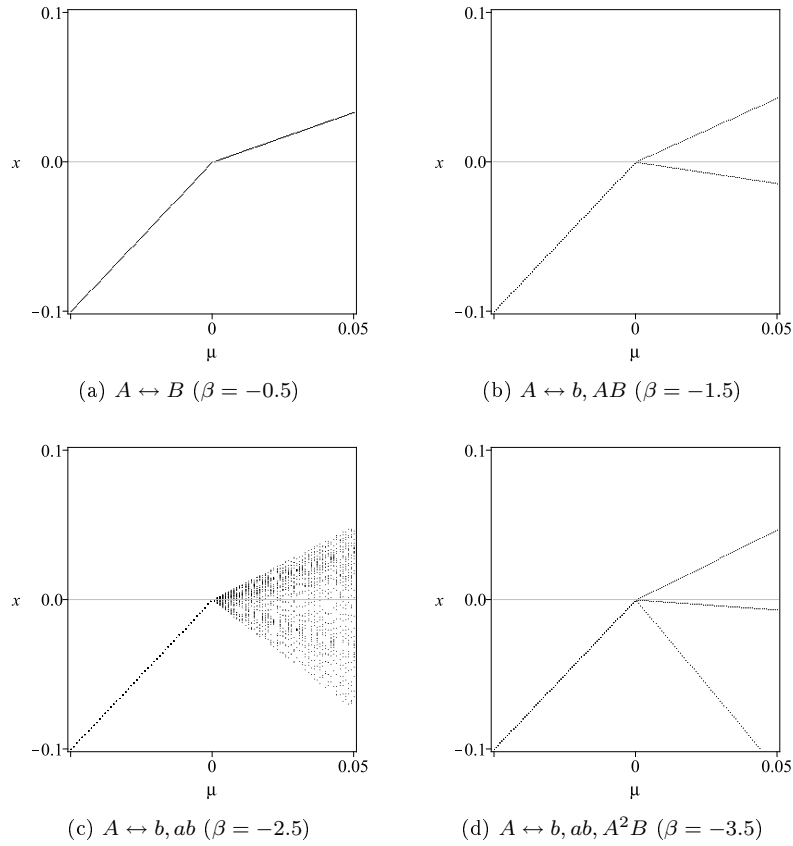
Figure 2.11. Bifurcation diagrams using μ as the varying parameter and considering $\alpha = 0.5$.

To conclude, some relevant bifurcation diagrams have been depicted in Fig. 2.11 using μ as varying parameter. Persistence, non-smooth period-doubling, robust chaos and period-three orbit are illustrated in 2.11a, 2.11b, 2.11c and 2.11d respectively.

Chapter 3

Non-smooth dynamics of a three-piece piecewise-linear map

> *This chapter deals with the study of the dynamics of a three-piece continuous piecewise-linear map. Expressions for the existence and stability of the fixed points and period-two orbits are determined in a restricted set of parameters jointly with an extended classification of the border-collision bifurcations. The basins of attraction in those set of parameters in which coexistence of attractors can be found are also determined. This analysis will help us to understand the dynamics of the SIMIMO converter under both SPC and IC controls, which will be discussed in the following chapters.*

3.1 Definition of the map

Let us consider the following three-piece piecewise-linear map

$$
x \mapsto f(x) = \begin{cases} F_A(x, \phi) & \text{if } x \in S_A, \\ F_B(x, \phi) & \text{if } x \in S_B, \\ F_C(x, \phi) & \text{if } x \in S_C, \end{cases} \tag{3.1}
$$

where $x \in \mathcal{D} \subset \mathbb{R}$ and $F_i : \mathbb{R} \times \mathbb{R}^5 \mapsto \mathbb{R}$, being $i \in \{A, B, C\}$.
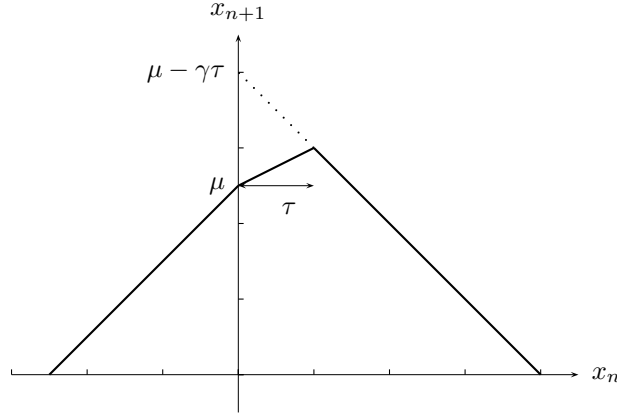
Figure 3.1. The three-piece piecewise-linear map.

The expressions for the linear functions will be expressed as follows

$$F_A(x, \alpha, \mu) = \alpha x + \mu, \tag{3.2}$$

$$F_B(x, \alpha, \beta, \mu) = (\alpha + \beta)x + \mu, \tag{3.3}$$

$$F_C(x, \alpha, \beta, \gamma, \mu, \tau) = (\alpha + \beta + \gamma)x + \mu - \gamma\tau. \tag{3.4}$$

Notice that the definition of the parameters considered here, where β (γ) corresponds to the difference between the slopes of F_A and F_B (F_B and F_C). This property permits to provide simpler expressions for the restriction of the parameters when adapting the discrete-time model to the SIMIMO converter in following chapters.

The regions are defined as

$$S_A = \{x \in \mathcal{D} : x \le 0\}, \tag{3.5}$$

$$S_B = \{x \in \mathcal{D} : 0 < x \le \tau\}, \tag{3.6}$$

$$S_C = \{x \in \mathcal{D} : x > \tau\}, \tag{3.7}$$

and it is easy to prove that the boundaries are described by

$$\Sigma_{AB}(x) = \{x \in \mathcal{D} : x = 0\},$$

$$\Sigma_{BC}(x) = \{x \in \mathcal{D} : x - \tau = 0\}.$$

Therefore, the piecewise-linear map proposed here will be described by five parameters, whose domains are summarized in Table 3.1.

Let us now explain the significance of the restrictions applied to the parameters. Firstly, α will be always considered positive and less or equal than one, thus the

Parameter	Domain
α	$[0,1]$
β	$(-\infty, 0]$
γ	$(-\infty, \infty]$
μ	$(-\infty, +\infty)$
τ	$(0, \infty)$

Table 3.1. Domain of the parameters α, β, γ, μ, τ. The parameters must also fulfil the condition $\alpha + \beta + \gamma \leq 1$.
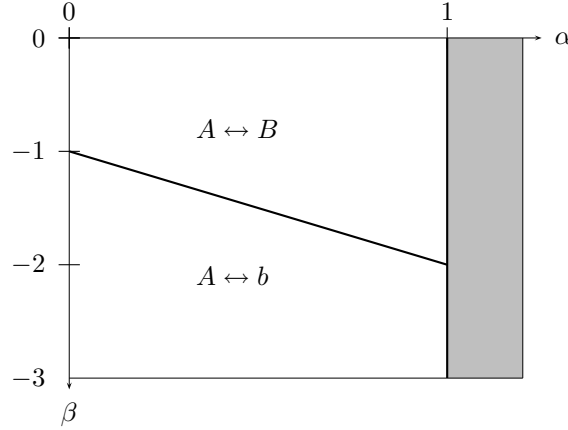
Figure 3.2. Behavior of the fixed points x_A^* and x_B^* in the planar space $\{\alpha, \beta\}$. $\mu \in (-\infty, \mu_{AB}^0) \leftrightarrow \mu \in (\mu_{AB}^0, \mu_{BC}^0)$.

slope of F_A will be always positive. Moreover, β is negative and consequently, the slope of F_B will be always less than the slope of F_A, despite being positive or negative, but less than 1. Finally, although γ can be positive or negative, the third slope $(\alpha + \beta + \gamma)$ must be less than 1.

Concerning the definition of the boundaries, the first border has been placed at $x = 0$ in order to simplify the analysis and ensure the continuity of the map. In the same way, the second boundary is placed at $x = \tau$, which will be always positive to guarantee that the map is divided into three pieces.

3.2   Existence and stability of fixed points

The map (3.1) presents the following fixed points:

$$x_A^* = \frac{\mu}{1-\alpha},$$
$$x_B^* = \frac{\mu}{1-(\alpha+\beta)},$$
$$x_C^* = \frac{\mu-\gamma\tau}{1-(\alpha+\beta+\gamma)}.$$

Notice that the fixed point x_A^* is not defined when $\alpha = 1$. These fixed points will undergo a border-collision bifurcation when they hit any of the boundaries of the map, which means that any of the following conditions $\Sigma_{AB}(x_A^*)$ (or $\Sigma_{AB}(x_B^*)$) or $\Sigma_{BC}(x_B^*)$ ($\Sigma_{BC}(x_C^*)$) is fulfilled. Using μ as a varying parameter, the fixed points will cross the boundaries Σ_{AB} and Σ_{BC} at the critical values μ_{AB}^0 and μ_{BC}^0 respectively, given by (see Fig. 3.3)

$$\mu_{AB}^0 = 0,$$
$$\mu_{BC}^0 = \tau(1-(\alpha+\beta)).$$

Let us now study the existence conditions of the fixed points. Firstly, x_A^* will be an admissible fixed point if $x_A^* < 0$ and, taking into account that $1-\alpha > 0$, x_A^* will only exist if $\mu < 0$. Moreover, its stability is always guarantied because the range of α.

Similarly, the fixed point x_B^* will exist if $x_B^* > 0$ and $x_B^* < \tau$. Considering that $1-(\alpha+\beta) > 0$, the existence of x_B^* will be proved if $\mu > \mu_{AB}^0$ and $\mu < \mu_{BC}^0$, whose value is always higher than μ_{AB}^0 and thus, x_B^* is an admissible fixed point if $\mu_{AB}^0 < \mu < \mu_{BC}^0$. In addition, its stability will be proved when $\alpha+\beta > -1$.

Finally, the fixed point x_C^* will be an admissible fixed point if $x_C^* > \tau$. Therefore, considering that $\alpha+\beta+\gamma < 1$, the existence condition will be fulfilled if

$$\mu - \gamma\tau > \tau(1-(\alpha+\beta+\gamma)),$$

and hence, x_C^* will exists if

$$\mu > \mu_{BC}^0.$$

The stability of x_C^* is guaranteed if $\alpha+\beta+\gamma > -1$.

These results have been summarized in Fig. 3.2 and Fig. 3.4, in which the existence and stability conditions have been depicted in the two-parameter space $\{\alpha, \beta\}$ and $\{\alpha+\beta, \gamma\}$ respectively. Some remarkable conclusions can be obtained from our analysis: the attractor A is always presented for negative values of μ and none of the three fixed points can coexist in a given set of parameters.

(a) μ_{AB}^0 and μ_{BC}^0

(b) μ_{BC}^1

(c) μ_{AB}^1
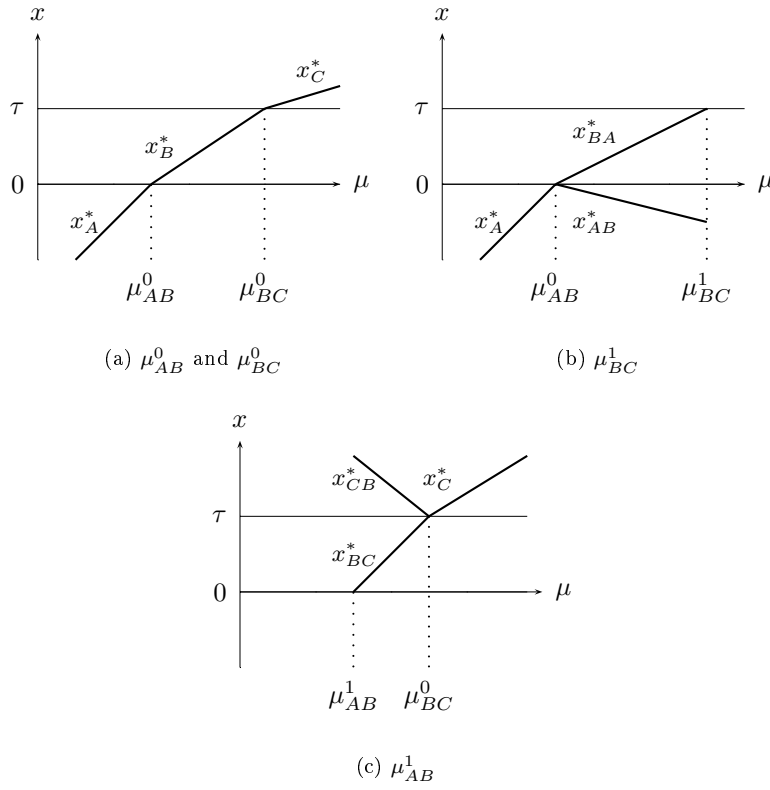
Figure 3.3. Illustrations of the critical values of μ.
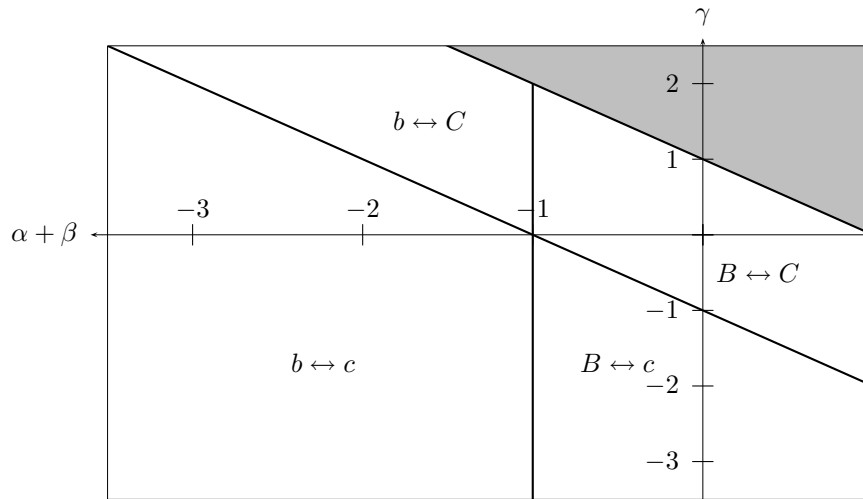
Figure 3.4. Behavior of the fixed points x_B^* and x_C^* in the planar space $\{\alpha + \beta, \gamma\}$. $\mu \in (\mu_{AB}^0, \mu_{BC}^0) \leftrightarrow (\mu_{BC}^0, +\infty)$.

3.3   Existence and stability of two-periodic solutions

Period-two solutions of the map (3.1) correspond to the pair of fixed points of the second iterative maps given by

$$F_i(F_j(x, \alpha, \beta, \gamma, \mu, \tau)) \quad \text{and} \quad F_j(F_i(x, \alpha, \beta, \gamma, \mu, \tau)), \tag{3.8}$$

where i, j can be A, B or C. These orbits, which will be named (x_{ij}^*, x_{ji}^*), are admissible if $x_{ij}^* \in S_i$ and $x_{ji}^* \in S_j$. Because of the linearity of the map, the two-periodic orbits (x_{ii}^*, x_{ii}^*), which have both fixed points in the same region, cannot be admissible. Therefore, only three possible two-periodic orbits can be found in this three-piece map: (x_{AB}^*, x_{BA}^*), (x_{BC}^*, x_{CB}^*) and (x_{AC}^*, x_{CA}^*). In this section, the existence and stability of each of these possible attractors will be analyzed in detail.

3.3.1   Two-periodic orbit (x_{AB}^*, x_{BA}^*)

The orbit (x_{AB}^*, x_{BA}^*) has its fixed points placed in the regions S_A and S_B respectively. Therefore, from (3.5) and (3.6), the conditions of existence of x_{AB}^* and x_{BA}^* are given by

$$x_{AB}^* < 0, \tag{3.9}$$

$$x_{BA}^* > 0 \quad \text{and} \quad x_{BA}^* < \tau \tag{3.10}$$

respectively, where the expressions of both points x_{AB}^* and x_{BA}^* are expressed as follows

$$x_{AB}^* = \frac{1 + \alpha + \beta}{1 - \alpha(\alpha + \beta)}\mu, \qquad x_{BA}^* = \frac{1 + \alpha}{1 - \alpha(\alpha + \beta)}\mu.$$

Considering the domain of the parameters, the expressions $1 - \alpha(\alpha + \beta)$ and $1 + \alpha$ are always positive and thus, the first part of the condition (3.10) can only be fulfilled for $\mu > \mu_{AB}^0$. Moreover, from the condition (3.9) and assuming positive values of μ, the following condition must be also fulfilled to guarantee the existence of the periodic solution:

$$\alpha + \beta < -1.$$

Notice that this inequality corresponds to the instability condition of the fixed point x_B^* seen above. Finally, the first part of the condition (3.10) implies that

$$\mu < \tau \frac{1 - \alpha(\alpha + \beta)}{1 + \alpha} = \mu_{BC}^1. \tag{3.11}$$

μ_{BC}^1 is defined as the critical value of μ at which the point x_{BA}^* reaches the boundary Σ_{BC} (see Fig. 3.3b). Notice that $\mu_{BC}^1 < \mu_{BC}^0$. Concerning the stability of the two-periodic orbit, it is guaranteed if

$$\alpha(\alpha + \beta) > -1. \tag{3.12}$$
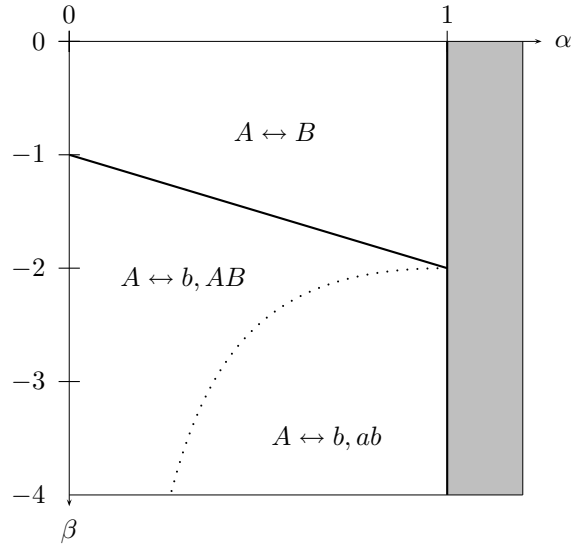
Figure 3.5. Existence and stability of x_A^* and x_B^* and two-periodic orbit (x_{AB}^*, x_{BA}^*) in the planar space $\{\alpha, \beta\}$. $\mu \in (-\infty, \mu_{AB}^0) \leftrightarrow (\mu_{AB}^0, \mu_{AB}^1)$. Solid and dotted lines correspond to the conditions $\alpha + \beta = -1$ and $\alpha(\alpha + \beta) = -1$ respectively.

All these results are summarized in Fig. 3.5, in which the curves of existence and stability for the fixed points A and B and the two-periodic orbit AB/ab are plotted.

3.3.2 Two-periodic orbit (x_{BC}^*, x_{CB}^*)

Similarly, the periodic orbit (x_{BC}^*, x_{CB}^*) has the fixed points in the regions S_B and S_C respectively. Therefore, this two-periodic orbit will exist so long as

$$x_{BC}^* > 0, \qquad x_{BC}^* < \tau \qquad \text{and} \qquad x_{CB}^* > \tau, \tag{3.13}$$

where the expressions of the fixed points of the attractor can be easily obtained from (3.3), (3.4) and (3.8) and are given by

$$x_{BC}^* = \frac{\mu(1 + \alpha + \beta + \gamma) - \gamma\tau}{1 - (\alpha + \beta)(\alpha + \beta + \gamma)} \qquad \text{and} \qquad x_{CB}^* = \frac{\mu(1 + \alpha + \beta) - \gamma\tau(\alpha + \beta)}{1 - (\alpha + \beta)(\alpha + \beta + \gamma)}.$$

From the two last conditions of (3.13), we obtain the following inequalities:

$$x_{BC} - \tau = \frac{(1 + \alpha + \beta + \gamma)(\mu - \tau(1 - (\alpha + \beta)))}{1 - (\alpha + \beta)(\alpha + \beta + \gamma)} = \frac{(1 + \alpha + \beta + \gamma)(\mu - \mu_{BC}^0)}{1 - (\alpha + \beta)(\alpha + \beta + \gamma)} < 0$$

$$x_{CB} - \tau = \frac{(1 + \alpha + \beta)(\mu - \tau(1 - (\alpha + \beta)))}{1 - (\alpha + \beta)(\alpha + \beta + \gamma)} = \frac{(1 + \alpha + \beta)(\mu - \mu_{BC}^0)}{1 - (\alpha + \beta)(\alpha + \beta + \gamma)} > 0. \tag{3.14}$$
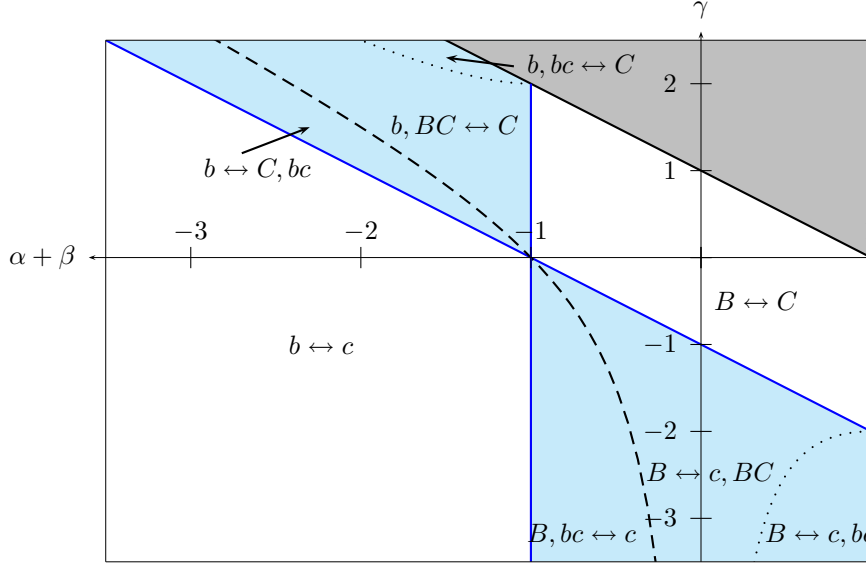
Figure 3.6. Existence and stability of x_B^*, x_C^* and the two-periodic orbit (x_{BC}^*, x_{CB}^*) in the planar space $\{\alpha + \beta, \gamma\}$. $\mu \in (\mu_{AB}^0, \mu_{BC}^0) \hookrightarrow (\mu_{BC}^0, \mu_{AB}^1)$ if $\mu_{AB}^1 > \mu_{BC}^0$ or $\mu \in (\mu_{AB}^0, \mu_{BC}^0) \hookrightarrow (\mu_{BC}^0, +\infty)$ if $\mu_{AB}^1 < \mu_{BC}^0$.

which have been factorized to make the analysis easier. Notice that the existence of this periodic orbit requires that $1 + \alpha + \beta + \gamma$ and $1 + \alpha + \beta$ must have different sign. Hence, the orbit BC/bc will exist

$$\text{if} \quad \gamma < 0, \quad \text{and} \quad \alpha + \beta + \gamma < -1 \quad \text{and} \quad \alpha + \beta > -1, \tag{3.15}$$

or

$$\text{if} \quad \gamma > 0, \quad \text{and} \quad \alpha + \beta + \gamma > -1 \quad \text{and} \quad \alpha + \beta < -1. \tag{3.16}$$

These results are illustrated in Fig. 3.6, where the critical conditions $\alpha + \beta + \gamma = -1$ and $\alpha + \beta = -1$ have been depicted using blue lines. Moreover, in the region colored in blue, the set of parameters fulfil (3.15) and (3.16) and therefore, the orbit (x_{BC}^*, x_{CB}^*) is admissible.

Let us now focus in the range of μ which guaranties the existence of the two-periodic orbit. For (3.15), when the denominator of (3.14) is negative, the admissibility is given when $\mu < \mu_{BC}^0$. Therefore, if $\gamma < 0$, the existence of the orbit is given by

$$\mu < \mu_{BC}^0 \quad \text{and} \quad 1 - (\alpha + \beta)(\alpha + \beta + \gamma) < 0,$$

$$\mu > \mu_{BC}^0 \quad \text{and} \quad 1 - (\alpha + \beta)(\alpha + \beta + \gamma) > 0.$$

Otherwise, from (3.16), we obtain the conditions

$$\mu < \mu_{BC}^0 \quad \text{and} \quad 1 - (\alpha + \beta)(\alpha + \beta + \gamma) > 0,$$

$$\mu > \mu_{BC}^0 \quad \text{and} \quad 1 - (\alpha + \beta)(\alpha + \beta + \gamma) < 0.$$

In Fig. 3.6, the different scenarios have been represented specifying the different obits which are admissible in both sides of the border-collision bifurcation at the critical value of $\mu = \mu_{BC}^0$. The results obtained are characteristic of a two-piece PWL, because only one boundary has been taken into account. Notice also the symmetry is the different scenarios illustrated in Fig. 3.6.

Nevertheless, due to the map (3.1) is composed by three pieces, there exists another boundary when the fixed point x_{BC}^* reaches Σ_{AB} ($x_{BC}^* = 0$). Therefore, from the first condition of (3.13), when $1 - (\alpha + \beta)(\alpha + \beta + \gamma) > 0$ and $\alpha + \beta + \gamma > -1$, we obtain the condition

$$\mu > \frac{\gamma\tau}{1 + \alpha + \beta + \gamma} = \mu_{AB}^1. \tag{3.17}$$

The critical value μ_{AB}^1 is defined as the value of μ for which x_{BC}^* reaches the boundary Σ_{AB} (see Fig. 3.3c). Therefore, considering all the solutions of the first condition of (3.13) it is obtained:

$$\text{if} \quad 1 - (\alpha + \beta)(\alpha + \beta + \gamma) > 0, \quad \text{and} \quad \alpha + \beta + \gamma > -1 \quad \text{and} \quad \mu > \mu_{AB}^1,$$

$$\text{if} \quad 1 - (\alpha + \beta)(\alpha + \beta + \gamma) > 0, \quad \text{and} \quad \alpha + \beta + \gamma < -1 \quad \text{and} \quad \mu < \mu_{AB}^1,$$

$$\text{if} \quad 1 - (\alpha + \beta)(\alpha + \beta + \gamma) < 0, \quad \text{and} \quad \alpha + \beta + \gamma > -1 \quad \text{and} \quad \mu < \mu_{AB}^1,$$

$$\text{if} \quad 1 - (\alpha + \beta)(\alpha + \beta + \gamma) < 0, \quad \text{and} \quad \alpha + \beta + \gamma < -1 \quad \text{and} \quad \mu > \mu_{AB}^1.$$

In order to establish the range of μ where the orbit is admissible in each region of the parameter space, it is required to determine the relation between both critical values μ_{BC}^0 and μ_{AB}^1. Hence, from $\mu_{AB}^1 < \mu_{BC}^0$, the following condition is obtained:

$$\frac{1 - (\alpha + \beta)(\alpha + \beta + \gamma)}{1 + \alpha + \beta + \gamma} > 0.$$

Therefore, the orbit (x_{BC}^*, x_{CB}^*) will be admissible so long as

$$\text{for} \quad 1 - (\alpha + \beta)(\alpha + \beta + \gamma) > 0 \quad \text{and} \quad \alpha + \beta + \gamma > -1, \quad \mu_{AB}^1 < \mu < \mu_{BC}^0,$$

$$\text{for} \quad 1 - (\alpha + \beta)(\alpha + \beta + \gamma) > 0 \quad \text{and} \quad \alpha + \beta + \gamma < -1, \quad \mu_{BC}^0 < \mu < \mu_{AB}^1,$$

$$\text{for} \quad 1 - (\alpha + \beta)(\alpha + \beta + \gamma) < 0 \quad \text{and} \quad \alpha + \beta + \gamma > -1, \quad \mu_{BC}^0 < \mu < \mu_{AB}^1,$$

$$\text{for} \quad 1 - (\alpha + \beta)(\alpha + \beta + \gamma) < 0 \quad \text{and} \quad \alpha + \beta + \gamma < -1, \quad \mu_{AB}^1 < \mu < \mu_{BC}^0.$$

It is important to remark that μ_{AB}^1 can be negative (and then $\mu_{AB}^1 < \mu_{AB}^0$) for negative values of γ and $\alpha + \beta + \gamma > -1$ or for positive values of γ and $\alpha + \beta + \gamma < -1$. Notice that is this region in the parameter space, the orbit (x_{BC}^*, x_{CB}^*) cannot exist.

Finally, the stability of the orbit BC/bc will be given if the following condition is fulfilled:

$$-1 < (\alpha + \beta)(\alpha + \beta + \gamma) < 1.$$

Notice that the condition $(\alpha + \beta + \gamma)(\alpha + \beta) = 1$ has also taken part in the analysis of the existence of the orbit. The condition $(\alpha + \beta + \gamma)(\alpha + \beta) = -1$ has been represented in Fig. 3.6 using a dotted line.

3.3.3   Two-periodic orbit (x_{AC}^*, x_{CA}^*)

The fixed points of the last two-periodic orbit (x_{AC}^*, x_{CA}^*) are given by the expressions

$$x_{AC}^* = \frac{\mu(1 + \alpha + \beta + \gamma) - \gamma\tau}{1 - \alpha(\alpha + \beta + \gamma)} \qquad \text{and} \qquad x_{CA}^* = \frac{\mu(1 + \alpha) - \alpha\gamma\tau}{1 - \alpha(\alpha + \beta + \gamma)},$$

whose existence conditions, taking into account that x_{AC}^* and x_{CA}^* are in S_A and S_C respectively, can be expressed as

$$x_{AC}^* < 0 \qquad \text{and} \qquad x_{CA}^* > \tau. \tag{3.18}$$

From the first part of (3.18), and taking into account that $1 - \alpha(\alpha + \beta + \gamma)$ is always positive, the (x_{AC}^*, x_{CA}^*) period-two orbit will exist if

$$\alpha + \beta + \gamma < -1 \quad \text{and} \quad \mu > \mu_{AB}^1,$$

or

$$\alpha + \beta + \gamma > -1 \quad \text{and} \quad \mu < \mu_{AB}^1.$$

From the second part of the condition (3.18), we obtain a complementary existence condition, expressed as

$$\mu > \tau \left(\frac{1 - \alpha(\alpha + \beta)}{1 + \alpha} \right) = \mu_{BC}^1.$$

Finally, the stability is given by the condition $\alpha(\alpha + \beta + \gamma) > -1$ and thus, (x_{AC}^*, x_{CA}^*) will be stable (attractor AC) if

$$\gamma > -\frac{1}{\alpha} - (\alpha + \beta).$$
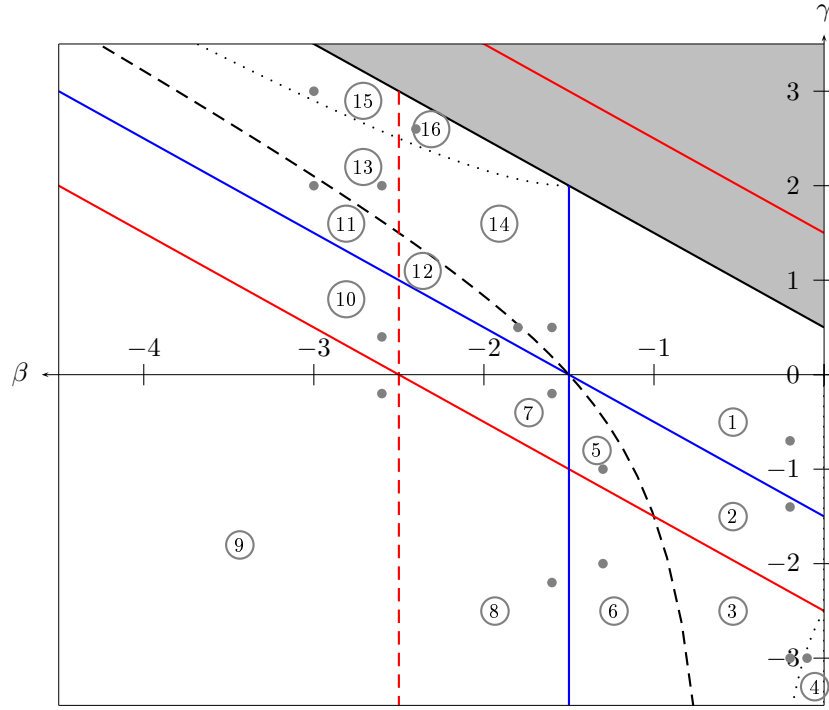
Figure 3.7. Existence and stability of the period 1 and 2 orbits in the parameter space $\{\beta, \gamma\}$ for $\alpha = 0.5$. The different attractors of each region are summarized in the Tables 3.2, 3.3, 3.4, 3.5 and 3.6. The grey dots represent the sets of parameters used in Figs. 3.8 and 3.9.

All these results are summarized in Fig. 3.7, where the existence and stability curves of period-one and two orbits split the parameter space $\{\beta, \gamma\}$ into sixteen zones. Though these curves have been obtained using the value $\alpha = 0.5$, the value of this parameter does not change qualitatively the regions in the parameter space $\{\beta, \gamma\}$. Each region has different attractors depending on the parameter μ, which are resumed in Tables 3.2, 3.3, 3.4, 3.5 and 3.6 depending on the relationship between the critical values μ_{AB}^0, μ_{BC}^0, μ_{AB}^1 and μ_{BC}^1.

To sum up, we summarized the most important results which can be obtained in the analysis of the existence and stability of the period 1 and 2 orbits:

- For $\mu < 0$, there is only the attractor A.

- Only the attractors C and AC can exist for higher values of μ.

- The attractor AC appears in all zones except in zone 1.

- For $\mu > \mu_{BC}^0$, the attractor C exists if $\alpha + \beta + \gamma > -1$ (Zones 1, 11-16).

- The attractor AC can coexist with the fixed point B in Zone 5, and C, in zones 11 and 12.

Zone	$\mu < \mu_{AB}^0$	$\mu_{AB}^0 < \mu < \mu_{BC}^0$	$\mu_{BC}^0 < \mu < \mu_{AB}^1$	$\mu > \mu_{AB}^1$
1	A	B	C	C
2	A	B	c, BC	c, AC
3	A	B	c, BC	c, ac
4	A	B	c, bc	c, ac

Table 3.2. Different scenarios of the map in zones 1 to 4 ($\mu_{AB}^0 < \mu_{BC}^0 < \mu_{AB}^1$)

Zone	$\mu < \mu_{AB}^0$	$\mu_{AB}^0 < \mu < \mu_{AB}^1$	$\mu_{AB}^1 < \mu < \mu_{BC}^0$	$\mu > \mu_{BC}^0$
5	A	B	B, bc, AC	c, AC
6	A	B	B, bc, ac	c, ac

Table 3.3. Different scenarios of the map in zones 5 to 6 ($\mu_{BC}^1 < \mu_{AB}^1 < \mu_{BC}^0$)

Zone	$\mu < \mu_{AB}^0$	$\mu_{AB}^0 < \mu < \mu_{BC}^1$	$\mu_{BC}^1 < \mu < \mu_{BC}^0$	$\mu > \mu_{BC}^0$
7	A	b, AB	b, AC	c, AC
8	A	b, AB	b, ac	c, ac
9	A	b, ab	b, ac	c, ac
10	A	b, ab	b, AC	c, AC

Table 3.4. Different scenarios of the map in zones 7 to 10 ($\mu_{AB}^1 < \mu_{BC}^1 < \mu_{BC}^0$)

	$\mu < \mu_{AB}^0$	$\mu_{AB}^0 < \mu < \mu_{BC}^1$	$\mu_{BC}^1 < \mu < \mu_{BC}^0$	$\mu_{BC}^0 < \mu < \mu_{AB}^1$	$\mu > \mu_{AB}^1$
11	A	b, ab	b, AC	C, bc, AC	C
12	A	b, AB	b, AC	C, bc, AC	C

Table 3.5. Different scenarios of the map in zones 11 to 12 ($\mu_{AB}^1 < \mu_{BC}^1 < \mu_{BC}^0$)

3.4   BC bifurcations of the fixed points and period-two solutions

As it has been introduced above, the fixed points A and C present a border-collision bifurcation when they cross the boundaries Σ_{AB} and Σ_{BC} respectively. In addition, B can have two border-collision bifurcations when the attractor crosses the boundaries

	$\mu < \mu_{AB}^0$	$\mu_{AB}^0 < \mu < \mu_{BC}^1$	$\mu_{BC}^1 < \mu < \mu_{AB}^1$	$\mu_{AB}^1 < \mu < \mu_{BC}^0$	$\mu > \mu_{BC}^0$
13	A	b, ab	b, AC	b, BC	C
14	A	b, AB	b, AC	b, BC	C
15	A	b, ab	b, AC	b, bc	C
16	A	b, AB	b, AC	b, bc	C

Table 3.6. Different scenarios of the map in zones 13 to 16 ($\mu_{AB}^1 < \mu_{BC}^1 < \mu_{BC}^0$)

Σ_{AB} or Σ_{BC}. Dealing with the period-two orbits, AB or BC will present another bifurcation when the fixed point x_{AB}^* or x_{BC}^* reach the boundaries Σ_{AB} and Σ_{BC} respectively and finally, orbit AC will present two bifurcations when the fixed points x_{AC}^* and x_{CA}^* cross the boundaries Σ_{AB} or Σ_{BC} respectively.

The different dynamical scenarios in which border-collision bifurcations are involved can be seen in Fig. 3.8 and Fig. 3.9, where sixteen bifurcation diagrams have been depicted using μ as the varying parameter and using sets of parameters placed in each region defined previously in Fig. 3.7. Moreover, in Fig. 3.10 two bifurcation diagram are depicted using the same set of parameters in the Zone 6 (Fig. 3.10a,b), 10 (Fig. 3.10c) and 13 (Fig. 3.10d) to show the coexistence of two attractors.

In Table 3.7, the different border-collision bifurcations appeared at the critical values of μ are classified using the strategy of classification presented in [31], which is based on the analysis of the eigenvalues of the maps involved in each bifurcation at the bifurcation point and has been reviewed in Chapter 2. Notice that in all cases $\sigma_A^+ = \sigma_A^- = \sigma_B^+ = \sigma_C^+ = 0$ and $\sigma_{AB}^+ = \sigma_{AC}^+ = 0$. Depending on the values of σ_B^-, σ_C^-, σ_{AB}^-, σ_{BC}^-, σ_{AC}^- and σ_{BC}^+ at the bifurcation point, the scenarios found are persistence of the fixed point or the period-2 orbit, non-smooth fold and non-smooth period-doubling. Furthermore, in some regions it is needed to analyze the existence and stability of higher periodic orbits.

(a) Zone 1: $(-0.2, -0.7)$ (b) Zone 2: $(-0.2, -1.4)$ (c) Zone 3: $(-0.2, -3.0)$

(d) Zone 4: $(-0.1, -3.0)$ (e) Zone 5: $(-1.3, -1.0)$ (f) Zone 6: $(-1.3, -2.0)$

(g) Zone 7: $(-1.6, -0.2)$ (h) Zone 8: $(-1.6, -2.2)$ (i) Zone 9: $(-2.6, -0.2)$
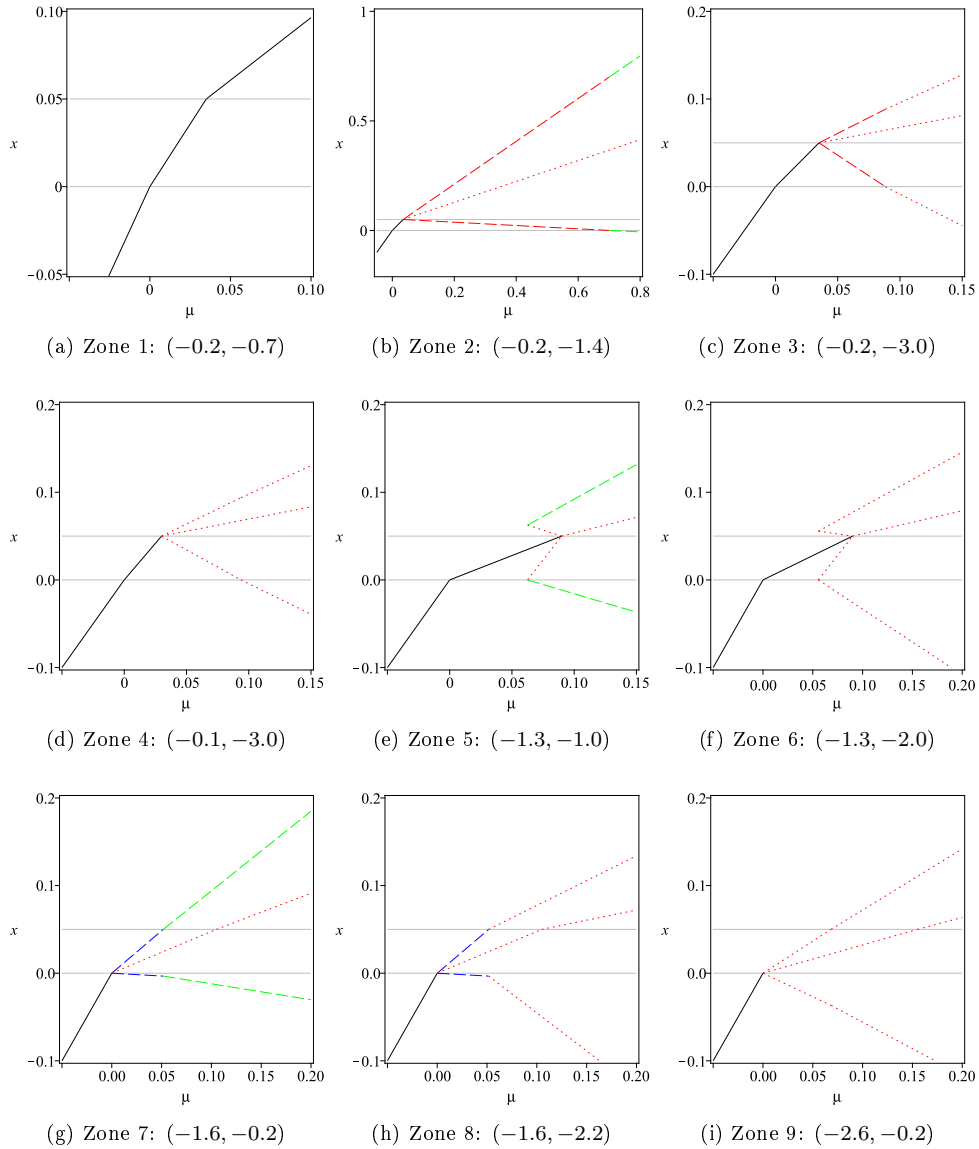
Figure 3.8. Bifurcation diagrams with μ as varying parameter for negative values of γ. Parameters: $\alpha = 0.5$, $\tau = 0.05$ and (β, γ) are in the captions. Legend: Red doted lines for unstable orbits, black solid lines for stable one-periodic orbits and blue, red and green dashed lines for the orbits AB, BC and AC respectively.

(a) Zone 10: $(-2.6, 0.4)$

(b) Zone 11: $(-3.0, 2.0)$

(c) Zone 12: $(-1.8, 0.5)$

(d) Zone 13: $(-2.6, 2.0)$

(e) Zone 14: $(-1.6, 1.5)$

(f) Zone 15: $(-3.0, 3.0)$

(g) Zone 16: $(-2.4, 2.6)$
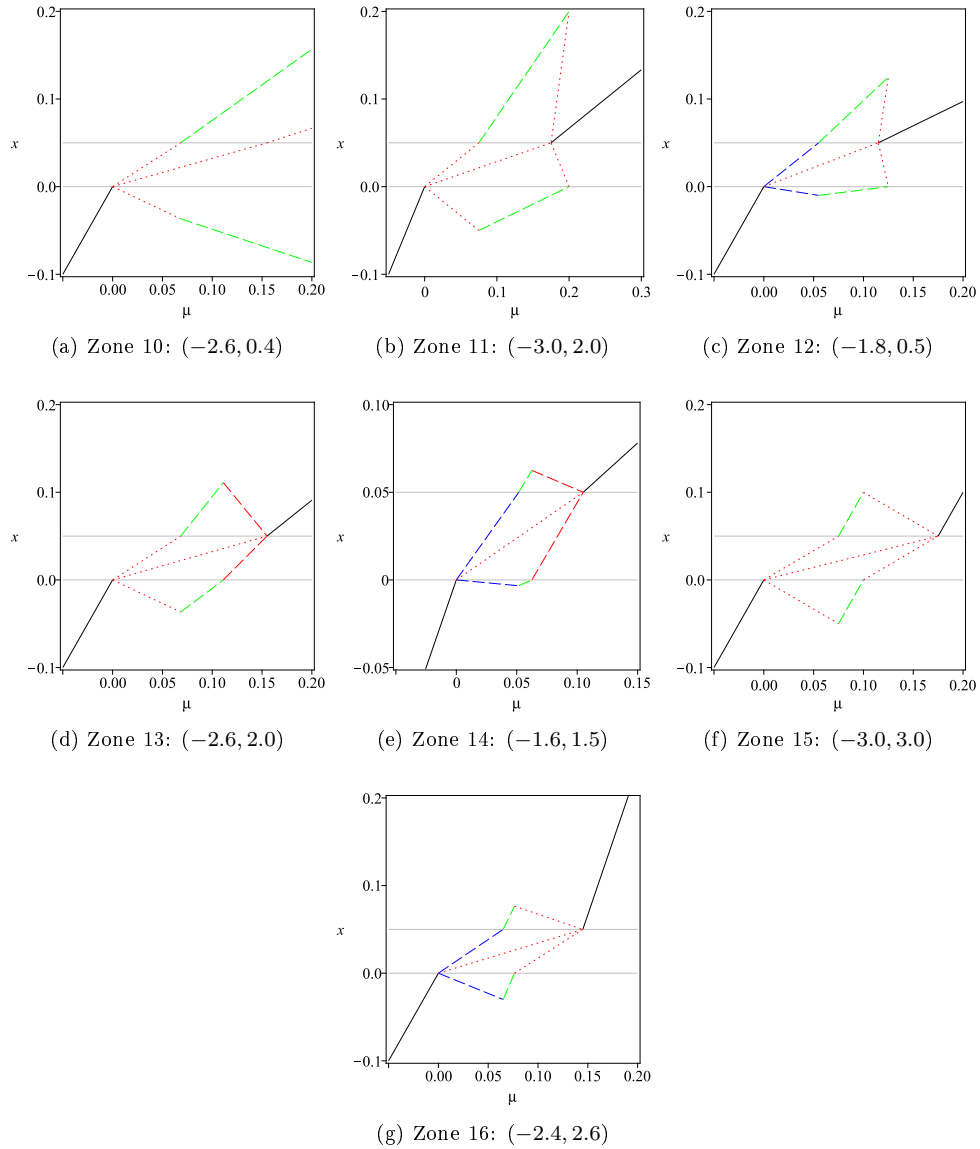
Figure 3.9. Bifurcation diagrams with μ as varying parameter for positive values of γ. Parameters: $\alpha = 0.5$, $\tau = 0.05$ and (β, γ) are in the captions. Legend: Red doted lines for unstable orbits, black solid lines for stable one-periodic orbits and blue, red and green dashed lines for the orbits AB, BC and AC respectively.

(a) Zone 6: Left-Right

(b) Zone 6: Right-Left
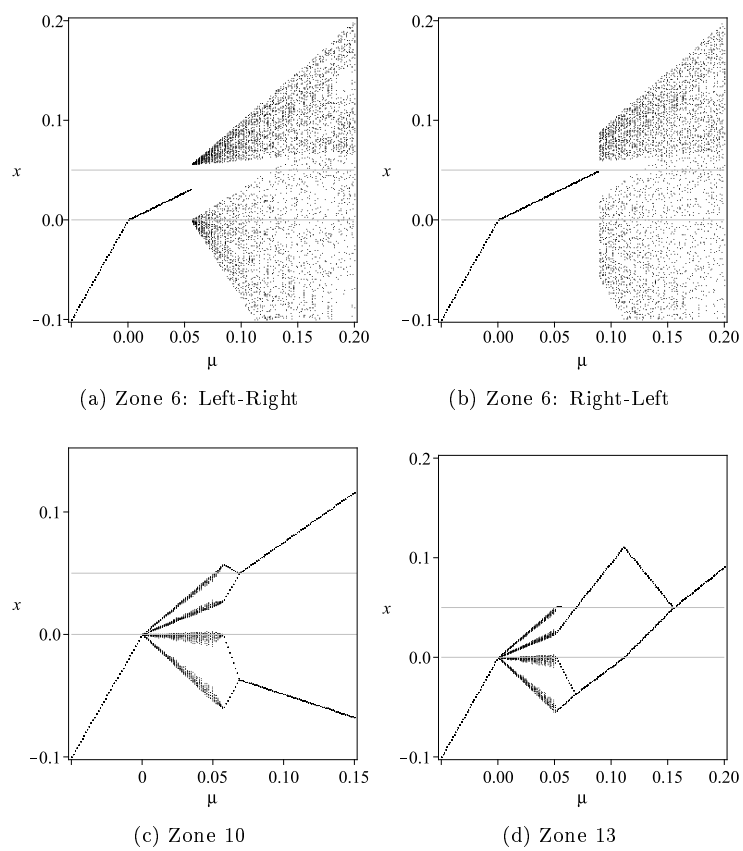
(c) Zone 10

(d) Zone 13

Figure 3.10. Bifurcation diagrams with μ as varying parameter. Parameters (α, β, γ and τ): (a,b) Zone 6: $(0.5, -1.3, -2.0, 0.05)$, (c) Zone 10: $(0.5, -2.6, 0.4, 0.05)$, (d) Zone 13: $(0.5, -2.6, 2.0, 0.05)$.

Zones	μ	Scenario	σ_B^-	σ_C^-	σ_{AB}^-	σ_{BC}^-	σ_{AC}^-	σ_{BC}^+	Type
$1..6$	μ^0_{AB}	$A \leftrightarrow B$	0						P
$7,8,12,14$	μ^0_{AB}	$A \leftrightarrow b, AB$	1		0				NS PD
$9..11,13$	μ^0_{AB}	$A \leftrightarrow b, ab$	1		1				HPO/C
1	μ^0_{BC}	$B \leftrightarrow C$	0	0					P
$2..3$	μ^0_{BC}	$B \leftrightarrow c, BC$	0	1		0		0	NS PD
4	μ^0_{BC}	$B \leftrightarrow c, bc$	0	1		1		0	HPO/C
$5..6$	μ^0_{BC}	$B, bc \leftrightarrow c$	0	1		1		1	NS PD
$7..10$	μ^0_{BC}	$b \leftrightarrow c$	1	1					P
$11,12$	μ^0_{BC}	$b \leftrightarrow C, bc$		0			1		NS PD
$13,14$	μ^0_{BC}	$C \leftrightarrow b, BC$		0			1		NS PD
$2,14$	μ^1_{AB}	$BC \leftrightarrow AC$				0	0	0	P
$4,13$	μ^1_{AB}	$bc \leftrightarrow ac$				1	1	0	P
3	μ^1_{AB}	$BC \leftrightarrow ac$				0	1	0	HPO/C
$5,11,12$	μ^1_{AB}	$\emptyset \leftrightarrow bc, AC$				0	0	1	NS F
6	μ^1_{AB}	$\emptyset \leftrightarrow bc, ac$				0	1	1	NS F
$7,12,14$	μ^1_{BC}	$AB \leftrightarrow AC$			0		0		P
$10,11,13$	μ^1_{BC}	$ab \leftrightarrow AC$			1		0		HPO/C
9	μ^1_{BC}	$ab \leftrightarrow ac$			1		1		P
8	μ^1_{BC}	$AB \leftrightarrow ac$			0		1		HPO/C

Table 3.7. Bifurcations of the fixed points and two-periodic orbits. P: persistence, NS PD: Non-smooth period-doubling, NS F: Non-smooth fold, HPO/C: higher periodic orbit or chaos.

3.5   Higher periodic orbits and chaos

The map exhibits a rich variety of higher periodic orbits (see Fig. 3.11) due to the
presence of two boundaries. In this section, some results dealing with these orbits will
be discussed. Nevertheless, a complete classification of the possible scenarios involving
higher periodic orbits is out of the scope of this dissertation.

In contrast to the higher periodic orbits in a two-piece map, other conditions of ex-
istence must be taken into consideration. The set of periodic orbits of the forms
A^kB/a^kb and B^kC/b^kc will always present a border-collision bifurcation when one of
the fixed points of the attractor reaches one of the boundaries. For A^kB/a^kb orbits,
the border-collision will be given when the fixed point placed in S_B reaches the bound-
ary Σ_{BC} (Fig. 3.11a,b), whereas for B^kC/b^kc orbits, the bifurcation will appear when
the lowest fixed point in S_B reaches the boundary Σ_{AB} (Fig. 3.11c). Then, differ-
ent scenarios can appear as persistence (Fig. 3.11a), period-doubling (Fig. 3.11c) or
chaos (Fig. 3.11b). The border-collision bifurcation of the A^kB and B^kC modes will
be given at the critical values

$$\mu_{BC}^k = \tau\frac{1 - \alpha^k(\alpha + \beta)}{1 - \alpha^{k+1}}(1 - \alpha),$$

$$\mu_{AB}^k = -\frac{-\gamma\tau(1 - (\alpha + \beta))}{1 + \gamma - (\alpha + \beta)^k(\alpha + \beta + \gamma)},$$

respectively.

Although the A^kB/a^kb and B^kC/b^kc modes cannot be admissible for high values of
μ, from a critical value of μ, the orbits of the form A^kC/a^kc can appear and will
not present border-collision bifurcations as μ increases (see Fig. 3.11d). Due to the
fact that the fixed point placed in S_C to has to be greater than Σ_{BC} we obtain the
following condition of μ

$$\mu > \tau\frac{1 - \alpha^k(\alpha + \beta)}{1 - \alpha^{k+1}}(1 - \alpha) = \mu_{BC}^k.$$

In addition, the highest point in S_A must be negative, and hence

$$\mu > -\frac{-\gamma\tau(1 - \alpha)\alpha^{k-1}}{1 - \alpha^{k-1}((\alpha - 1)(\alpha + \beta + \gamma) + \alpha)} = \mu_{AC}^k.$$

3.6   Basins of attraction

The study of the existence and stability of the period-one and two orbits has shown
the coexistence of the attractors B and AC in the zone 5, and the attractors C and
AC in the zones 11 and 12. In both cases, bc is an admissible period-two orbit and
takes a relevant part in the basin of attraction of each pair of attractors.

(a) Zone 9, $(0.5, -3.6, -0.2, 0.1)$ (b) Zone 9, $(0.5, -3.6, -1.2, 0.017)$

(c) Zone 4, $(0.5, -0.15, -5, 0.4)$ (d) Zone 6, $(0.5, -1.4, -2.9, 0.69)$
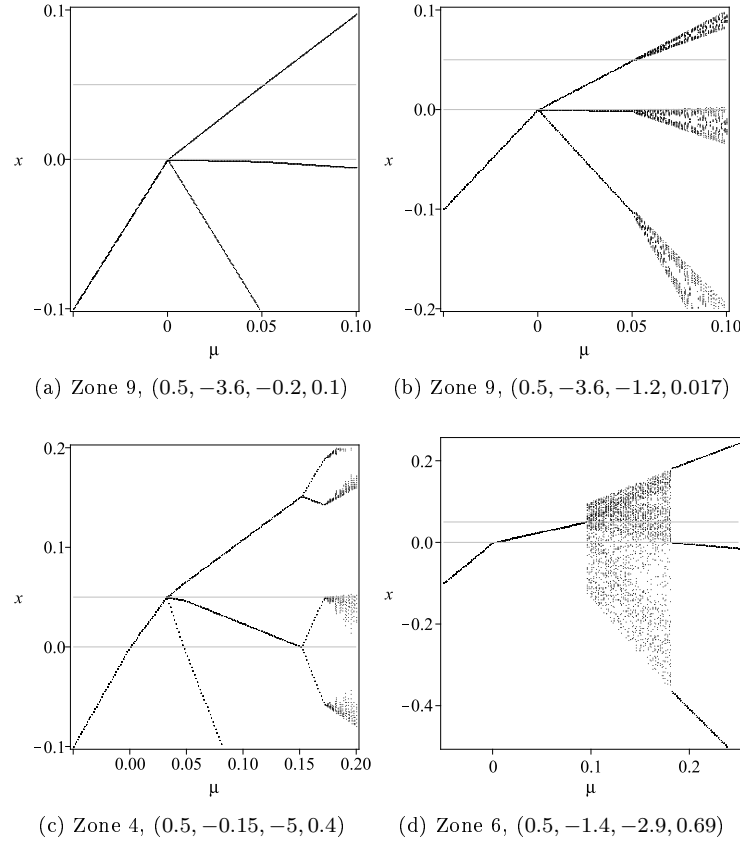
Figure 3.11. Bifurcation diagrams with μ as varying parameter. Parameters (α, β, τ, γ and μ) are in the caption.

Let us study the first case, which is illustrated in Fig. 3.12. Basins of attractions for the solutions C and AC in zone 11 and 12 can be obtained similarly. As it can be appreciated, the basin of attraction of B (blue) is composed by infinite segments, each of which surrounded by segments of the basin of attraction of the orbit AC (green). The *main* basin, which surrounds the fixed point B, is limited by the fixed points of the unstable orbit (x^*_{BC}, x^*_{CB}). The next segment of this basin is bounded by x'_{A1} and x''_{A1} (left side) and x'_{C1} and x''_{C1} (right side), being

$$x^*_{CB} = F_A(x'_{A1}), \qquad x^*_{BC} = F_A(x''_{A1}),$$

$$x'_{A1} = F_C(x'_{C1}), \qquad x''_{A1} = F_C(x''_{C1}).$$

Therefore, the expressions for x'_{A1}, x''_{A1}, x'_{C1} and x''_{C1} are given by

$$x'_{A1} = \frac{1}{\alpha}\left(x^*_{CB} - \mu\right), \qquad x''_{A1} = \frac{1}{\alpha}\left(x^*_{BC} - \mu\right),$$

$$x'_{C1} = \frac{1}{\alpha\,(\alpha + \beta + \gamma)}\,(x^*_{CB} - \mu - (\mu - \gamma\tau)\alpha)\,,$$

$$x''_{C1} = \frac{1}{\alpha\,(\alpha + \beta + \gamma)}\,(x^*_{BC} - \mu - (\mu - \gamma\tau)\alpha)\,.$$

The remainder segments of the basin are limited by x'_{An} and x''_{An} in the region S_A and x'_{Cn} and x''_{Cn} in S_C (see Fig. 3.12), whose expressions are given by

$$x'_{An} = \frac{x^*_{CB} - \mu\left(1 + \alpha + \alpha^2 + \cdots\alpha^{n-1}\right)}{\alpha^n} = \frac{1}{\alpha^n}\left(x^*_{CB} - \frac{\mu(1 - \alpha^n)}{1 - \alpha}\right)$$

$$x''_{An} = \frac{x^*_{BC} - \mu\left(1 + \alpha + \alpha^2 + \cdots\alpha^{n-1}\right)}{\alpha^n} = \frac{1}{\alpha^n}\left(x^*_{BC} - \frac{\mu(1 - \alpha^n)}{1 - \alpha}\right)$$

$$x'_{Cn} = \frac{x'_{An} - \mu + \gamma\tau}{\alpha + \beta + \gamma} = \frac{1}{\alpha^n(\alpha + \beta + \gamma)}\left(x^*_{CB} - \frac{\mu(1 - \alpha^n)}{1 - \alpha} - (\mu - \gamma\tau)\alpha^n\right)$$

$$x''_{Cn} = \frac{x''_{An} - \mu + \gamma\tau}{\alpha + \beta + \gamma} = \frac{1}{\alpha^n(\alpha + \beta + \gamma)}\left(x^*_{BC} - \frac{\mu(1 - \alpha^n)}{1 - \alpha} - (\mu - \gamma\tau)\alpha^n\right)$$

being $n = 1, 2, 3.. + \infty$.

The size of each basin of the attractor B is given by the expressions

$$x'_{An} - x''_{An} = \frac{x^*_{CB} - x^*_{BC}}{\alpha^n}$$

$$x''_{Cn} - x'_{Cn} = \frac{x^*_{BC} - x^*_{CB}}{\alpha^n(\alpha + \beta + \gamma)}$$

which increases with n.
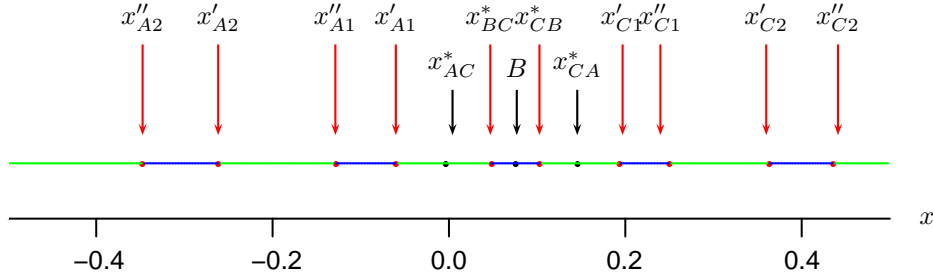
Figure 3.12. Basin of attraction in region 5. Parameters $(\alpha, \beta, \gamma, \tau, \mu)$: $(0.8, -1.79, -0.2, 0.1, 0.15)$. Colors: Green (x^*_{AC}, x^*_{CA}), blue (B).

3.7   Non-smooth dynamics for $\alpha = 1$

The discrete-time analysis of the SITITO converter that will be explained in the following chapters reveals that the dynamics of this converter governed by the SPC

Figure 3.13. Existence and stability of the period 1 and 2 orbits for $\alpha = 1$.

control can be modelled by means of a three-piece piecewise-linear map. Similarly, the discrete-time map that describes the dynamics of the converter under the control IC is composed by three or four trams. Due to the fact that the first slope of both maps will be established to 1, we have been motivated to particularize the analysis realized above for $\alpha = 1$.

The first consequence produced when α is forced to 1 is the disappearance of the fixed point x_A^*. In addition, the stability conditions of the attractors AC and AB becomes equivalent to the stability of x_C^* and x_B^* respectively. As a result, the possible scenarios are significantly reduced as Fig. 3.13 illustrates.

Moreover, for negative values of γ, the only possible attractors of the map are: C, placed in zone 1, and BC, which only appears in zone 3. Therefore, the coexistence of B and AC in zone 5 is now avoided. Zones 7 and 8, in which AB was allowed, now have collapsed and disappeared. Notice that BC is the only period-two orbit permitted. Higher periodic orbits such as $B^k C$ can also be found in zone 4. Otherwise, for positive values of γ, C is a feasible attractor which can be found in zones 1, 11 and 13. In addition, in the zone 11 the attractor AC coexists with C. Notice that now both attractors loose the stability simultaneously.

3.8   Conclusions

The existence and stability conditions of the fixed points and period-two orbits have been obtained in a three-piece piecewise-linear map in a restricted range of parameters. Furthermore, the border-collision bifurcations, which can be produced by these attractors, have been detected and classified.

This study has revealed an increment in the complexity of the dynamical behavior in comparison with the two-piece piecewise-lineal continuous map. Firstly, the number of different patterns of bifurcation reported has increased significantly owing to, in part, the presence of two boundaries. This fact has implied the existence of different critical values of μ, which can also appear in a different order of occurrence, incrementing the variety of scenarios. Furthermore, the study has shown different regions in the parameter space in which there are coexisting attractors, such as B and AC or C, and AC and therefore, hysteresis in the bifurcation diagrams. The analytical expressions which define the boundaries of the basin of attraction have been developed for the first pair of attractors.

An overview of the existence of higher periodic orbit has been also included. Nevertheless, a complete classification of the higher periodic orbits will be the subject of future research.

Finally, the bifurcation analysis has been particularized for $\alpha = 1$. These results will permit us to improve the comprehension of the dynamics of the SITITO converter governed by SPC and, partially, by IC control.

Chapter 4

Analysis of the SITITO converter with Single-Phase Control

In this chapter, a Single-Inductor Two-input Two-output (SITITO) dc-dc converter, which is capable of regulating two asymmetric outputs with different polarities by means of a PWM control, will be analyzed. As a first step, averaging technique is used to deal with low-scale bifurcations, then discrete-time models are developed to predict bifurcations connected to the ripple of the inductor current and to account for non-smooth bifurcations. The discrete formulation will be developed according to the formalism used in the previous chapter.

4.1 Description of the dc-dc converter

4.1.1 Power stage description

The simplified scheme of the power stage of a Single-Inductor Two-Input Two-Output (SITITO) dc-dc converter is shown in Fig. 4.1. This stage includes the unregulated source voltage V_{IN}, the inductor with inductance L and series resistance r_L and the positive and negative loads with resistance R_P and R_N and filter capacitance C_P and C_N respectively. Two pair of switches are also required in the circuit, which will be
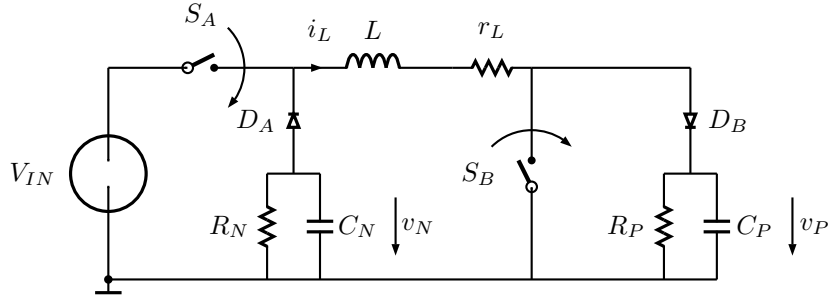
Figure 4.1. Schematic of the power stage of a single inductor dc-dc converter with positive and negative loads.

implemented by means of two MOSFET transistors, S_A and S_B and two diodes D_A and D_B. The action of S_A and S_B will be determined by the control of the converter, whereas the action of both diodes is complementary to the corresponding controlled switches S_A and S_B. Therefore, S_A can connect the inductor to the source (ON case) or to the negative channel (OFF case) whereas S_B can connect the other terminal of the inductor to the ground (ON case) or to the positive channel (OFF case).

Associated to the energy storage elements of this stage (the inductor and the positive and negative filter capacitors) are the following three state variables: current i_L, and both capacitor voltages v_P and v_N respectively.

4.1.2   Operation of the converter

The operation of this converter is based on suitable toggling among different topologies given by the convenient action of both switches. In the continuous conduction mode (CCM), where the inductor current is always defined positive, four feasible topologies can operate in converter, whose schemes are represented in Fig. 4.2 and summarized in Table 4.1. The $\mathcal{T}_1$ topology (see Fig. 4.2a) is given when both controlled switches are ON and, consequently, both diodes are open. In this topology, the unregulated source transfers energy to the inductor by increasing i_L. The $\mathcal{T}_2$ configuration (see Fig. 4.2b) is operating when the switch S_B changes to OFF while S_A remains ON, then the inductor transfers energy only to the positive load, whereas the $\mathcal{T}_3$ (Fig. 4.2c) configuration appears when the switch S_A changes to OFF while S_B remains ON, then the inductor transfers energy only to the negative load. In the last topology $\mathcal{T}_4$ (Fig. 4.2d), which corresponds to both switches open, the energy flows from the inductor to both positive and negative loads, so this configuration corresponds to a series connection of the loads and the inductor.

(a) $\mathcal{T}_1$: S_A ON and S_B ON

(b) $\mathcal{T}_2$: S_A ON and S_B OFF

(c) $\mathcal{T}_3$: S_A OFF and S_B ON

(d) $\mathcal{T}_4$: S_A OFF and S_B OFF
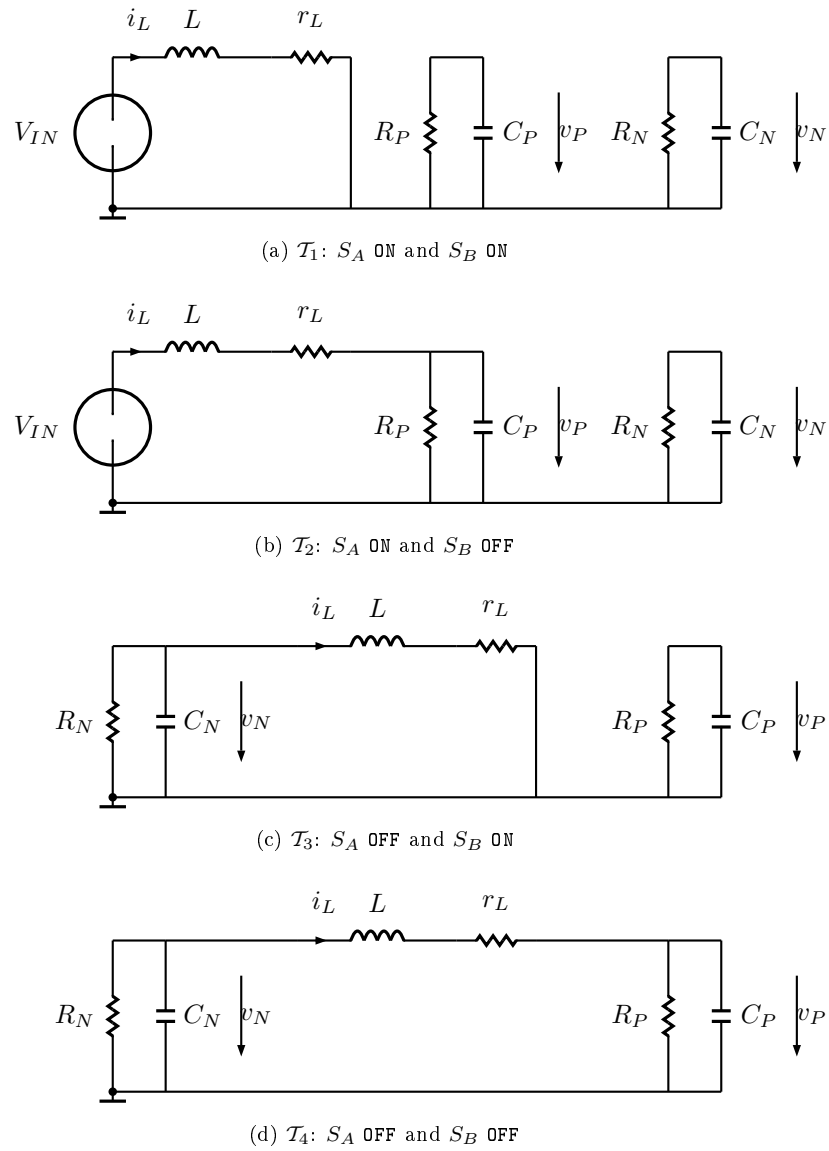
Figure 4.2. The four feasible topologies of the SITITO converter in CCM.

	S_A	S_B
$\mathcal{T}_1$	ON	ON
$\mathcal{T}_2$	ON	OFF
$\mathcal{T}_3$	OFF	ON
$\mathcal{T}_4$	OFF	OFF

Table 4.1. Definition of the topologies of the SITITO converter in CCM.

The discontinuous conduction mode (DCM) can also be found in the SITITO converter proposed and hence, another topology must be taken into account in the dynamics of the converter when the inductor current drops to zero. In this topology, both diodes and both transistors remain open.

As it has been said before, the operation of the converter will alternate among the different topologies to achieve the regulation. Notice that if the switching sequence reached is $\mathcal{T}_1 \to \mathcal{T}_2$, the circuit will work as a boost converter being the negative output voltage $v_N = 0$. Similarly, if the switching sequence becomes $\mathcal{T}_1 \to \mathcal{T}_3$, the circuit will operate as a buck-boost converter and hence, $v_P = 0$.

4.1.3   Control PWM

The aim of the control of this converter is the regulation of voltage outputs $v_P(t)$ and $v_N(t)$ to adjust them to the corresponding desired inputs V_P and V_N respectively, which, in general, will be unbalanced. The control must provide two binary signals $u_A(t)$ and $u_B(t)$ in order to drive the corresponding switches S_A and S_B and thus, two loops have been included to the control to achieve the regulation.

Figure 4.3 shows a diagram of the control proposed for the converter. As it can be seen in the figure, the control will be given, as usual in PWM controllers, by the comparison of two signals. Particularly, the control compares the peak references $v_A(t)$ and $v_B(t)$, which will include a modulating signal $v_M(t)$ of period T, with $v_I(t)$. This signal is proportional to the inductor current and will be common for both channels. Its expression is given by

$$v_I(t) = r_S i_L. \tag{4.1}$$

where r_S is the sensing resistance.

The expressions for both peak references $v_A(t)$ and $v_B(t)$ are given by

$$v_A(t) = g_{PA}(V_P - v_P(t) - \sigma_P(t)) + g_{NA}(v_N(t) - V_N + \sigma_N(t)) - g_{FA}V_{IN} + v_M(t), \tag{4.2}$$

$$v_B(t) = g_{PB}(V_P - v_P(t) - \sigma_P(t)) + g_{NB}(v_N(t) - V_N + \sigma_N(t)) - g_{FB}V_{IN} + v_M(t). \tag{4.3}$$
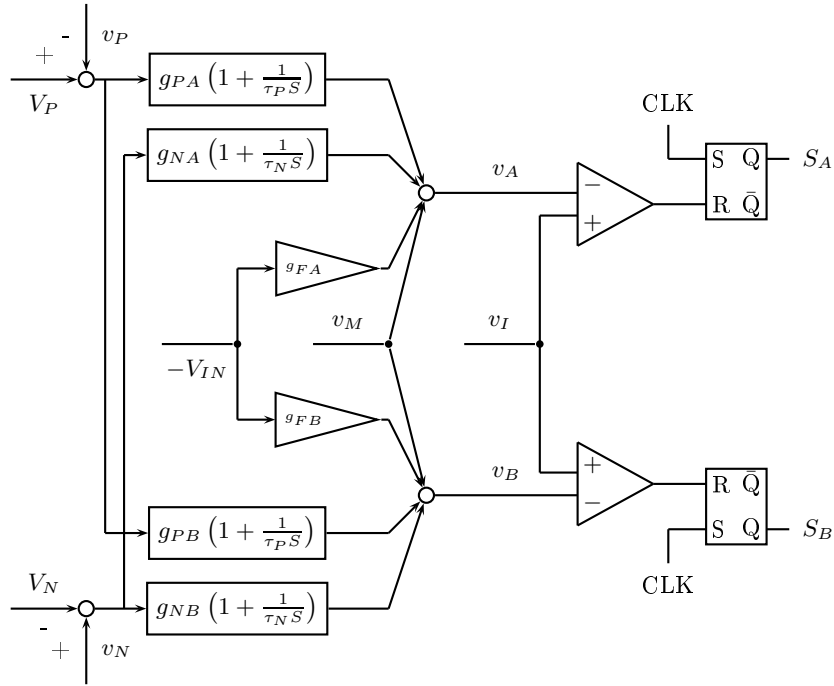
Figure 4.3. Schematic of the PWM control of the SITITO converter.

Finally, the integral error variables $\sigma_P(t)$ and $\sigma_N(t)$ are given as follows

$$\sigma_P(t) = \frac{1}{\tau_P} \int (v_P(t) - V_P) \, \mathrm{dt}, \tag{4.4}$$

$$\sigma_N(t) = \frac{1}{\tau_N} \int (v_N(t) - V_N) \, \mathrm{dt}, \tag{4.5}$$

where τ_P and τ_N are the corresponding time constants associated with the integral terms. $\sigma_P(t)$ and $\sigma_N(t)$ will add two state variables of the system.

Notice that each peak references $v_A(t)$ and $v_B(t)$ include the following terms:

- Two proportional integral terms with gains g_{PA} and g_{NA} (g_{NB} and g_{PB}) to minimize error signals.

- A feedforward term to prevent from disturbances of the source, whose gain is g_{FA} (g_{FB}).

- A modulating sawtooth function, v_M, whose expression will depend on the state of the switches that must be synchronized. Particularly, in the control proposed
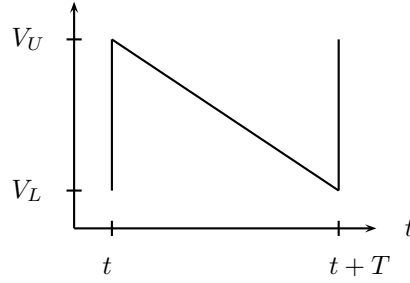
Figure 4.4. The modulating signal $v_M(t)$

here, the ON state of both channels will be synchronized with an external clock. Therefore, the expression of the modulating signal must be given by

$$v_M(t) = V_U - (V_U - V_L) \operatorname{mod}\left(\frac{t}{T}, 1\right),$$

being V_U and V_L the upper and lower value and T, its period (see Fig. 4.4).

In order to avoid multiple switching during a single period, two Set-Reset edge-triggered Flip-Flops are included taking into account that their configuration will depend on the synchronized state. In case of synchronizing the ON state, the external clock must be connected to the SET input of the Flip-Flops of both channels and thus, the ON state of both switches will be forced to be synchronized with the clock, which will also imply the simultaneity of both ON switches. Conversely, the signal v_I must be connected to the RESET terminal. Consequently, the OFF state of S_A and S_B switches, which are outputs of the Q channels, will be reached when conditions (4.6) and (4.7) are fulfilled, thus these switches will be asynchronous and, in general, non simultaneous.

$$v_A(t) = v_I(t), \tag{4.6}$$

$$v_B(t) = v_I(t). \tag{4.7}$$

Before presenting the different modes of operation of the converter, let us define the duty cycles d_A and d_B as the time interval during which the switches S_A and S_B remain closed (ON) respectively, and thus

$$d_A = \frac{t_{A,ON}}{T},$$

$$d_B = \frac{t_{B,ON}}{T},$$

where $t_{A,ON}$ ($t_{B,ON}$) is the time interval for which the switch S_A (S_B) is in the state ON. Let us also define the binary signals u_A and u_B. Their values are related with the state
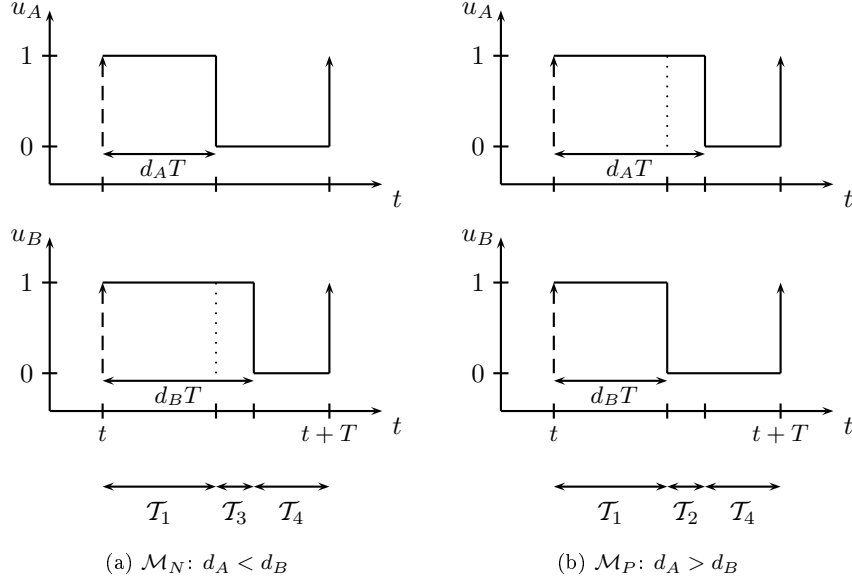
Figure 4.5. The two main modes of operation of the converter: $\mathcal{M}_N$ and $\mathcal{M}_P$.

of the corresponding switch S_A and S_B: 0 if open (OFF) or 1 if closed (ON). Therefore, both signals will be fixed to 1 at the beginning of each period, becoming 0 when its corresponding condition (4.6) or (4.7) is fulfilled. Then, this value is maintained until the end of the period.

Depending on the order of occurrence of conditions (4.6) or (4.7) during a certain period of the modulating signal, different scenarios turn up. Figure 4.5 shows the two cases in which both conditions are satisfied during a period T and consequently, three topologies are involved. The critical condition that distinguishes both models of operation is given by

$$d_A - d_B = 0. \tag{4.8}$$

In Fig. 4.5a, $d_A < d_B$ and thus, S_A changes to OFF while S_B remains in the ON state, and then S_B changes to OFF. Therefore, the sequence of topologies will be $\mathcal{T}_1 \leftrightarrow \mathcal{T}_3 \leftrightarrow \mathcal{T}_4$. This mode of operation will be called $\mathcal{M}_N$. Similarly, the second mode (see Fig. 4.5b), $(d_A > d_B)$ in which firstly S_B changes to OFF while S_A remains in ON, will be called $\mathcal{M}_P$, being the sequence of topologies $\mathcal{T}_1 \leftrightarrow \mathcal{T}_2 \leftrightarrow \mathcal{T}_4$. The evolution of the state variables i_L, v_P and v_N including the references v_A and v_B are depicted in Fig. 4.6 for both modes of operations.

Besides these cases, other scenarios can appear if one or both switches do not change their ON state, although the dynamics of the converter cannot be stable. These modes

(a) $\mathcal{M}_P$: $r_S i_L$

(b) $\mathcal{M}_N$: $r_S i_L$

(c) $\mathcal{M}_P$: v_P

(d) $\mathcal{M}_N$: v_P

(e) $\mathcal{M}_P$: v_N

(f) $\mathcal{M}_N$: v_N
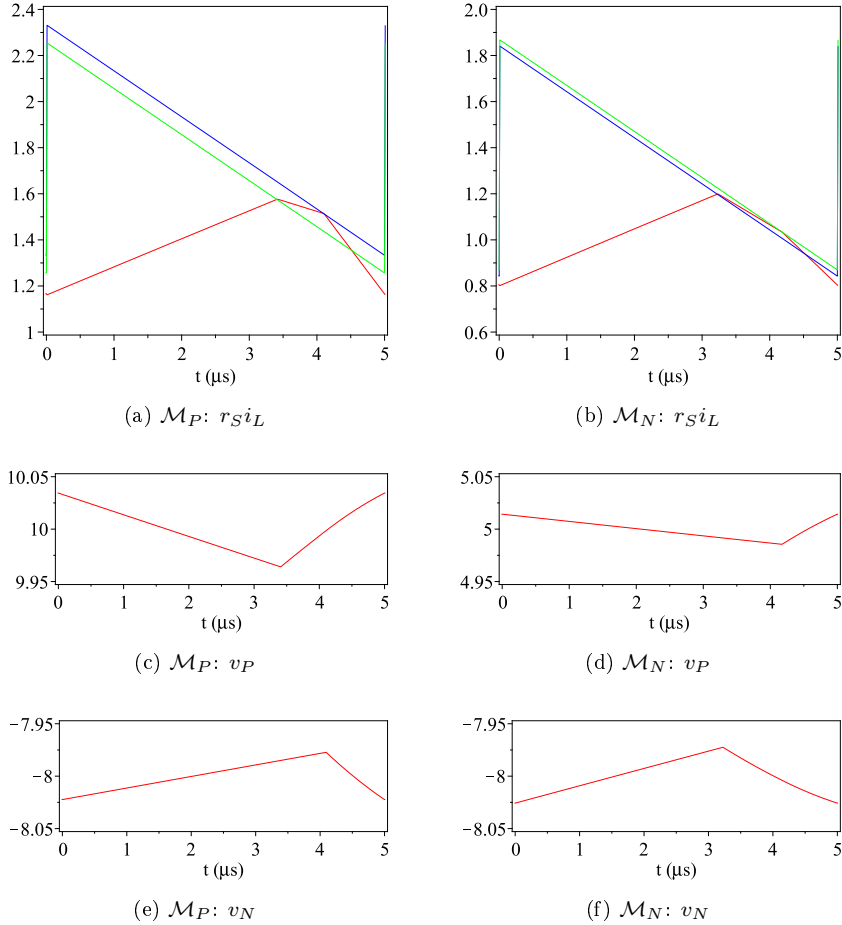
Figure 4.6. Evolution of following signals: (a,b) the inductor current, more precisely v_I, (red) and the reference signals v_A (blue) and v_B (green); (c,d) the positive and (e,f) negative capacitor voltages. The parameters are in Table 4.2 except in mode $\mathcal{M}_N$: $R_P = 33\,\Omega$, $R_N = 22\,\Omega$ and $V_P = 5.0\,\text{V}$.

Parameter	Value	Parameter	Value
V_{IN}	6.0 V	r_S	1 Ω
L	47 µH	r_L	0.2 Ω
V_U	1.0 V	V_L	0.0 V
V_P	10.0 V	V_N	−8.0 V
C_P	22 µF	C_N	22 µF
R_P	22 Ω	R_N	33 Ω
τ_P	50 µs	τ_N	50 µs
g_{PA}	0.02	g_{NA}	0.0
g_{PB}	0.0	g_{NB}	0.02
g_{FA}	0.0	g_{FB}	0.0
$f_s = 1/T$	200 kHz		

Table 4.2. Parameter values used in numerical simulations.

will be called $\mathcal{M}_O$, if neither of the commutations is given and $\mathcal{M}_{SP}$ or $\mathcal{M}_{SN}$, when only the condition (4.6) or (4.7) is satisfied.

4.2 Closed loop mathematical modeling

4.2.1 Switched model

Switched models are useful tools to simulate the dynamics of switching power converters, since they contain the dynamics of all configurations of the converter by means of appropriate binary signals. The dynamics can be studied straightforward from the corresponding differential equations of every topology, which can be obtained easily from Fig. 4.2 using Kirchhoff's laws, and the initial conditions of the state variables. Notice that the differential equations are linear and the vector fields are, in general, discontinuous in the transitions between topologies. Therefore, the system can be classified as a piecewise-linear system (PWL). Particularly, the switching instants can be fixed by solving (4.6) or (4.7), depending on the sequence of topologies. The value of the state variables at these points will become the initial conditions of the following topology. Using this methodology, the continuous evolution of all state variables can be obtained despite the discontinuity in the vector fields.

Let us define the general form of the fifth-dimensional system as follows

$$\dot{\mathbf{x}} = \mathbf{A}\mathbf{x} + \mathbf{B}, \tag{4.9}$$

where $\mathbf{x}$ is the fifth-order state space vector which includes the five state variables mentioned above, the inductor current i_L, both capacitor voltages v_P and v_N and both integral variables σ_P and σ_N, and is defined as

$$\mathbf{x} = [i_L, v_P, v_N, \sigma_P, \sigma_N]^T.$$

The dynamics of the converter will be determined by a (5×5) matrix $\mathbf{A}$ and the 5-dimensional vector $\mathbf{B}$, which depend on the topology and are given by

$$\mathbf{A} = \begin{bmatrix} \dfrac{-r_L}{L} & A_{12} & A_{13} & 0 & 0 \\ A_{21} & \dfrac{-1}{R_P C_P} & 0 & 0 & 0 \\ A_{31} & 0 & \dfrac{-1}{R_N C_N} & 0 & 0 \\ 0 & \dfrac{1}{\tau_P} & 0 & 0 & 0 \\ 0 & 0 & \dfrac{1}{\tau_N} & 0 & 0 \end{bmatrix}, \tag{4.10}$$

$$\mathbf{B} = \begin{bmatrix} B_1 & 0 & 0 & -\dfrac{V_P}{\tau_P} & -\dfrac{V_N}{\tau_N} \end{bmatrix}^T, \tag{4.11}$$

where the elements depending on the four topologies are summarized in Table 4.3.

Considering the definition of the binary signals u_A and u_B defined above, the matrix (4.10) and the vector (4.11) can be simplified and written as follows:

$$\mathbf{A} = \begin{bmatrix} -\dfrac{r_L}{L} & \dfrac{u_B - 1}{L} & \dfrac{1 - u_A}{L} & 0 & 0 \\ \dfrac{1 - u_B}{C_P} & \dfrac{-1}{R_P C_P} & 0 & 0 & 0 \\ \dfrac{u_A - 1}{C_N} & 0 & \dfrac{-1}{R_N C_N} & 0 & 0 \\ 0 & \dfrac{1}{\tau_P} & 0 & 0 & 0 \\ 0 & 0 & \dfrac{1}{\tau_N} & 0 & 0 \end{bmatrix}, \tag{4.12}$$

$$\mathbf{B} = \begin{bmatrix} \dfrac{V_{IN}}{L} u_A & 0 & 0 & -\dfrac{V_P}{\tau_P} & -\dfrac{V_N}{\tau} \end{bmatrix}. \tag{4.13}$$

4.2.2   Averaged model

Under the assumption of small period of the modulating signal compared to the time constants of the circuit, the dynamics of the system (4.9) can be analyzed by means

	ON:ON	ON:OFF	OFF:ON	OFF:OFF
A_{21}	0	$\dfrac{1}{C_P}$	0	$\dfrac{1}{C_P}$
A_{31}	0	0	$-\dfrac{1}{C_N}$	$-\dfrac{1}{C_N}$
A_{12}	0	$-\dfrac{1}{L}$	0	$-\dfrac{1}{L}$
A_{13}	0	0	$\dfrac{1}{L}$	$\dfrac{1}{L}$
B_1	$\dfrac{V_{IN}}{L}$	$\dfrac{V_{IN}}{L}$	0	0

Table 4.3. Matrix elements

of a smooth averaged model, where the switching action is not taken into account and, consequently, the state variables can be considered as constant values during the entire period. A simple model can be derived easily from (4.12) and (4.13), by substituting the binary functions u_A and u_B by the averaged duty cycles, which will be called $\bar{d}_A$ and $\bar{d}_B$ respectively. Now, the domain of these continuous signals turns into $\bar{d}_A$, $\bar{d}_B \in (0,1)$. Therefore, from (4.12), the averaged model will be described as follows

$$\frac{\mathrm{d}\bar{\mathbf{x}}}{\mathrm{d}t} = \begin{bmatrix} -\dfrac{r_L}{L} & \dfrac{\bar{d}_B - 1}{L} & \dfrac{1 - \bar{d}_A}{L} & 0 & 0 \\ \dfrac{1 - \bar{d}_B}{C_P} & \dfrac{-1}{R_P C_P} & 0 & 0 & 0 \\ \dfrac{\bar{d}_A - 1}{C_N} & 0 & \dfrac{-1}{R_N C_N} & 0 & 0 \\ 0 & \dfrac{1}{\tau_P} & 0 & 0 & 0 \\ 0 & 0 & \dfrac{1}{\tau_N} & 0 & 0 \end{bmatrix} \bar{\mathbf{x}} + \begin{bmatrix} \dfrac{V_{IN}\bar{d}_A}{L} \\ 0 \\ 0 \\ \dfrac{-V_P}{\tau_P} \\ \dfrac{-V_N}{\tau_N} \end{bmatrix}, \qquad (4.14)$$

where the bar stands for the averaging during one switching period and hence, $\bar{\mathbf{x}} = [\bar{i}_L, \bar{v}_P, \bar{v}_N, \bar{\sigma}_P, \bar{\sigma}_N]^T$ will correspond to the averaged vector of state variables and $\bar{i}_L$, $\bar{v}_P$, $\bar{v}_N$, $\bar{\sigma}_P$ and $\bar{\sigma}_N$ are the corresponding averaged state variables.

The control proposed previously for this converter gives us explicit expressions of the averaged duty cycles (see Fig. 4.7), which, together with (4.14), determine the closed
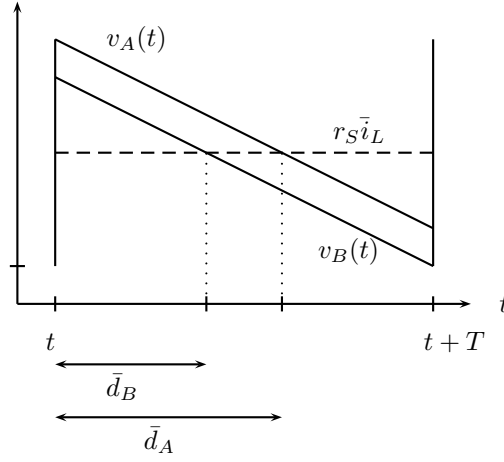
Figure 4.7. The definition of the averaged duty cycles for the mode $\mathcal{M}_P$.

loop of the converter. These expressions are given by

$$\bar{d}_A = \frac{V_U + g_{NA}(\bar{v}_N - V_N + \bar{\sigma}_N) + g_{PA}(V_P - \bar{v}_P - \bar{\sigma}_P) - g_{FA}V_{IN} - r_S\bar{i}_L}{V_U - V_L}, \quad (4.15)$$

$$\bar{d}_B = \frac{V_U + g_{NB}(\bar{v}_N - V_N + \bar{\sigma}_N) + g_{PB}(V_P - \bar{v}_P - \bar{\sigma}_P) - g_{FB}V_{IN} - r_S\bar{i}_L}{V_U - V_L}. \quad (4.16)$$

This averaged approach allows us to determine the equilibrium points of the systems, denoted by $\bar{\mathbf{x}}^*$, which will correspond to limit cycles in the switched model. The value of the equilibrium points can be obtained by solving the set of equations

$$\mathbf{A}\bar{\mathbf{x}}^* + \mathbf{B} = 0, \quad (4.17)$$

which corresponds to the equations

$$
\begin{bmatrix}
-\dfrac{r_L}{L} & \dfrac{\bar{d}_B - 1}{L} & \dfrac{1 - \bar{d}_A}{L} & 0 & 0 \\[2mm]
\dfrac{1 - \bar{d}_B}{C_P} & \dfrac{-1}{R_P C_P} & 0 & 0 & 0 \\[2mm]
\dfrac{\bar{d}_A - 1}{C_N} & 0 & \dfrac{-1}{R_N C_N} & 0 & 0 \\[2mm]
0 & \dfrac{1}{\tau_P} & 0 & 0 & 0 \\[2mm]
0 & 0 & \dfrac{1}{\tau_N} & 0 & 0
\end{bmatrix}
\begin{bmatrix}
\bar{i}_L^* \\[2mm]
\bar{v}_P^* \\[2mm]
\bar{v}_N^* \\[2mm]
\bar{\sigma}_P^* \\[2mm]
\bar{\sigma}_N^*
\end{bmatrix}
+
\begin{bmatrix}
\dfrac{V_{IN}\bar{d}_A}{L} \\[2mm]
0 \\[2mm]
0 \\[2mm]
\dfrac{-V_P}{\tau_P} \\[2mm]
\dfrac{-V_N}{\tau_N}
\end{bmatrix}
=
\begin{bmatrix}
0 \\[2mm]
0 \\[2mm]
0 \\[2mm]
0 \\[2mm]
0
\end{bmatrix}. \quad (4.18)
$$

Firstly, in order to understand the possible solutions of this set of equations, only those belonging to the open loop will be considered. Then, it is easy to prove, from

the second and third equation of (4.18) that the expressions of the duty cycles in the steady state are given by

$$\bar{d}_A = 1 + \frac{\bar{v}_N^*}{R_N \bar{i}_L^*},\tag{4.19}$$

$$\bar{d}_B = 1 - \frac{\bar{v}_P^*}{R_P \bar{i}_L^*}.\tag{4.20}$$

The fourth and fifth equations of (4.18) force the steady state of the capacitor voltages to the corresponding voltage reference, and thus

$$\bar{v}_P^* = V_P,\tag{4.21}$$

$$\bar{v}_N^* = V_N.\tag{4.22}$$

Finally, the expression of the steady state of the averaged inductor current can be obtained from the first equation of (4.18), together with (4.21) and (4.22) solving the equation,

$$-\frac{r_L}{L}\bar{i}_L^* + \frac{\bar{d}_B - 1}{L}V_P + \frac{1 - \bar{d}_A}{L}V_N + \frac{V_{IN}\bar{d}_A}{L} = 0,\tag{4.23}$$

from which the following expression for $\bar{i}_L$ is obtained

$$\bar{i}_L^* = \frac{V_{IN}}{2r_L} \pm \sqrt{\left(\frac{V_{IN}}{2r_L}\right)^2 - \frac{1}{r_L}\left(\frac{V_P^2}{R_P} + \frac{V_N^2}{R_N} - \frac{V_{IN}V_N}{R_N}\right)}.\tag{4.24}$$

This expression corresponds to an ellipsoid in the phase space, with high (positive sign) and low (negative sign) current. Nevertheless, though the expression (4.24) includes the negative and positive values of the square root, only the negative one will be used in a real design of the converter due to the fact the alternative solution will imply high current which means high losses in the series resistor of the inductor. The existence of equilibrium points also requires positive values of the discriminant of the square root in (4.24).

Figure 4.8 shows the transient of the state variables i_L, v_P and v_N by using the averaged model proposed here and the PSIM simulator. Notice that the averaged model predicts accurately the evolution of the inductor current and both capacitor voltages. Nevertheless, the averaged model fails in the prediction of the steady state of the integral variables.

4.2.3   Stability analysis of the equilibrium points

The stability of the equilibrium point of a dynamical system is known to be equivalent to the stability of a linearized system in the neighborhood of an equilibrium point.

(a) i_L (b) v_P and v_N
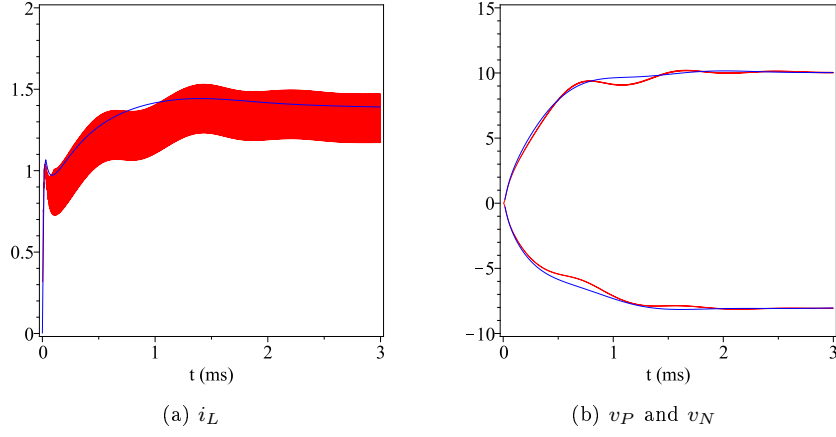
Figure 4.8. Comparison of the evolution of the state variables obtained with the averaged (blue) and switched models (red). The parameters are in Table 4.2.

Therefore, the stability of the proposed converter can be analyzed by means of the properties of the Jacobian matrix evaluated in the equilibrium point $\bar{\mathbf{x}}^*$. Taking into account that the element J_{ij} of this matrix corresponds to the partial derivative of the equation i of (4.14) respect the element j of the state vector evaluated at the equilibrium point, the expression of the Jacobian Matrix is given by

$$
J = \begin{bmatrix}
& & -\dfrac{1}{L}\dfrac{V'_P}{V_D} & \dfrac{1}{L}\dfrac{V'_N}{V_D} \\[2mm]
& J_P & \dfrac{g_{PB}}{V_D}\dfrac{\bar{i}^*_L}{C_P} & -\dfrac{g_{NB}}{V_D}\dfrac{\bar{i}^*_L}{C_P} \\[2mm]
& & -\dfrac{g_{PA}}{V_D}\dfrac{\bar{i}^*_L}{C_N} & \dfrac{g_{NA}}{V_D}\dfrac{\bar{i}^*_L}{C_N} \\[2mm]
0 & \dfrac{1}{\tau_P} & 0 & 0 & 0 \\[2mm]
0 & 0 & \dfrac{1}{\tau_N} & 0 & 0
\end{bmatrix}, \qquad (4.25)
$$

where the submatrix is given by

$$
J_P = \begin{bmatrix}
-\dfrac{r_S}{L}\left(\dfrac{r_L}{r_S}+\dfrac{V'}{V_D}\right) & -\dfrac{1}{L}\left(D'_B+\dfrac{V'_P}{V_D}\right) & \dfrac{1}{L}\left(D'_A+\dfrac{V'_N}{V_D}\right) \\[3mm]
\dfrac{1}{C_P}\left(D'_B+\dfrac{r_S\bar{i}^*_L}{V_D}\right) & \dfrac{1}{C_P}\left(\dfrac{-1}{R_P}+\dfrac{g_{PB}\bar{i}^*_L}{V_D}\right) & -\dfrac{1}{C_P}\dfrac{g_{NB}\bar{i}^*_L}{V_D} \\[3mm]
-\dfrac{1}{C_N}\left(D'_A+\dfrac{r_S\bar{i}^*_L}{V_D}\right) & -\dfrac{1}{C_N}\dfrac{g_{PA}\bar{i}^*_L}{V_D} & \dfrac{1}{C_N}\left(\dfrac{-1}{R_N}+\dfrac{g_{NA}\bar{i}^*_L}{V_D}\right)
\end{bmatrix},
$$

being

$$V'_P = g_{PB}V_P + g_{PA}(V_{IN} - V_N) \qquad \text{and} \qquad V'_N = g_{NB}V_P + g_{NA}(V_{IN} - V_N),$$

$$V' = V_{IN} - V_N + V_P,$$

$$D'_A = 1 - \bar{d}_A \qquad \text{and} \qquad D'_B = 1 - \bar{d}_B,$$

$$V_D = V_U - V_L.$$

Figure 4.9 shows different diagrams, in which the real part of the eigenvalues of the matrix J evaluated in the equilibrium point have been depicted as one single parameter is varied. It is well known that the local stability of a equilibrium point is proved if the real part of all the eigenvalues is negative.

(a) R_P

(b) R_N

(c) V_P

(d) V_N
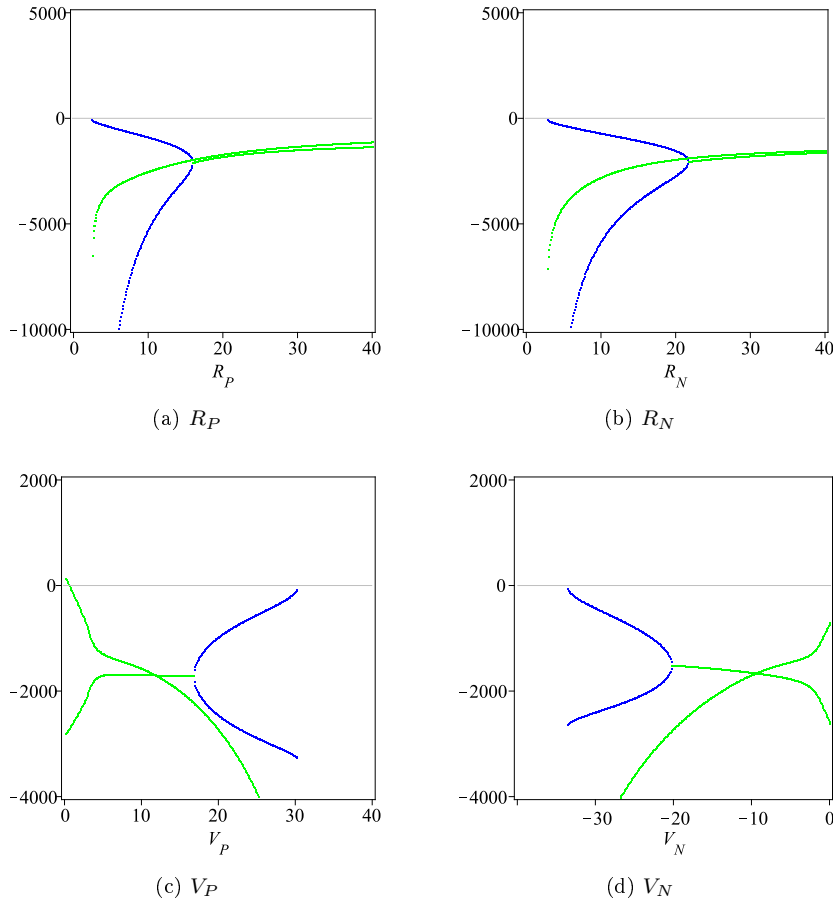
Figure 4.9. Real part of the largest real (blue) and complex (green) eigenvalues of J evaluated in the *low current* equilibrium point as the parameters in the caption is varied. The parameters used are in Table 4.2.

(a) g_{PA}

(b) g_{NA}

(c) g_{PB}

(d) g_{NA} and g_{PB}

(e) τ_P

(f) V_U
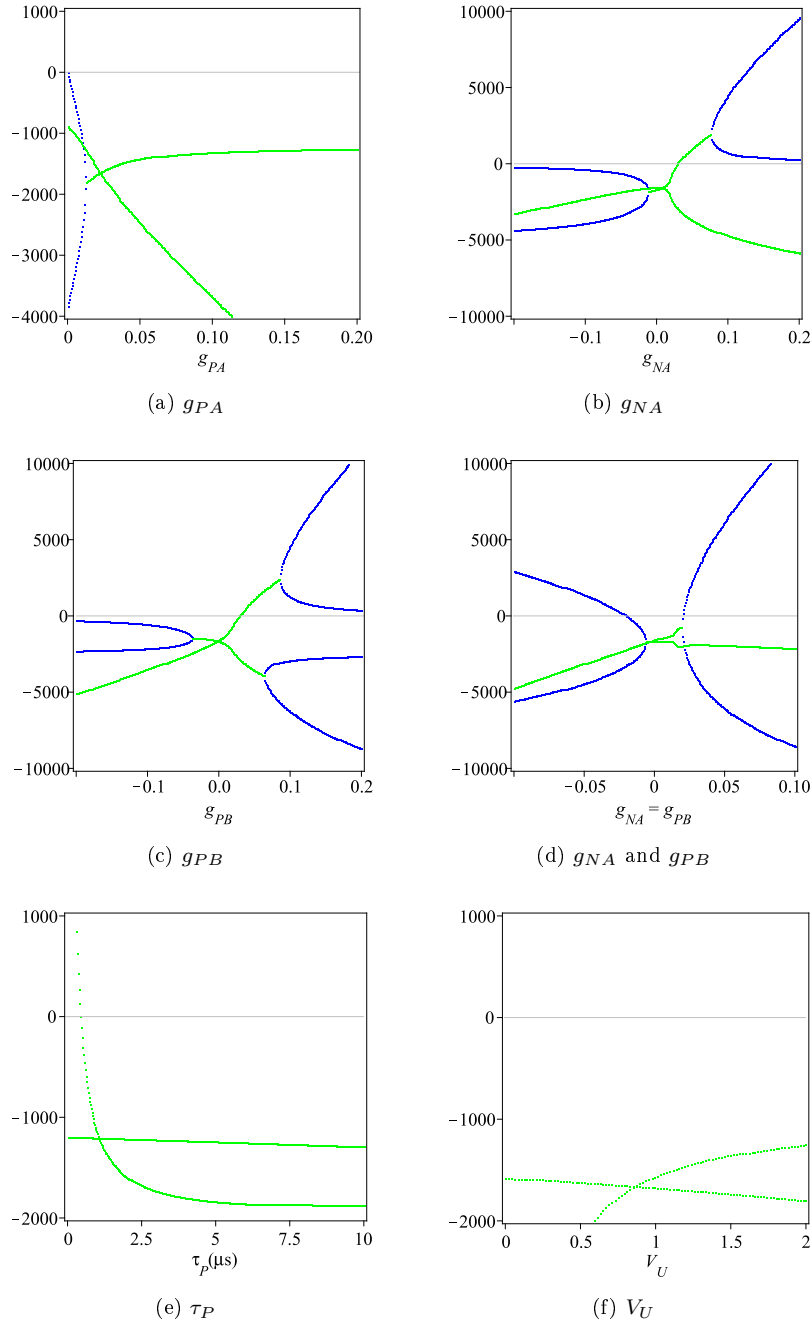
Figure 4.10. Real part of the largest real (blue) and complex (green) eigenvalues of J evaluated in the *low current* equilibrium point as the parameter in the caption is varied. The parameters used are in Table 4.2.

As it can be seen in Fig. 4.9, two kind of smooth bifurcations can be detected by using the averaged model proposed: saddle-node and Hopf bifurcation.

- **Saddle-node bifurcation**:

  Figure 4.9 shows some tangent or saddle-node bifurcations as the parameter, specified in the caption, is varied. It is important to remark that before the appearance of the bifurcation, the two equilibrium points mentioned above, being one stable and the other one, unstable, coexist. Nevertheless, beyond a critical point, these equilibrium points collapse, implying the no existence of any equilibrium point after the bifurcation. Another characteristic of this kind of bifurcation is that the eigenvalues of both equilibrium points tend to zero at this critical point. These phenomena can be seen in the diagrams depicted in Fig. 4.9 taking into account that only the eigenvalues of the stable fixed point have been represented. Figure 4.11 illustrates the steady state of both equilibrium points of the inductor current as V_P is varied showing this smooth bifurcation. It is important to remark that in a real design, the parameters of the converter must be chosen in such a way that the stable equilibrium point is far from this tangent point.
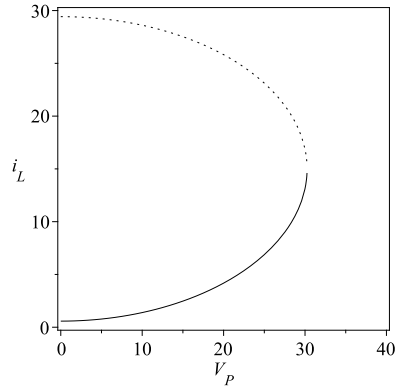
Figure 4.11. Representation of both equilibrium points of the inductor current as the parameter V_P is varied, revealing the existence of a saddle-node bifurcation. Stable and unstable equilibrium points are plotted in solid and dotted line respectively.

Finally, an explicit expression for the critical point can be obtained directly from (4.24), considering that the inductor current cannot be a complex number. This expression is given by

$$\left(\frac{V_{IN}}{2r_L}\right)^2 - \frac{1}{r_L}\left(\frac{V_P^2}{R_P} + \frac{V_N^2}{R_N} - \frac{V_{IN}V_N}{R_N}\right) = 0. \tag{4.26}$$

Therefore, the parameters directly related with this bifurcation are V_{IN}, V_P, V_N, R_P, R_N and r_L.

- **Hopf bifurcation**:

  The Hopf bifurcation, which appears when the real part of the largest complex eigenvalue becomes positive, can be appreciated in Fig. 4.10b,c,e. One property of this bifurcation, due to approaching to zero, is the increment of the transients of the state variables in the neighborhood of the critical point.

  Let us now focus in the influence in the stability when the gains of the feedforward terms are varied. Notice that whereas the variation of the gains g_{PA} (and similarly g_{NB}) are not critical in the stability, the variation of g_{NA} or g_{PB} has a strong influence in the stability of the converter which implies unstable dynamics when the value of the largest eigenvalue differs slightly from 0. Taking into consideration that g_{NA} and g_{PB} are related with the errors of the negative and positive channels, which are driven by the channels S_A and S_B respectively, this result reveals the need of avoiding the direct feedforward terms to guarantee the stability of the converter.

4.3   One-dimensional discrete-time model

Numerical simulations of the dynamics of the converter have revealed the existence of alternative scenarios, apart from those seen in the previous section, related with the ripple of the inductor current. Discrete-time models are known to be useful tools to analyze the fast dynamics in power switching converters. In following sections, we will deal with several discrete-time models, each of which will be able to cover a determined set of scenarios.

Under discrete-time modeling, the dynamics of the SITITO converter can be described by a fifth-dimensional piecewise-smooth map. Nevertheless, considering some assumptions, this map will be simplified to a one-dimensional piecewise-linear map. Let us assume the period of the modulating signal T much lower than the time constants of every operating topology. In this situation, the ripples of both capacitor voltages are small and consequently, these functions can be approached by their mean values, which are forced by the integral control to the voltage references V_P and V_N. This last consideration also implies that the values of the state variables σ_P and σ_N, which measure the integral of the errors $v_P - V_P$ and $v_N - V_N$ respectively, can also be considered as constant values, whose level can be estimated by means of the averaged model (see [52]). Thus, the whole five-dimensional system can be approached by a one-dimensional map, being the inductor current, which will be denoted as i, the only state variable.

This map will be classified as a piecewise continuous map, whose different trams are required to describe each of the modes of operation determined in the previous section. Nevertheless, the assumptions taken into consideration in the approach will permit to simplify the model. Let us consider the condition which distinguishes the operation

modes between $\mathcal{M}_P$ and $\mathcal{M}_N$ (4.8). In concordance with (4.19) and (4.20), (4.8) can be written as follows

$$1 + \frac{\bar{v}_N^*}{R_N \bar{i}_L^*} - \left(1 - \frac{\bar{v}_P^*}{R_P \bar{i}_L^*}\right) = 0. \tag{4.27}$$

From the averaged model, the steady state of the capacitors $\bar{v}_P^*$ and $\bar{v}_N^*$ are known to be V_P and V_N respectively. Therefore, (4.27) can be simplified as follows

$$\frac{V_P}{R_P} + \frac{V_N}{R_N} = 0, \tag{4.28}$$

which does not depend on the state variable of the discrete-time model i. This allows us to divide the one-dimensional model into two submappings. Then, the discrete-time model will be defined as

$$f(i, \phi) = \begin{cases} f_1(i, \phi) & \text{if } H_0(\phi) > 0, \\ f_2(i, \phi) & \text{if } H_0(\phi) < 0, \end{cases}$$

where $f : \mathbb{R}^1 \times \mathbb{R}^9 \mapsto \mathbb{R}^1$ and $i \subset \mathcal{D} \in \mathbb{R}$ refers to the inductor current. ϕ represents the following set of 9 parameters:

$$\phi = \{V_{IN}, r_L, V_P, V_N, R_P, R_N, V_U, V_L, T\}.$$

Finally, the surface $H_0(\phi)$ will be defined as

$$H_0(\phi) = \frac{V_P}{R_P} + \frac{V_N}{R_N}, \tag{4.29}$$

where $H_0 : \mathbb{R}^9 \mapsto \mathbb{R}$. According with this definition, the first submapping f_1 will operate for positive values of (4.29) and thus, whenever $d_A > d_B$, whereas the submapping f_2 will be active when $d_A < d_B$. Note that each of the submappings f_1 and f_2 is itself a PWS map characterized by different operating regions. In what follows, we will treat separately the analysis of the two submappings.

	S_A	S_B	Δi	
$\mathcal{T}_1$	ON	ON	$\Delta \mathtt{i}_1$	$\dfrac{V_{IN} - r_L I_Q}{L}T$
$\mathcal{T}_2$	ON	OFF	$\Delta \mathtt{i}_2$	$\dfrac{V_{IN} - V_P - r_L I_Q}{L}T$
$\mathcal{T}_3$	OFF	ON	$\Delta \mathtt{i}_3$	$\dfrac{V_N - r_L I_Q}{L}T$
$\mathcal{T}_4$	OFF	OFF	$\Delta \mathtt{i}_4$	$\dfrac{V_N - V_P - r_L I_Q}{L}T$

Table 4.4. Definition of the increment currents of the SITITO converter in CCM.
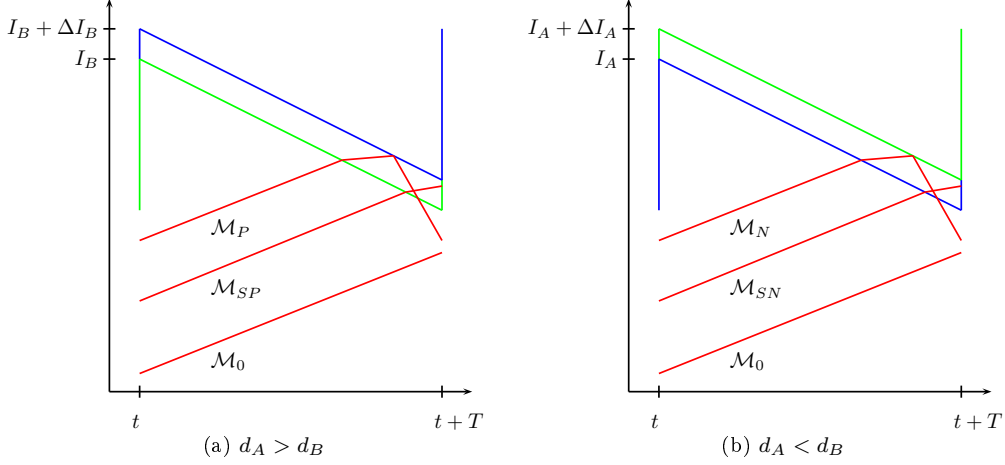
Figure 4.12. The different modes of operation of the SITITO converter. The signals represented correspond to v_A/r_S (blue), v_B/r_S (green) and i_L (red).

4.3.1   Approximated expressions of the maps f_1 and f_2

The definition of the map must approach the evolution of i_L in each topology, during a period of the modulating ramp. These functions can be obtained directly approaching the state equations defined in (4.10) and (4.11) and assuming a linear time dependence of i_L. Therefore, different increment currents, whose expressions are summarized in Table 4.4, will be obtained for each topology. Notice that in the expressions the capacitor voltages have been approached by their corresponding voltage reference and the term $r_L i_L$, which is related with the losses in the inductor resistance, by $r_L I_Q$ where I_Q will correspond to $\bar{i}_L^*$.

Dealing with function f_1, there exist three modes of operation involved (see Fig. 4.12a): $\mathcal{M}_0$, $\mathcal{M}_{SP}$ and $\mathcal{M}_P$, where none, one and two switchings are produced during a period. Consequently, the discrete-time model f_1 will be described by three pieces (see Fig. 4.13), which will be called F_A, F_B and F_C respectively. Thus, the map f_1 will be defined as follows

$$f_1(i, \phi) = \begin{cases} F_A(i, \phi) & \text{if } i \in S_A, \\ F_B(i, \phi) & \text{if } i \in S_B, \\ F_C(i, \phi) & \text{if } i \in S_C, \end{cases} \tag{4.30}$$

where $F_i : \mathbb{R} \times \mathbb{R}^9 \mapsto \mathbb{R}$. The regions of S_A, S_B and S_C represent the domain of each tram.

Conversely, the function f_2 will also be composed by the three trams, G_A, G_B and G_C, which model the modes of operation $\mathcal{M}_0$, $\mathcal{M}_{SN}$ and $\mathcal{M}_N$ respectively (see Fig.

4.12b). Therefore, the map f_2 will be expressed as follows

$$f_2(i, \phi) = \begin{cases} G_A(i, \phi) & \text{if } i \in T_A, \\ G_B(i, \phi) & \text{if } i \in T_B, \\ G_C(i, \phi) & \text{if } i \in T_C. \end{cases} \tag{4.31}$$

According to Fig. 4.12 and Table 4.4, the expressions of the functions F_A, F_B and F_C can be easily obtained and are expressed as

$$F_A(i) = i + \Delta\mathtt{i}_1, \tag{4.32}$$

$$F_B(i) = i + \Delta\mathtt{i}_1 d_B(i) + \Delta\mathtt{i}_2 \left(1 - d_B(i)\right), \tag{4.33}$$

$$F_C(i) = i + \Delta\mathtt{i}_1 d_B(i) + \Delta\mathtt{i}_2 \bar{d}_{AB} + \Delta\mathtt{i}_4 \left(1 - d_B(i) - \bar{d}_{AB}\right), \tag{4.34}$$

where d_B corresponds to

$$d_B(i) = \frac{I_B - i}{\Delta\mathtt{i}_1 - \Delta\mathtt{ir}}, \tag{4.35}$$

being

$$\Delta\mathtt{ir} = -\frac{V_U - V_L}{r_S}.$$

The parameter I_B corresponds to the peak value of the reference v_B at the beginning of the period divided by the sensing resistance ($I_B = v_B(0)/r_S$). The value of $\bar{d}_{AB}$, which represents the difference between both duty cycles, $d_A - d_B$, will be forced in this one-dimensional map to the value predicted by means of the averaged model. Hence, the expression for d_{AB} is give by

$$\bar{d}_{AB} = \frac{1}{I_Q} \left(\frac{V_P}{R_P} + \frac{V_N}{R_N}\right).$$

Once the evolutions of the inductor current has been fixed, let us determine the expressions for the regions S_A, S_B and S_C. Notice that the functions F_A and F_B model the dynamics when none or one switching is produced, which implies $d_B > 1$ and $d_B + d_{AB} > 1$, respectively. Then, these modes of operation will act when the conditions (see Fig. 4.12)

$$i < I_B - (\Delta\mathtt{i}_1 - \Delta\mathtt{ir}),$$

$$i > I_B - (\Delta\mathtt{i}_1 - \Delta\mathtt{ir}) \quad \text{and} \quad i < I_B - (1 - \bar{d}_{AB})(\Delta\mathtt{i}_1 - \Delta\mathtt{ir}),$$

respectively, are fulfilled. Therefore, the regions can be established by the expressions

$$S_A = \left\{i \in \mathcal{D} : H_{F,AB}(i, \phi) < 0\right\},$$

$$S_B = \left\{i \in \mathcal{D} : H_{F,AB}(i, \phi) > 0 \quad \text{and} \quad H_{F,BC}(i, \phi) < 0\right\},$$

$$S_C = \left\{i \in \mathcal{D} : H_{F,BC}(i, \phi) > 0\right\},$$
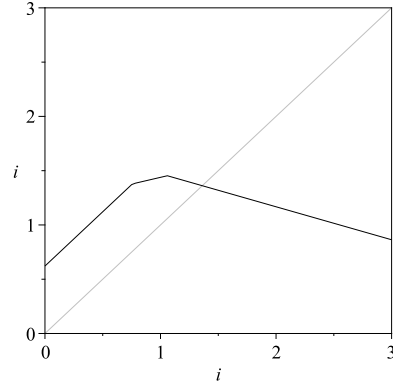
Figure 4.13. Illustration of the three-piece map f_1 and the fixed point i^*. The parameters used are in Table 4.4.

being

$$H_{F,AB}(i) = i - I_B + \Delta i_1 - \Delta ir,$$

$$H_{F,BC}(i) = H_{F,AB}(i) - \overline{d}_{AB}(\Delta i_1 - \Delta ir).$$

Similarly, expressions for the map f_2 can be found and are given by

$$G_A(x) = i + \Delta i_1, \tag{4.36}$$

$$G_B(x) = i + \Delta i_1 d_A(i) + \Delta i_3 \left(1 - d_A(x)\right), \tag{4.37}$$

$$G_C(x) = i + \Delta i_1 d_A(i) - \Delta i_3 \overline{d}_{AB} + \Delta i_4 \left(1 - d_A(i) + \overline{d}_{AB}\right), \tag{4.38}$$

where d_A corresponds to

$$d_A(i) = \frac{I_A - i}{\Delta i_1 - \Delta ir}. \tag{4.39}$$

The parameter I_A corresponds to $I_A = v_A/r_S$ at the beginning of the period. Finally, the existence regions will be given by

$$T_A = \left\{i \in \mathcal{D} : H_{G,AB}(i, \phi) < 0\right\},$$

$$T_B = \left\{i \in \mathcal{D} : H_{G,AB}(i, \phi) > 0 \quad \text{and} \quad H_{G,BC}(i, \phi) < 0\right\},$$

$$T_C = \left\{i \in \mathcal{D} : H_{G,BC}(i, \phi) > 0\right\},$$

being

$$H_{G,AB}(i) = i - I_A + \Delta i_1 - \Delta ir,$$

$$H_{G,BC}(i) = H_{G,AB}(i) + \overline{d}_{AB}(\Delta i_1 - \Delta ir).$$

Obtaining approached expressions of I_B and I_A

Notice that the values of parameters I_B and I_A are still undefined. These values will establish the level of the voltage references and consequently, the averaged value of the variable i. Before obtaining their appropriate expressions, let us consider the influence of these parameters in the value of the steady state, assuming the main modes $\mathcal{M}_P$ and $\mathcal{M}_N$. Let us define i_F^* and i_G^* as the fixed points of the functions F_C and G_C respectively and let us assume that the duty cycle in this equilibrium situation corresponds to the averaged $\bar{d}_B$ and $\bar{d}_A$. Then, $F_C(i_F^*)$ and $G_C(i_G^*)$ will be

$$F_C(i_F^*) = i_F^* + \Delta\mathtt{i}_1\bar{d}_B + \Delta\mathtt{i}_2\bar{d}_{AB} + \Delta\mathtt{i}_4\left(1 - \bar{d}_B - \bar{d}_{AB}\right) \tag{4.40}$$

and

$$G_C(i_G^*) = i_G^* + \Delta\mathtt{i}_1\bar{d}_A - \Delta\mathtt{i}_3\bar{d}_{AB} + \Delta\mathtt{i}_4\left(1 - \bar{d}_A + \bar{d}_{AB}\right). \tag{4.41}$$

If i_F^* and i_G^* are fixed points of $F_C(i)$, $G_C(i)$ then following conditions must be fulfilled

$$\Delta\mathtt{i}_1\bar{d}_B + \Delta\mathtt{i}_2\bar{d}_{AB} + \Delta\mathtt{i}_4\left(1 - \bar{d}_B - \bar{d}_{AB}\right) = 0$$

and

$$\Delta\mathtt{i}_1\bar{d}_A - \Delta\mathtt{i}_3\bar{d}_{AB} + \Delta\mathtt{i}_4\left(1 - \bar{d}_A + \bar{d}_{AB}\right) = 0.$$

Replacing the current increments with the expressions given in Table 4.4, the following expression is obtained in both cases:

$$-\frac{r_L}{L}I_Q + \frac{\bar{d}_B - 1}{L}V_P + \frac{1 - \bar{d}_A}{L}V_N + \frac{V_{IN}\bar{d}_A}{L} = 0, \tag{4.42}$$

which corresponds to the condition obtained in the averaged approach (4.23). Therefore, (4.42) is fulfilled and consequently, i_F^* and i_G^* are fixed points of the F_C and G_C respectively, whose expressions can be obtained forcing the duty cycles to their averaged values. Then, from (4.19), (4.20), (4.35) and (4.39) we obtain

$$d_B^* = \frac{I_B - i_F^*}{\Delta\mathtt{i}_1 - \Delta\mathtt{i}\mathtt{r}} = 1 - \frac{V_P}{R_P I_Q},$$

and

$$d_A^* = \frac{I_A - i_G^*}{\Delta\mathtt{i}_1 - \Delta\mathtt{i}\mathtt{r}} = 1 + \frac{V_N}{R_N I_Q},$$

and thus,

$$i_F^* = I_B - \left(1 - \frac{V_P}{R_P I_Q}\right)(\Delta\mathtt{i}_1 - \Delta\mathtt{i}\mathtt{r})$$

and

$$i_G^* = I_A - \left(1 + \frac{V_N}{R_N I_Q}\right)(\Delta\mathtt{i}_1 - \Delta\mathtt{i}\mathtt{r}).$$

Consequently, the value of the fixed points will be determined by I_B and I_A. The strategy proposed here to establish the value of I_B and I_A is to force the mean value during a period of $i_L(t)$ to be equal to I_Q, assuming there exists a situation of equilibrium, then

$$\frac{1}{T} \int_t^{t+T} i_L(t)dt = I_Q. \tag{4.43}$$

To solve this equation, assuming that the evolution of the inductor current is linear in each topology and the duty cycles of the steady state are those predicted in the averaged model. Then,

$$i_F^* + \frac{1}{2T} \left(\Delta i_1 \bar{d}_B^2 + \Delta i_2 \bar{d}_{AB}^2 + 2\Delta i_1 \bar{d}_B \bar{d}_{AB} - \Delta i_4 (1 - \bar{d}_A)^2 \right) = I_Q$$

and

$$i_G^* + \frac{1}{2T} \left(\Delta i_1 \bar{d}_A^2 + \Delta i_3 \bar{d}_{AB}^2 - 2\Delta i_1 \bar{d}_A \bar{d}_{AB} - \Delta i_4 (1 - \bar{d}_B)^2 \right) = I_Q$$

and thus,

$$i_F^* = I_Q - \frac{1}{2T} \left(\Delta i_1 \bar{d}_B^2 + \Delta i_2 \bar{d}_{AB}^2 + 2\Delta i_1 \bar{d}_B \bar{d}_{AB} - \Delta i_4 (1 - \bar{d}_A)^2 \right)$$

and

$$i_G^* = I_Q - \frac{1}{2T} \left(\Delta i_1 \bar{d}_A^2 + \Delta i_3 \bar{d}_{AB}^2 - 2\Delta i_1 \bar{d}_A \bar{d}_{AB} - \Delta i_4 (1 - \bar{d}_B)^2 \right).$$

Finally, the expressions of I_B and I_A will be given by

$$I_B = i_F^* + \bar{d}_B \left(\Delta i_1 - \Delta ir \right)$$

and

$$I_A = i_G^* + \bar{d}_A \left(\Delta i_1 - \Delta ir \right).$$

It can be proved that both expressions for i_F^* and i_G^* are, in fact, equivalent and it is important to remark here their dependence on parameters T and V_D.

4.3.2   Fixed points of f_1 and f_2

Though the maps f_1 and f_2 could have several fixed points, only the fixed points belonging to the functions F_C or G_C, which have been found previously, will be taken into consideration in our analysis. Notice that only the modes of operation $\mathcal{M}_P$ and $\mathcal{M}_N$ imply the switching of S_A and S_B during the same period. If only one switch is given, the one-dimensional map would predict a stable dynamics, but the real system cannot be stable except in the particular cases $V_P = 0$ and $V_N = 0$. i_F^* or i_G^*, whose expressions are equivalent, will be referred here as the main fixed point (i^*).

(a) $V_U = 2.0\,\mathrm{V}$ (b) $V_U = 1.2\,\mathrm{V}$
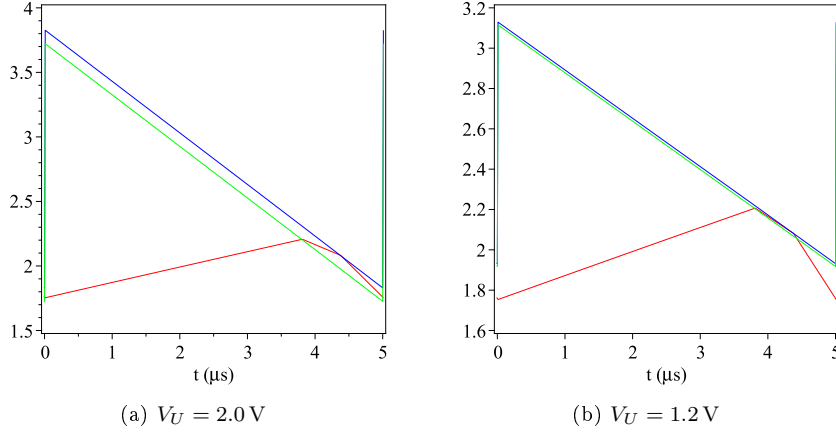
Figure 4.14. Temporal evolution of the signals v_A (blue), v_B (green) and $r_S i_L$ (red).

4.3.3   Stability analysis of the main fixed point

The stability of the main fixed point can be analyzed by means of the derivative of the functions F_C and G_C. Therefore, from (4.34) and (4.35) or from (4.38) and (4.39), the derivative of both functions will be determined by the expression

$$\lambda = \frac{\Delta \mathtt{i}_4 - \Delta \mathtt{ir}}{\Delta \mathtt{i}_1 - \Delta \mathtt{ir}}, \tag{4.44}$$

which does only depend on the current increments of the first and third stage. Moreover, due to $\Delta \mathtt{i}_1 > 0$ and $\Delta \mathtt{i}_4 < 0$, $\lambda < 1$ the stability of the main fixed point will be guaranteed provided that $\lambda > -1$. Therefore, the instability occurs when the following condition is fulfilled:

$$V_{IN} + V_N - V_P - 2r_L I_Q + 2(V_U - V_L)\frac{L}{r_S T} = 0. \tag{4.45}$$

4.3.4   Existence of the main fixed point

Let us now deal with the existence of the main fixed point. From (4.30) and (4.31), the condition of existence for fixed points are given by

$$i^* \in S_C \qquad \text{or} \qquad i^* \in T_C,$$

whether the mode of operation is $\mathcal{M}_P$ or $\mathcal{M}_N$ respectively. Therefore, the fixed point will be admissible if the conditions

$$H_{F,BC}(i^*) >= 0 \quad \text{or} \quad H_{G,BC}(i^*) >= 0$$

is fulfilled. Considering that these conditions are equivalent to $\bar{d}_A < 1$ or $\bar{d}_B < 1$ in the mode $\mathcal{M}_P$ or $\mathcal{M}_N$ respectively, from (4.19) and (4.20), the existence of the fixed

point will be guaranteed if

$$1 + \frac{V_N}{R_N I_Q} < 1 \quad \text{or} \quad 1 - \frac{V_P}{R_P I_Q} < 1,$$

which, taking into account that the resistances and the inductor current are positive and the reference voltages V_P and V_N are defined positive and negative respectively, is always fulfilled. Therefore, the fixed point i^* will never become virtual.

Nevertheless, there exists another boundary due to the definition of the map. In Fig. 4.14, two diagrams have been depicted in which the evolution of both voltage references and the sensed current are represented. Notice that, as the parameters V_U is varied, the inductor current decreases faster than the signal references in the intermediate tram. At the critical point, the three slopes will be equivalent and the second switching is skipped. Actually, the maps (4.30) and (4.31) are only defined if the parameter ΔI_B or ΔI_A (see Fig. 4.12) is positive and so, ΔI_B and ΔI_A becomes 0 at the critical point. Therefore, the following two surfaces can be defined as

$$H_F(\phi) = \Delta I_B = \bar{d}_{AB}(\Delta \mathsf{i}_2 - \Delta \mathsf{ir})$$

or

$$H_G(\phi) = \Delta I_A = -\bar{d}_{AB}(\Delta \mathsf{i}_3 - \Delta \mathsf{ir}),$$

and their corresponding boundaries

$$\Sigma_F(\phi) = \{H_F(\phi) = 0\} \tag{4.46}$$

or

$$\Sigma_G(\phi) = \{H_G(\phi) = 0\}. \tag{4.47}$$

Consequently, a non-smooth bifurcation will occur when the fixed point of the modes of operation $\mathcal{M}_P$ and $\mathcal{M}_N$ crosses the corresponding boundary (4.46) or (4.47). It is important to remark that, despite having the same fixed point and stability condition, the existence condition of the fixed point is different. This fact has some consequences, which will be seen in the following section.

4.3.5   Two-dimensional bifurcation diagrams. Codimension-two points

In this section, several representative two-dimensional bifurcation diagrams will illustrate some of the feasible scenarios that can be predicted with the one-dimensional discrete model presented above. Only one smooth bifurcation will take place, the flip bifurcation, whereas there exist three different conditions in which the fixed point can yield a non-smooth bifurcation:

- **Intermediate slope limit (ISL)**: As it has been mentioned above, a non-smooth bifurcation is yielded when i_F^* or i_G^* crosses the boundaries Σ_F (4.46) or Σ_G (4.47) respectively.

- **Change of the mode of operation (MOC)**: This non-smooth bifurcation will appear when, under the variation of some parameters of the systems, the mode of operation changes from $\mathcal{M}_P$ to $\mathcal{M}_N$ or viceversa. From (4.29), the bifurcation will be given when the corresponding fixed point crosses the boundary defined by:

$$\Sigma_0(\phi) = \{H_0(\phi) = 0\}. \tag{4.48}$$

- **Discontinuous conduction mode (DCM)**: This bifurcation is given when the inductor current drops to 0 at the beginning of the cycle, and thus, the bifurcation occurs when

$$i^* = 0.$$

Flip bifurcation - ISL bifurcation

(a) $R_P = 22\,\Omega$, $R_N = 33\,\Omega$ (b) $R_P = 33\,\Omega$, $R_N = 22\,\Omega$
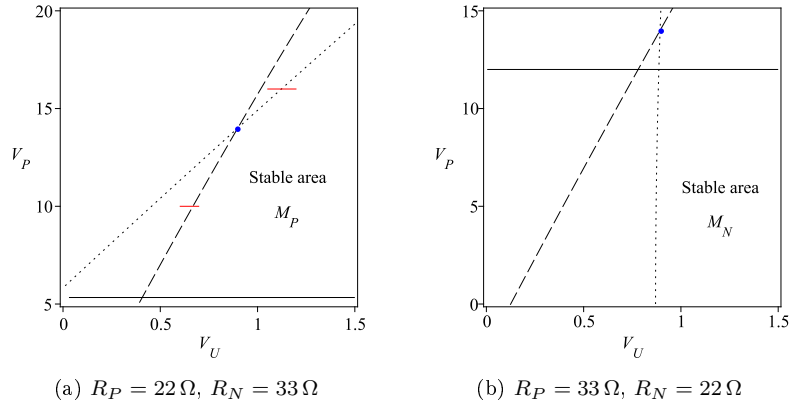
Figure 4.15. Stability (dashed) and ISL (dotted) bifurcation curves in the parameter space $\{V_U, V_P\}$. The solid line represents to the condition Σ_0 (MOC). The parameters are in table 4.2.

In Fig. 4.15, the stability condition (4.44) (dashed lines) and the two border-collision bifurcation curves Σ_F and Σ_G (dotted lines) have been depicted in the two-parameter space $\{V_U, V_P\}$ for the modes of operation $\mathcal{M}_P$ (see Fig. 4.15a) and $\mathcal{M}_N$ (see Fig. 4.15b) respectively. The solid line stands for the condition (4.48), which establishes the change of mode of operation. Therefore, the non-smooth bifurcation curves Σ_F and Σ_G are only valid in their corresponding mode of operation. Let us focus in the first diagram. As V_U is decreased, the fixed point can reach the instability by crossing the flip bifurcation curve or can become virtual by crossing Σ_F. The existence of both scenarios in Fig. 4.15a has been validated, in which two bifurcation diagrams obtained with the PSIM simulator have been depicted (flip bifurcation in Fig. 4.16a and ISL

(a) Flip bifurcation ($V_P = 10.0$ V)   (b) ISL bifurcation ($V_P = 16.0$ V)
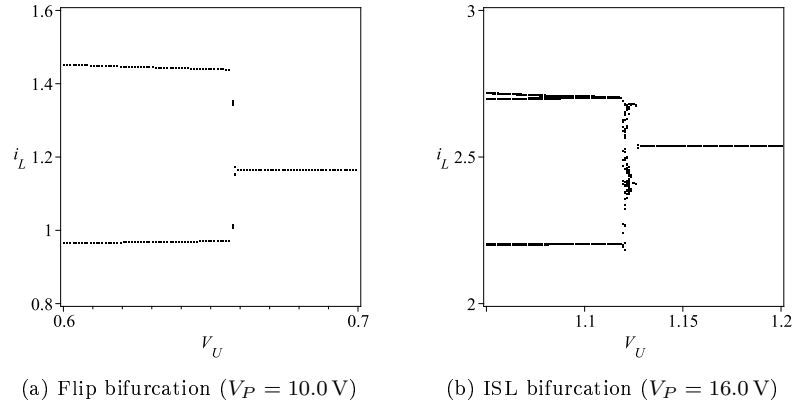
Figure 4.16. Bifurcation diagrams obtained with the PSIM simulator using V_U as varying parameter along segments in Fig. 4.15a.

bifurcation in Fig. 4.16b). Notice that the red lines in Fig. 4.15a correspond to the parameter variation of the one-dimensional bifurcation.

A codimension-two point appears when these two bifurcation curves intersect. From (4.44) and (4.46) or from (4.44) and (4.47), it is obtained the condition

$$V_{IN} - V_N - V_P = 0, \tag{4.49}$$

and from (4.49) and (4.45),

$$(V_U - V_L)\frac{L}{r_S T} + V_N - r_L I_Q = 0. \tag{4.50}$$

The codimension-two point will occur when the conditions (4.49) and (4.50) are fulfilled, for both operation modes. Consequently, for a given set of parameters, this point will appear only in one mode of operation. Notice that in Fig. 4.15b, the fixed point can only present the non-smooth bifurcation due to the fact that the critical point is placed in the $\mathcal{M}_P$ zone.

MOC non-smooth bifurcation curve

Under the variation of some parameters of the system, the fixed point can change the mode of operation between $\mathcal{M}_P$ and $\mathcal{M}_N$. The stability condition has been proved not to be influenced by the mode of operation, in contrast to its corresponding existence condition. This phenomenon has been illustrated in Fig. 4.17, where the involved bifurcation curves have been depicted. In this diagram, the green line represents the stability condition, whereas the solid black line corresponds to the boundary Σ_0. Notice that, in both sides of this curve, there exists a region in which the fixed point is admissible and stable, despite belonging to different modes of operation. Therefore,
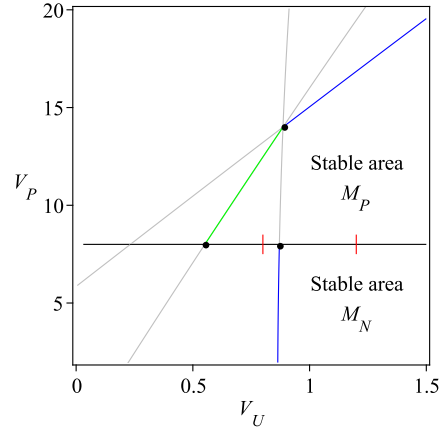
Figure 4.17. Stability (green) and existence (blue) bifurcation curves in the parameter space $\{V_U, V_P\}$. The solid line corresponds to Σ_0 and grey lines represent virtual lines. The parameters are in table 4.2 except: $R_P = R_N = 33\,\Omega$.

a stable fixed point placed in whatever mode can become virtual or persist when changing the mode of operation, but not become unstable. The conditions Σ_F and Σ_G have also been included. Notice that these lines are only defined in the region in which the corresponding fixed point is admissible (blue lines).

Two different bifurcation scenarios have been chosen and denoted with red lines in Fig. 4.17. In one case, for $V_U = 1.2\,\text{V}$, the fixed point persists after crossing the boundary Σ_0. Due to the fact that it cannot be appreciated a significant change in the fixed point in both sides of the bifurcation, two temporal diagrams have been illustrated in Fig. 4.18 to show the persistence scenario. Conversely, the second non-smooth phenomenon can be observed in Fig. 4.19, in which a one-dimensional bifurcation diagram has been shown. For $V_U = 0.8\,\text{V}$, as V_P is decreased, the fixed point of $\mathcal{M}_P$ crosses the boundary Σ_0 by becoming virtual. Moreover, after the boundary, the fixed point i_G^* is also virtual and the dynamics of the converter jumps to a chaotic attractor. This non-smooth phenomenon is characteristic of discontinuous maps.

Discontinuous conduction mode.

The last non-smooth bifurcation that can be predicted by the one-dimensional map occurs when the inductor current drops to zero and operates in DCM. Figure 4.20a shows the DCM bifurcation curve (cyan line) in the parameter space $\{V_U, V_P\}$ when the fixed point belongs to $\mathcal{M}_N$. As it can be seen in the one-dimensional bifurcation diagram included (see 4.20b).

The one-dimensional discrete-time model has been proved to be useful to predict the mentioned non-smooth bifurcation together with the smooth flip bifurcation. Their

(a) $V_P = 8.5\,\text{V}$

(b) $V_P = 7.5\,\text{V}$
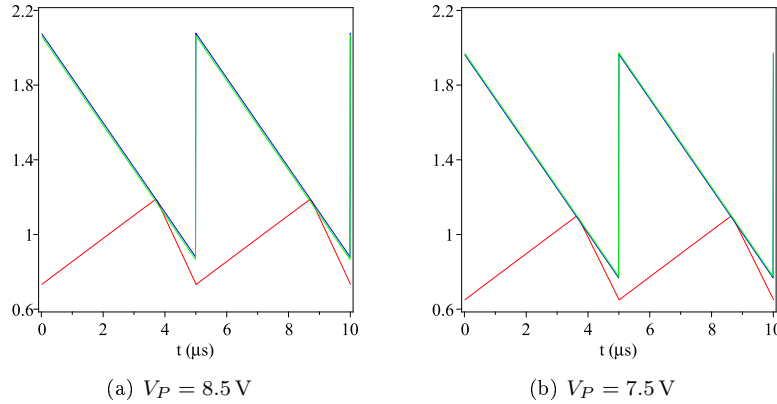
Figure 4.18. Temporal evolution of $r_S i_L$ (red), v_A (blue) and v_B (green) fixing $V_U = 1.2\,\text{V}$ obtained with the PSIM simulator. The parameters are in Fig. 4.17.
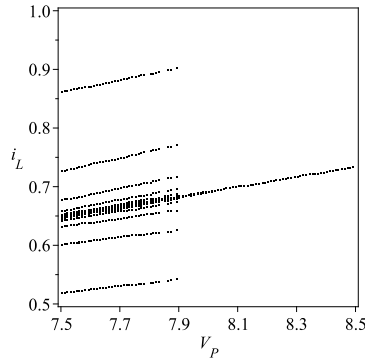
Figure 4.19. Bifurcation diagram using V_P as varying parameter obtained with the PSIM simulator. The parameters are in Fig. 4.17 except: $V_U = 0.8\,\text{V}$.

prediction has resulted to be accurate enough in a range of parameters. Nevertheless, the averaged model predicts a Hopf smooth bifurcation that cannot be predicted by this simplified map due to its unique state variable. This fact has motivated us to develop a more complete map.

4.4   Normalized one-dimensional map

In Chapter 3, the different scenarios that can be given in a three-piece piecewise-lineal map in a restricted range of parameters have been classified in sixteen zones in the parameter space $\{\beta, \gamma\}$. Under the assumption of $\alpha = 1$, the dynamics was reduced to few zones illustrated in Fig. 3.13. Let us now determine which scenarios can occur in the submappings f_1 and f_2 defined above, taking into account the restrictions of the physical parameters.

(a)   (b) $V_U = 0.8\,\text{V}$
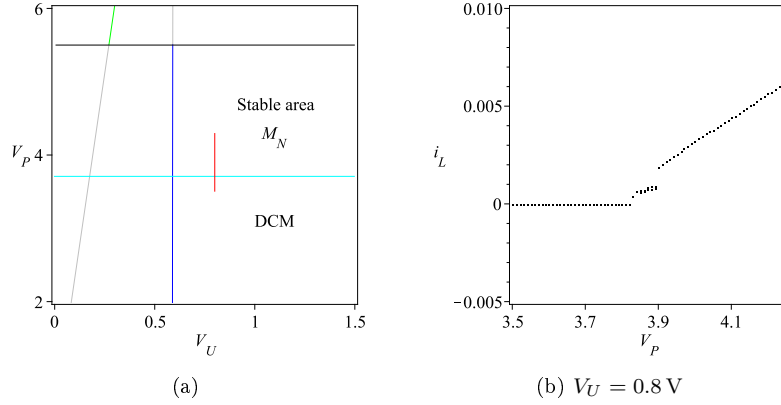
Figure 4.20. (a) Stability (green), Σ_G (blue), Σ_0 (black) and DCM (cyan) bifurcation curves in the parameter space $\{V_U, V_P\}$. (b) Bifurcation diagram obtained with the PSIM simulator according to the red line variation. The parameters are in table 4.2 except: $R_P = R_N = 68\,\Omega$ and $V_N = -5.5\,\text{V}$.

Concerning the submapping f_1, after applying the change of coordinates $x = i - I_B + \Delta\mathtt{i}_1 - \Delta\mathtt{ir}$, this submapping can be rewritten as

$$F_A(x) = x + \Delta\mathtt{i}_1,$$
$$F_B(x) = \left(1 - \frac{\Delta\mathtt{i}_1 - \Delta\mathtt{i}_2}{\Delta\mathtt{i}_1 - \Delta\mathtt{ir}}\right) x + \Delta\mathtt{i}_1,$$
$$F_C(x) = \left(1 - \frac{\Delta\mathtt{i}_1 - \Delta\mathtt{i}_2}{\Delta\mathtt{i}_1 - \Delta\mathtt{ir}} - \frac{\Delta\mathtt{i}_1 - \Delta\mathtt{i}_3}{\Delta\mathtt{i}_1 - \Delta\mathtt{ir}}\right) x + \Delta\mathtt{i}_1 + \bar{d}_{AB}(\Delta\mathtt{i}_1 - \Delta\mathtt{i}_3).$$

Therefore, if the following definitions are taken into consideration

$$\alpha = 1, \quad \beta = -\frac{\Delta\mathtt{i}_1 - \Delta\mathtt{i}_2}{\Delta\mathtt{i}_1 - \Delta\mathtt{ir}}, \quad \gamma = -\frac{\Delta\mathtt{i}_1 - \Delta\mathtt{i}_3}{\Delta\mathtt{i}_1 - \Delta\mathtt{ir}},$$

$$\mu = \Delta\mathtt{i}_1 \quad \text{and} \quad \tau = \bar{d}_{AB}(\Delta\mathtt{i}_1 - \Delta\mathtt{ir}),$$

the three-piece PWL map studied in the previous Chapter is obtained.

Considering the range of the physical parameters, the domain of the normalized parameters are given by

$$\beta < 0 \quad \text{and} \quad \gamma < 0,$$
$$\tau > 0 \quad \text{and} \quad \mu > 0.$$

Notice that $\gamma < 0$ and hence, the only feasible scenarios are placed in zones 1, 3, 4 and 6. Nevertheless, considering the discontinuous boundary Σ_F, which is now determined by the expression

$$\Sigma_F = \{1 + \beta = 0\},$$

$\beta > -1$ and the dynamics of the submapping f_1 is restricted to the zones 1, 3 and 4. Consequently, only the stable period-two solution BC can be found in the system and no coexistence between period-one and two orbits are permitted. These results are in agreement with those obtained in this chapter.

Equivalent results are obtained for the map f_2 and hence, they will not be reproduced here.

4.5   Five-dimensional discrete-time models

The map presented in this section will consider the evolution of all the state variables of the system. Though in the new map the evolution of the inductor current will be also considered linear in each topology, its influence in the evolution of the capacitor voltages will imply the need of nonlinear terms in order to approach their evolution, as well as the evolution of the integral terms. Therefore, the resulting map will be classified as 5-dimensional piecewise-smooth map. Taking all these consideration into account, the following map can be defined:

$$\mathbf{x}_{n+1} = f(\mathbf{x}_n) \tag{4.51}$$

where $\mathbf{x}_n = [i, vp, vn, \sigma p, \sigma n]^T$. Similarly to the definition of the one-dimensional map, (4.51) can be divided into the submappings:

$$f(i, vp, vn, \sigma p, \sigma n, \phi) = \begin{cases} f_1(i, vp, vn, \sigma p, \sigma n, \phi) & \text{if } H_0(vp, vn, \phi) > 0, \\ f_2(i, vp, vn, \sigma p, \sigma n, \phi) & \text{if } H_0(vp, vn, \phi) < 0, \end{cases}$$

where $f : \mathbb{R}^5 \times \mathbb{R}^{19} \mapsto \mathbb{R}^5$ and ϕ refers to the set of parameters

$$\phi = \{V_{IN}, r_L, L, V_P, V_N, R_P, R_N, V_U, V_L, T, C_P, C_N, r_S, g_{PA}, g_{PB}, g_{NA}, g_{NB}, \tau_P, \tau_N\}.$$

The expressions of the map will not be reproduced here, for the sake in brevity. For further details, the complete development of these expression can be found in the Appendix A. Notice that the condition that divides the map (4.51) depends on the state variables vp and vn. Therefore, hybrid solutions belonging to both submappings can now be modelled by this higher dimension map.

4.5.1   Stability bifurcation curves

It has been proved in the one-dimensional analysis that the dynamics of the converter can undergo a flip bifurcation, whose analytical expression has been presented above. Conversely, the averaged model has also detected the existence of a Hopf bifurcation, which corresponds to a Neimark-Sacker case in the discrete-time model, when the parameters related to feedback terms, such as g_{PA}, g_{NB}, τ_P or τ_N, are varied. Let us now analyze the footprints of these bifurcations in the five-dimensional map.

(a)   (b)
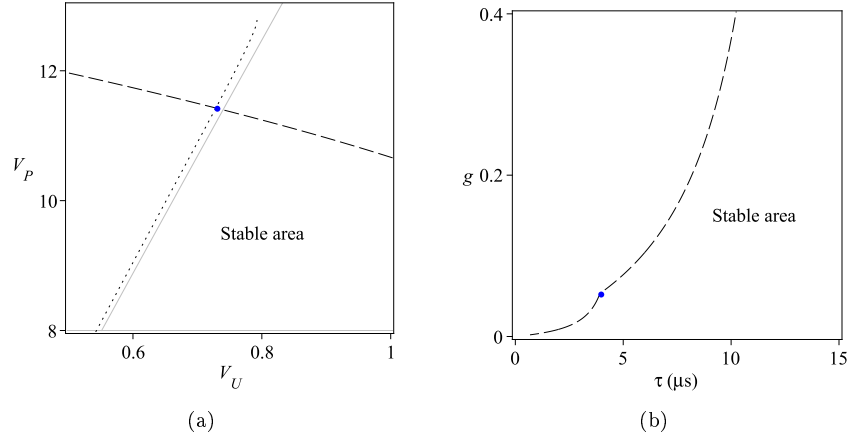
Figure 4.21. Flip bifurcation curve obtained with the 1-D map (solid line) and (4.51) (dotted line) and Neimark-Sacker (dashed line) bifurcation curves obtained with (4.51) in the parameter space $\{V_U, V_P\}$ (a) and $\{\tau, g\}$ (b). The parameters are in table 4.2 except: $R_P = R_N = 33\,\Omega$, $\tau_P = \tau_N = 6\,\mu s$ and $g_{PA} = g_{NB} = 0.1$.

The two-dimensional bifurcation diagrams depicted in Fig. 4.21 shows the smooth bifurcations curves predicted with the maps proposed in this chapter. Solid grey line stands for the flip bifurcation predicted with the one-dimensional maps whereas the dashed and dotted lines correspond to the Neimark-Sacker and flip bifurcations obtained with (4.51). In Fig. 4.21a, the parameter space and the set of selected parameters corresponds to the Fig. 4.17 but fixing $g_{PA} = g_{NB} = 0.1$ and $\tau_P = \tau_N = 6\,\mu s$. Notice the appearance of a Neimark-Sacker bifurcation, reducing significantly the region in which the fixed point is stable. The blue dot in Figure 4.21b illustrates this bifurcation curve in the parameter space $\{g, \tau\}$, being $g = g_{PA} = g_{NB}$ and $\tau = \tau_P = \tau_N$. Roughly, it can be seen the presence of unstable dynamics for lower values of the time constants τ jointly higher values of the gains g. In this case, the blue dot denotes a codimension-two point given by the crossing of two Neimark-Sacker bifurcations.

4.5.2   Non-smooth bifurcations

Let us now recall the non-smooth bifurcations predicted with the one-dimensional discrete-time model. In order to show the feasible deviations between both discrete-time models, the curves illustrated in the mode of operation $\mathcal{M}_P$ in Fig. 4.17 have been depicted in Fig. 4.22a, including now the curves predicted by the 5-dimensional map. Dealing with the MOC bifurcation, none discrepancy has been found between both maps. Actually, both curves cannot be distinguished. The analysis of the DCM bifurcation leads to similar conclusions.

(a)   (b)
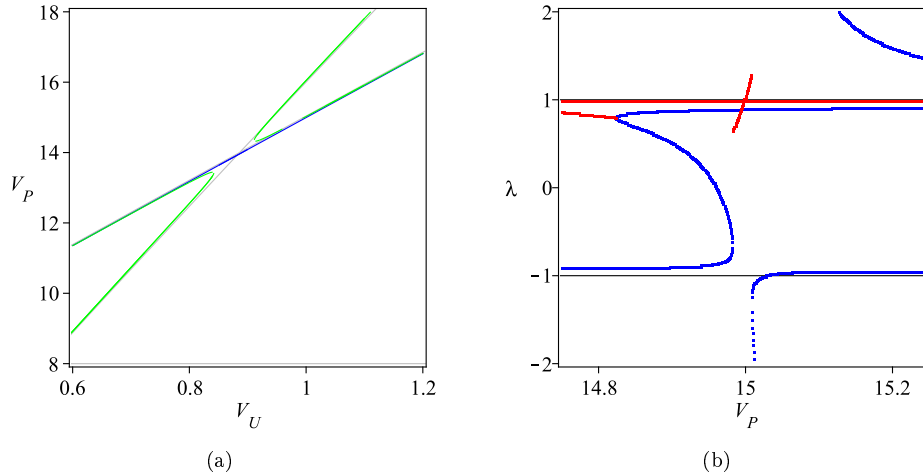
Figure 4.22. (a) Flip (green) and Neimark-Sacker (blue) bifurcation curves obtained with (4.51) in the parameter space $\{V_U, V_P\}$. Grey lines correspond to the bifurcation curves obtained with the one-dimensional map. (b) Modulo of the real (blue) and complex (red) eigenvalues of the Jacobian. The parameters are in table 4.2 except: $R_P = R_N = 33\,\Omega$ and (b) $V_U = 1.0\,\mathrm{V}$.

Nevertheless, an important deviation takes place in the neighborhood of the bifurcation. As it can be noticed in the diagram, in both sides of the ISL bifurcation, two smooth bifurcation curves appear. Notice in the diagram the appearance of the flip and Neimark-Sacker bifurcations. A deeper analysis of the eigenvalues has revealed that the ISL boundary presents a discontinuity in the eigenvalues of the Jacobian matrix (see Fig. 4.22b) despite the continuity of the fixed point. This phenomenon provokes the smooth bifurcations which takes place in the neighborhood of the ISL boundary. Further analysis is required to determine whether this discontinuity is yielded by the nature of the discrete-time model or by the own dynamics of the converter.

4.6   Conclusions

A Single-Inductor Two-Input Two-Output (SITITO) switching dc-dc converter has been analyzed in this chapter. This converter, which does not need symmetry in its positive and negative outputs, operates with a PWM control, which has proved to be capable of providing stable behavior if the parameters are properly selected. Two models have been used to deal with the existence and stability of the normal regime of operation. The averaging approach has been developed jointly with the Jacobian matrix to deal with the stability of the slow dynamics.

Relevant conclusions have been obtained after the discrete-time analysis. The different order of occurrence of both switchings allows the converter to operate in two different main modes. Moreover, the strategy of control chosen adds a discontinuous boundary

to the system, which has resulted to be depended on the mode of operation. The one-dimensional map has permitted to detect a period-doubling bifurcation by means of simple expressions jointly with some non-smooth bifurcations. Despite the presence of both modes, the study has shown that the value and stability of the main fixed point is not influenced by the mode of operation. Therefore, the dynamics of the converter is characterized by the stability condition and the corresponding non-smooth boundaries. Consequently, a non-smooth bifurcation arises when the condition which establishes the mode of operation of the fixed point is fulfilled.

Higher dimensional maps have provided more accurate predictions, which are required when the ripples of the capacitor voltages increases their weight in the feedback loops. This map also predicts Neimark-Saker bifurcations when the parameters related with the PI term are varied. Moreover, the analysis of the eigenvalues in the neighborhood of the discontinuous boundaries has proved the existence of new flip and Neimark-Sacker bifurcations owing to a discontinuity in the eigenvalues.

Chapter 5

Analysis of the SIMIMO converter with Interleaved Control

Interleaved control will be presented as an alternative control, whose viability will be studied in this chapter. In contrast to the control previously proposed, the nature of this strategy will allow us to generalize the control so as to regulate dc-dc converters with N outputs which can have different polarities. After proposing a generalized power stage, we will analyze both the stability and the boundaries of the system, which will establish the operating region of the converter, by means of averaged and discrete-time models. The usefulness of the different models to determine the dynamics will be also taken into consideration.

5.1 General power stage and interleaved control

5.1.1 Power stage description

The schematic diagram in Fig. 5.1 shows a SIMIMO dc-dc converter that uses a single inductor shared by a generic number of outputs: p positive (non-inverted) and n negative (inverted) polarities, being $N = p + n$. The following elements are defined for each output: an equivalent resistance R_j (considered here for the load), a filter
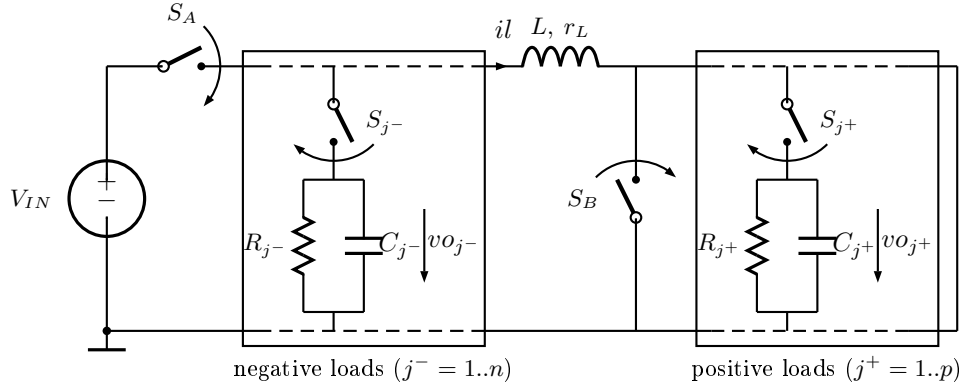
Figure 5.1. Schematic diagram of a SIMIMO dc-dc converter with a generic number of positive and negative outputs.

capacitor C_j, and a specific switch S_j, whose ON state (closed) will activate the charging of the capacitor C_j.

Two extra switches S_A and S_B are also required and work as following. Along the time intervals during which these two switches are ON (and all S_j are OFF (open)), the inductor is connected to the source V_{IN} in order to recover energy from it. This stage of the process is similar to the ON interval of simple boost or buck-boost dc-dc converter and is equivalent to the topology $\mathcal{T}_1$ in the SITITO converter presented in the previous chapter. During the time remainder, S_A and S_B are activated in a complementary way. If S_A is ON and S_B is OFF, then a particular S_j switch, belonging to a positive output, must be ON in order to load the corresponding capacitor C_j. This stage works like a boost converter in the OFF interval. Similarly, if S_A is OFF and S_B is ON, then the switch S_j in the ON state must belong to a negative output, so this part of the process is similar to the OFF interval of a buck-boost converter.

The general power stage also indicates the state variables: the inductor current i_L, and the set of output voltages $\{vo_j, \ j = 1..N\}$.

The diagram in Fig. 5.2 corresponds to a Single-Inductor Two-Output case ($p = 1$ and $n = 1$) (SITITO), which is equivalent to the converter studied in the previous chapter. There is no need here for specific S_j switches, because there is only one output to which inject the current from the inductor when either S_A or S_B results open. Hence, these switches can be substituted by two diodes, whose action is complementary to S_A (negative load) and S_B (positive load). We will assign the indices 1 and 2 to the positive and negative polarities respectively. Notice that the subindexes considered here as 1 and 2 have their correspondence in P and N respectively in the previous chapter.
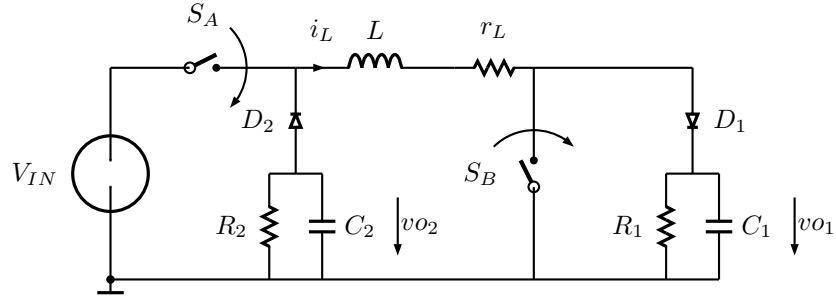
Figure 5.2. Schematic diagram of a SITITO dc-dc converter with positive (1) and negative (2) outputs.

5.1.2 Interleaved control
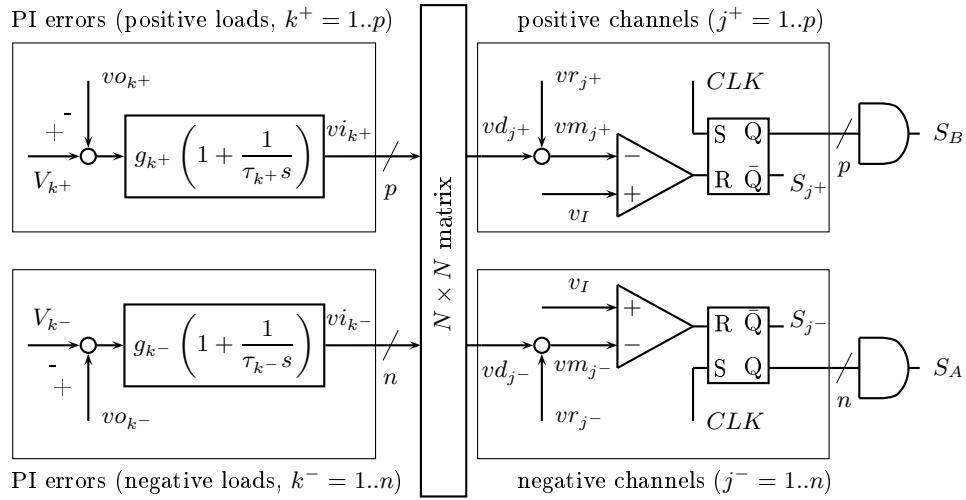
Figure 5.3. Scheme of the control of a SIMIMO dc-dc converter based on multi-phase modulation. The feedback current is $v_I = r_S i$, being r_S the sensing resistance.

A simplified scheme of a multi-phase or interleaved control for a SIMIMO dc-dc converter [15] is shown in Fig. 5.3. This control is made up from N channels, each of them driving a specific switch S_j. Hence, the corresponding capacitor C_j will be charged when the state of the switch S_j is ON. The AND gates are used to achieve the requirement, explained above, that the ON state of switch S_A corresponds to an OFF state of all S_j associated to negative outputs, and the same for S_B considering all S_j switches of the positive outputs.

Let us define the set of inputs as $\{V_j,\ j = 1..N\}$. Similarly to the previous control, the aim of the control is to force the set of voltage outputs vo_j as closed as possible to the corresponding input V_j. Considering the signal errors as follows

$$e_j = V_j - vo_j, \qquad j = 1..N,$$

and taking into account the PI term of the control, it can also be defined the set of signals $\{vi_j,\ j = 1..N\}$ as

$$vi_j = g_j \text{sign}(V_j)(e_j - \sigma_j) \qquad j = 1..N,$$

where $\{g_j,\ j = 1..N\}$ is the set of proportional coefficients of the PI blocks and

$$\sigma_j = \frac{1}{\tau_j} \int (vo_j - V_j)\, \mathrm{d}t \qquad j = 1..N,$$

being $\{\tau_j,\ j = 1..N\}$ the set of corresponding time constants. A generic channel j will be driven by a signal, which will be denoted vd_j. This signal, which plays the role of a dynamical reference, is a linear combination of PI outputs $\{vi_k\}$, given by

$$vd_j = \sum_{k=1}^{N} \alpha_{j,k} vi_k, \qquad j = 1..N,$$

where $\alpha_{j,k}$ are the generic coefficients in the matrix that appears in Fig. 5.3.

Similarly to the control presented in the previous chapter, the regulation is achieved by the comparison of v_I, a signal proportional to the inductor current ($v_I(t) = r_S i_L(t)$), and a set of peak reference signals $\{vm_j,\ j = 1..N\}$ (5.1), which include the corresponding dynamic reference vd_j and a ramp signal vr_j with period T and amplitude $V_U - V_L$.

$$vm_j = vr_j + vd_j. \tag{5.1}$$

Nevertheless, the set of ramp signals have been modified in order to achieve an appropriate regulation of the converter, due to the fact that it is convenient that only one switch S_j is ON at a time. Let us divide the period of a modulating signal into N intervals, so that

$$\sum_{j=1}^{N} \phi_j T = T,$$

where $\{\phi_j T,\ j = 1..N\}$ is the time duration of each phase interval. The strategy used in the interleaved control is based in applying an increment delay of the form

$$\sum_{k=1}^{j} \phi_k,\ k = 1..j,$$

to each of the ramp signals. Therefore, vr_j can be defined as

$$vr_j = V_U - (V_U - V_L)\text{mod}\left(\frac{t}{T} - \sum_{k=1}^{j} \phi_k, 1\right),$$

where mod $(x, 1)$ stands for the modulo of x.

In order to clarify the operation of the control, in Fig. 5.4 the state variables i_L and vo_j, $j = 1..4$ and the peak reference signals vm_j, $j = 1..4$ have been depicted in the steady state, for a SIMIMO converter with $N = 4$ (being $p = 2$ and $n = 2$).

During each phase j, whose duration is $\phi_j T$, and taking into consideration the action of the bistables, the condition $v_I = vm_j$ splits the phase interval into two parts. During the first subinterval, which will be referred as the ON subinterval, all S_j switches remain OFF and both S_A and S_B switches are ON. Therefore, in this subinterval, the inductor receives energy from the source. Afterwards, until the end of that interval $\phi_j T$, a second subinterval is defined for which S_j will be ON and either S_B or S_A will be OFF depending on the polarity of the output: S_B in case positive or S_A otherwise. This second subinterval will be known as the OFF subinterval. During this subinterval one capacitor C_j is charged from the inductor.

The action of the control is given by means of the automatic selection, due to the feedback, of the instants of time that will determine the ratio of both ON and OFF subintervals in every phase. During every OFF subinterval a direct effect is produced on the output that corresponds to the specific switch S_j that has been activated. However, along the ON subintervals, the inductor current is recovered from the source, so involving the rest of the outputs. The total time per cycle to charge the inductor is determined by the addition of all ON subintervals, thus being a combined action of the channels. Consequently, the regulation of each output is achieved through this total ON interval besides the duration of the respective OFF subinterval, thus meaning the stability must be considered for the system as a whole, not for each individual channel or output.

Finally, we will introduce same remarks about the coefficients α. Numerical simulations have revealed that the diagonal coefficients $\alpha_{j,j}$ must be very small or even null in order to ensure stability. This fact is due to an uncompensated effect: if $\alpha_{j,j}$ is defined with such a signum that a decreasing of vm_j would increase the ON subinterval, then an undesirable reduction in the time of loading C_j is produced, otherwise the reduction of the ON subinterval would not be in favor of the need of charge for the inductor in order to increase the current to later be delivered to C_j. Therefore, the feedback will be achieved by the crossed coefficients $\alpha_{j,k}, k \neq j$ of the matrix.

5.2 Closed loop mathematical modeling

5.2.1 Switched model

The switched model gives the set of $2N + 1$ ordinary differential equations for the state variables. In order to take into account the different configurations of the system, the

(a) $v_I = r_S i_L$

(b) vo_1

(c) vo_2

(d) vo_3

(e) vo_4
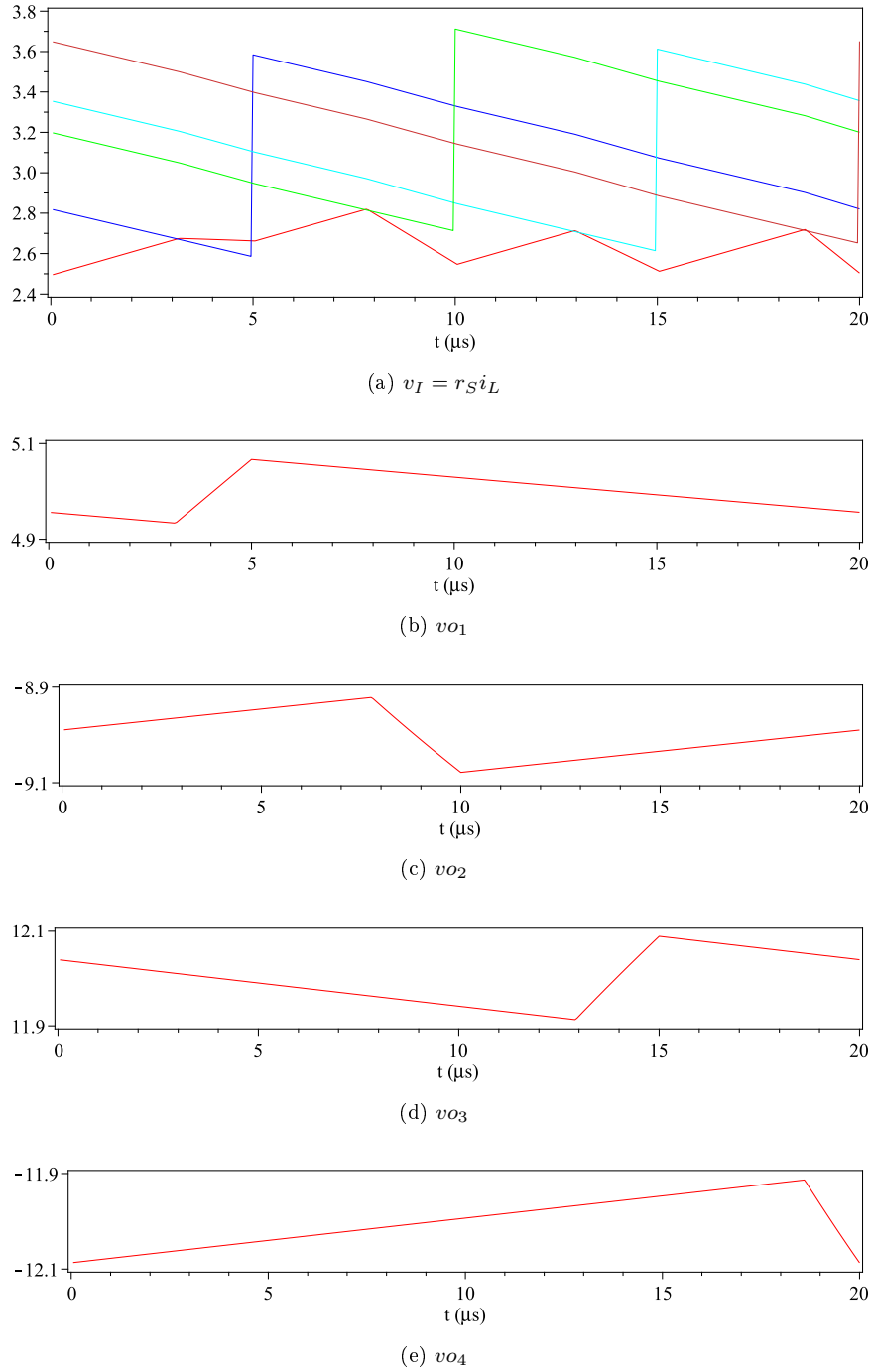
Figure 5.4. Steady state of the SIMIMO dc-dc converter with parameters in Table 5.1. Color code (a): red ($r_S i_L$) blue (vm_1), green (vm_2), cyan (vm_3) and orange (vm_4).

binary variables u_j and u_A are needed. These signals are valued depending on the state of the corresponding switches S_j and S_A: 0 or 1 if open or closed respectively. The switched model can be easily obtained by applying standard Kirchhoff's voltage law to the circuit:

$$\frac{\mathrm{d}vo_j}{\mathrm{d}t} = \frac{1}{C_j}\left(u_j\text{sign}\left(V_j\right)i_L - \frac{vo_j}{R_j}\right), \tag{5.2}$$

$$\frac{\mathrm{d}\sigma_j}{\mathrm{d}t} = \frac{1}{\tau_j}\left(vo_j - V_j\right), \tag{5.3}$$

$$\frac{\mathrm{d}i_L}{\mathrm{d}t} = \frac{1}{L}\left(u_A V_{IN} - \sum_{j=1}^{N} u_j\text{sign}\left(V_j\right)vo_j - r_L i_L\right). \tag{5.4}$$

The first subset of N equations (5.2) refers to the dynamics of each voltage output vo_j, where $\text{sign}\left(\cdot\right)$ stands for the signum function. Additional subset (5.3) deals with N equations for each of the integral terms σ_j in the PI blocks. Finally, the last equation (5.4) deals with inductor current dynamics.

The binary command signal u_j, which is directly related with the time interval in which capacitor C_j is loaded and thus, it is defined 0 from the beginning of ramp vm_j (when the synchronous switching is activated by the clock) until the asynchronous switching defined by the zero condition:

$$vm_j(t) - v_I(t) = 0. \tag{5.5}$$

Afterwards, u_j is valued 1 until the end of the ramp vm_j. Regarding the binary signal u_A, its value will be assigned to 1 if $u_j = 0$, $\forall j$ associated with a negative output, otherwise $u_A = 0$.

Taking into account (5.5), the set of state equations (5.2)-(5.4) is then in closed form and can be used for computer simulations of the whole system.

Before finishing the description of the switched model, let us present some remarks dealing with the operation of the converter. It should be noticed that, in the normal mode of operation (period T orbit), only one output is connected to the inductor. Nevertheless, during the transient or with a dynamics different from the normal regime (subharmonics or chaos), it is possible that the asynchronous switching condition (5.5) occurs before the interval assigned to that output. In this case, two outputs would result interconnected. Two situations can be distinguished here: if the two consecutive intervals involved in this process are defined belonging to outputs with opposite polarity (alternation of positive and negative outputs), that case implies a series connection of a positive and a negative output and the inductor, which will transfer energy to these two outputs. Otherwise, in case that two or more consecutive intervals are related to outputs having the same polarity, a parallel connection of them could be produced. In order to avoid this last situation, the control should include some

(a) i_L (b) vo_j, $j = 1..4$
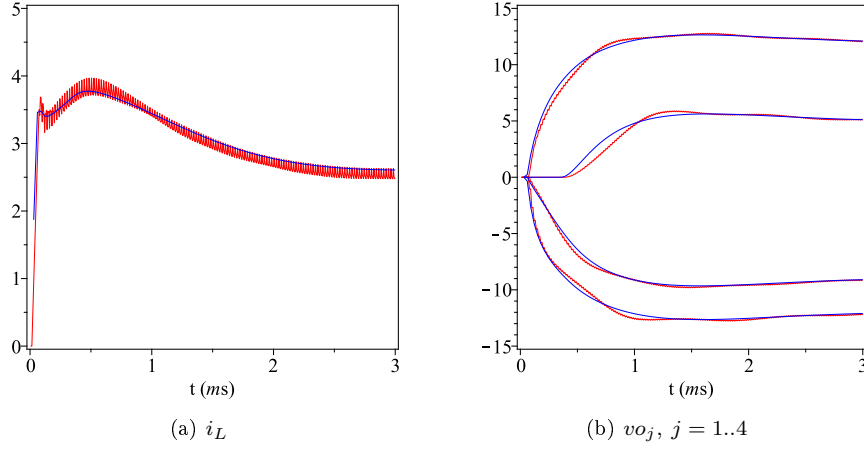
Figure 5.5. Simulated (red) and averaging (blue) transient of a SIMIMO dc-dc converter. The parameters used are in Table 5.1.

complementary logic to inhibit this occurrence or the switch model should incorporate at least the parasitic series resistance of the filter capacitors.

5.2.2 Averaged model

Under assumption of a reduced period T of the modulating signal such as the ripple of the state variables are enough small, the dynamics of the system (5.2)-(5.4) can be approximated by the smooth averaged model. A simple averaged model can be obtained from the switched model by substituting the binary signals by continuous variables. Therefore, if u_j and u_A are replaced by δ_j and δ_A respectively, then the set of $2N + 1$ averaged equations (5.6)-(5.8) are given by

$$\frac{\mathrm{d}\overline{vo}_j}{\mathrm{d}t} = \frac{1}{C_j} \left(\delta_j \mathrm{sign}\left(V_j\right) \bar{i}_L - \frac{\overline{vo}_j}{R_j} \right), \tag{5.6}$$

$$\frac{\mathrm{d}\overline{\sigma}_j}{\mathrm{d}t} = \frac{1}{\tau_j} \left(\overline{vo}_j - V_j \right), \tag{5.7}$$

$$\frac{\mathrm{d}\bar{i}_L}{\mathrm{d}t} = \frac{1}{L} \left(\delta_A V_{IN} - \sum_{j=1}^{N} \delta_j \mathrm{sign}\left(V_j\right) \overline{vo}_j - r_L \bar{i}_L \right), \tag{5.8}$$

where the over bar stands for averaging during one switching period.

The duty ratios δ_j, which are defined as the interval relative to a period T in which the switch S_j is open (OFF), can be obtained explicitly from in terms of the averaged state variables [15] as follows:

$$\delta_j = \frac{1}{V_U - V_L} \left(\sum_{k=1}^{N} \alpha_{j,k} g_k \mathrm{sign}\left(V_k\right) \left(\overline{vo}_k - V_k + \overline{\sigma}_k \right) + r_s \bar{i}_L - V_L \right) \tag{5.9}$$

Parameter	Value	Parameter	Value
V_{IN}	5.0 V	r_S	0.5 Ω
L	39 µH	r_L	0.1 Ω
V_1	5 V	V_2	−9 V
V_3	12 V	V_4	−12 V
R_1	10 Ω	R_2	15 Ω
R_3	22 Ω	R_4	33 Ω
C_1	68 µF	C_2	68 µF
C_3	56 µF	C_4	39 µF
V_U	1.0 V	V_L	0.0 V
τ_j	300 µs	ϕ_j	0.25
$\alpha_{j,j}$	0.0	$\alpha_{j,k},\ j \neq k$	1.0
g_j	0.1	T	20 µs

Table 5.1. Parameter values used in numerical simulations for $N = 4$, being $j, k = 1..4$.

The parameter δ_A refers to the ratio, in period of the modulating signal, in which the inductor is recovering energy from the source. Therefore, this ratio must include the N ON subintervals and the OFF subintervals considering only the positive loads, which is equivalent to exclude the OFF subintervals that involve the load of a negative output. To obtain a formal expression, let us define the binary variable b_j as

$$b_j = 1/2 + \text{sign}\,(V_j)\,/2,$$

so that $b_j = 0$ if $V_j < 0$ and $b_j = 1$ if $V_j > 0$, thus δ_A can be expressed as:

$$\delta_A = 1 - \sum_{j=1}^{N}(1 - b_j)\delta_j.$$

The above equations can be used to get information of the averaged system, in particular slow dynamics stability features. Let us recall here that a periodic orbit of the switching system corresponds to an equilibrium point of the continuous-time averaged system, which can be calculated by imposing the zero field condition to the set of averaging equations (5.6)-(5.8), thus giving the following results:

$$\overline{vo}_j = V_j \tag{5.10}$$

$$\delta_j = \frac{|V_j|}{I_Q R_j} \tag{5.11}$$

$$\bar{i} = I_Q = \frac{V_{IN}}{2r_L}\left(1 - \sqrt{1 - \frac{4r_L}{V_{IN}^2}\sum_{j=1}^{N}\frac{|V_j||V_j'|}{R_j}}\right) \tag{5.12}$$

where $|\cdot|$ stands for the absolute value and $V_j' = (1-b_j)V_{IN}+|V_j|$ (so that $V_j' = V_{IN}-V_j$ if $V_j < 0$ and $V_j' = V_j$ if $V_j > 0$). Finally, from (5.9) and (5.11), the steady state expression for $\overline{\sigma}_j$ can be obtained from the following set of N equations ($j = 1..N$)

$$\sum_{k=1}^{N} \alpha_{j,k} g_k \operatorname{sign}(V_k) \overline{\sigma}_k + r_s I_Q - V_L - (V_U - V_L)\frac{|V_j|}{I_Q R_j} = 0. \tag{5.13}$$

A necessary existence condition for equilibrium is that the discriminant in (5.12) be positive. Besides this, there are two possible solutions if either a positive or a negative signum is considered for the square root term in (5.12), but only the negative one is useful in practice; otherwise, the inductor current and the associated loss of energy would be very high. The stability of this equilibrium point can be studied by the Jacobian matrix of this model, which is given below:

$$
\begin{aligned}
J_{j,k} &= \frac{1}{C_j}\left(\beta_{j,k} + \frac{\alpha_{j,k} g_k \operatorname{sign}(V_j V_k) I_Q}{V_U - V_L}\right) \\
J_{j,N+k} &= \frac{1}{C_j}\frac{\alpha_{j,k} g_k \operatorname{sign}(V_j V_k) I_Q}{V_U - V_L} \\
J_{j,2N+1} &= \frac{1}{C_j}\left(\frac{V_j}{I_Q R_j} + \frac{\operatorname{sign}(V_j) r_S I_Q}{V_U - V_L}\right) \\
J_{N+j,k} &= \gamma_{j,k} \\
J_{N+j,N+k} &= 0 \\
J_{N+j,2N+1} &= 0 \\
J_{2N+1,k} &= \frac{-1}{L}\left(\frac{|V_k|}{I_Q R_k} + \frac{g_k \operatorname{sign}(V_k)}{V_U - V_L}\sum_{j=1}^{N}\alpha_{j,k}V_j'\right) \\
J_{2N+1,N+k} &= \frac{-1}{L}\frac{g_k \operatorname{sign}(V_k)}{V_U - V_L}\sum_{j=1}^{N}\alpha_{j,k}V_j' \\
J_{2N+1,2N+1} &= \frac{-1}{L}\left(r_L + \frac{r_S}{V_U - V_L}\sum_{j=1}^{N}V_j'\right)
\end{aligned}
\tag{5.14}
$$

being $j = 1..N$, $k = 1..N$, $\beta_{j,j} = -1/R_j$, $\beta_{j,k} = 0$ if $k \neq j$, $\gamma_{j,j} = 1/\tau_j$ and $\gamma_{j,k} = 0$ if $k \neq j$.

In Fig. 5.5, the inductor current and the voltage outputs are represented during the transient in a four-output single-inductor dc-dc converter using both the switched and the averaged model.

5.3 One-dimensional discrete-time model

The one-dimensional map that is presented in this section is a first approach that considers only the variations of the inductor current while the rest of the state variables

(the filter capacitor voltages and the integral terms) are assumed to be constant. In addition, the inductor current is approximated by a piecewise-linear time function. This kind of approach is equivalent to the one widely used in boost or buck-boost converters with current programmed control.
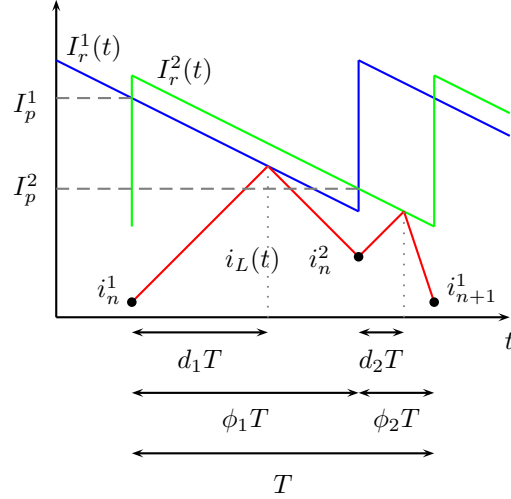
Figure 5.6. Schematic diagram of the current evolution for a SITITO converter ($N = 2$). The functions $I_r^1(t)$ and $I_r^2(t)$ correspond to $v_m^1(t)/r_S$ and $v_m^2(t)/r_S$ respectively.

5.3.1 Map definition

The map will be defined stroboscopically with the periodicity of the modulating ramps. Moreover, in an extended range of parameters, the evolution of the inductor current presents a pattern that is qualitatively repeated every phase (see Fig. 5.6). Taking into account this property, the map can be expressed as a composition of N submappings. Let $P(i)$ be the discrete-time map defined in a whole period T, then

$$i \mapsto P(i) = f^N \circ f^{N-1} \circ ... \circ f^2 \circ f^1(i), \tag{5.15}$$

where f^k corresponds to the submapping in the phase interval k. Considering a linear time dependence of the inductor current in each topology, the evolution of the inductor current in the phase interval k can be approached by

$$i^{k+1} = f^k(i^k) = i^k + (\Delta \texttt{ion} - \Delta \texttt{ioff}^k)d_k + \Delta \texttt{ioff}^k \phi_k, \tag{5.16}$$

where $i^1 = i$, $i^{N+1} = P(i)$ and, generally, i^k corresponds to the value of the state variable i at the beginning of the interval phase k, and thus

$$i^{k+1} = f^k \circ f^{k-1} \circ ... \circ f^2 \circ f^1(i).$$

The current increments that appear in (5.16) are specific for each subinterval and they are defined as the total variation of the inductor current that would be produced if that subinterval lasted for the whole period T. Therefore, taking into account (5.8) and the constant voltage approach ($vo_j \approx V_j$), these increments are

$$\Delta\mathtt{ion} = \frac{V_{IN} - r_L I_Q}{L} T \tag{5.17}$$

$$\Delta\mathtt{ioff}^k = \frac{b_k V_{IN} - |V_k| - r_L I_Q}{L} T \tag{5.18}$$

Notice that in the above expressions the voltage drop in the inductor due to the parasitic resistance r_L, which is expected to be small, is assumed constant using the averaged current I_Q in (5.12).

The duty cycle in each phase interval is modeled as follows

$$d_k = \begin{cases} d_k' & \text{if } d_k' \leq \phi_k, \\ \phi_k & \text{if } d_k' > \phi_k, \end{cases} \tag{5.19}$$

in which

$$d_k' = \frac{I_p^k - i^k}{\Delta\mathtt{ion} - \Delta\mathtt{ir}}, \tag{5.20}$$

and

$$\Delta\mathtt{ir} = -\frac{V_U - V_L}{r_S}.$$

According to (5.19), the generic submapping k is a PWL map with two trams: the (main) unsaturated tram with $d_k = d_k'$ and the saturated tram with $d_k = \phi_k$.

The set of parameters $\{I_p^k, k = 1..N\}$, in which I_p^k is the value of the modulating ramp vm_k at the beginning of the phase interval k divided by the sensing resistance r_S, is still undefined. As the one-dimensional map will be used to determine the existence and stability of the normal regime of operation, then, due to the integral action, the dc-levels of the ramps are considered to be shifted such as the mean value of the inductor current fits the averaged value obtained in (5.12). Therefore, the method proposed here to determine these parameters is to force the mean value of the piecewise-linear continuous function $i_L(t)$ during a whole period T to fit I_Q, when the starting value of i is just the main fixed point and thus, the duty cycles are those predicted by the averaged model (5.11). As d_k corresponds to the ON subinterval in the map, while δ_k does to the OFF subinterval in the averaged model, these ratios are complementarily defined in a phase interval, thus, in the fixed point conditions the duty ratio is defined as

$$d_k^* = \overline{d}_k = \phi_k - \frac{|V_k|}{R_k I_Q},$$

and I_p^k is determined in order to fulfil (5.20) in the fixed point condition

$$I_p^k = i^{*^k} + (\Delta\text{ion} - \Delta\text{ir})\overline{d}_k, \tag{5.21}$$

where i^{*^k}, which corresponds to $i_L(t)$ at the beginning of phase interval k in the period-one case (fixed point) so as to be applied to submapping f^k defined in (5.16), thus giving

$$i^{*^{k+1}} = i^{*^k} + (\Delta\text{ion} - \Delta\text{ioff}^k)\overline{d}_k + \Delta\text{ioff}^k\phi_k. \tag{5.22}$$

The final step is to give an explicit expression of i^{*^1}, which is actually the fixed point of the map P $(i^* = i^{*^1})$, in accordance to the averaging condition

$$I_Q = \sum_{k=1}^{N} \phi_k \overline{i}^k, \tag{5.23}$$

in which $\overline{i}^k$ is the mean inductor current during the phase interval k applied to the k-submapping in the fixed point condition. Taking into account that $i_L(t)$ is a PWL function, it is straightforward that

$$\overline{i}^k = i^{*^k} + \frac{\eta_k}{\phi_k} \qquad k = 1..N,$$

where

$$\eta_k = \Delta\text{ion}\ \overline{d}_k \left(\phi_k - \frac{\overline{d}_k}{2}\right) + \frac{1}{2}\Delta\text{ioff}^k \left(\phi_k - \overline{d}_k\right)^2.$$

Let $\{\Delta i^{*^k}, k = 1..N\}$ be the set of differences between $k-$ and $1st-$ submapping fixed points. This set includes a trivial first member $\Delta i^{*^1} = 0$ for the shake of completeness and the remainder $(k = 2..N)$ are obtained after $k - 1$ iterations of (5.22)

$$i^{*^k} = i^* + \Delta i^{*^k},$$

$$\Delta i^{*^k} = \sum_{l=1}^{k-1} \left((\Delta\text{ion} - \Delta\text{ioff}^l)\overline{d}_l + \Delta\text{ioff}^l\phi_l\right).$$

Finally, inserting the above expressions in (5.23), results

$$I_Q = i^* + \sum_{k=1}^{N} \left(\phi_k \Delta i^{*^k} + \eta_k\right),$$

then

$$i^* = I_Q - \sum_{k=1}^{N} \left(\phi_k \Delta i^{*^k} + \eta_k\right).$$

Parameter	Value	Parameter	Value
V_{IN}	6 V	V_L	0
L	47 μH	V_U	variable
r_L	0.2 Ω	V_1	variable
C_1	22 μF	V_2	−8 V
C_2	22 μF	$\tau = \tau_1 = \tau_2$	20 μs
R_1	33 Ω	$g = g_1 = g_2$	0.02
R_2	12 Ω	$\phi_1 = \phi_2$	$\frac{1}{2}$
$f_s = 1/T$	200 kHz	r_S	1 Ω

Table 5.2. Parameter values used in numerical simulations for $N = 2$.

5.3.2 Validity of the model

The map definition (5.15) has been constructed as a sequence of submappings and requires that the inductor current (more precisely $v_I = r_S i_L$) intercepts each of the modulating signals $vm_k(t)$ in the corresponding phase interval k. These restrictions add two sets of boundary conditions in the map. The first set applies to the value of i^{*^k} with respect to I_p^k so that the duty cycle be positive. Therefore, from (5.20) the first set of validity conditions can be expressed in two equivalent forms

$$\begin{cases} \overline{d}_k > 0, \\ i^{*^k} < I_p^k, \end{cases} \qquad k = 1..N. \tag{5.24}$$

The second set applies to the relative position of the modulating ramps vm_k and can be expressed in the form

$$I_p^k < I_p^{k+1} - \Delta \mathrm{ir}\phi_k, \qquad k = 1..N, \tag{5.25}$$

where the cyclic condition $I_p^{N+1} = I_p^1$ is taken into account.

Notice that (5.25) does not show dependence on the state variable i. When any of these conditions are fulfilled, the dynamics presents a border-collision bifurcation. Actually, the dynamics outside these boundaries should be analyzed redefining the model. Nevertheless, the loss in the symmetry of the system increases greatly the complexity of the map and the extension of the analysis is out of the scope of this dissertation. Therefore, these conditions will be considered here as a validity boundaries of our map.

The set of validity conditions (5.24) (black) and (5.25) (grey) have been depicted in Fig. 5.7 in the parameter space $\{V_U, \phi_1\}$ (Fig. 5.7a) and $\{V_1, \phi_1\}$ (Fig. 5.7b) for $N = 2$. Solid and dashed lines represent the conditions for the phase intervals one and

(a) $V_1 = 6.0\,\text{V}$

(b) $V_U = 0.5\,\text{V}$
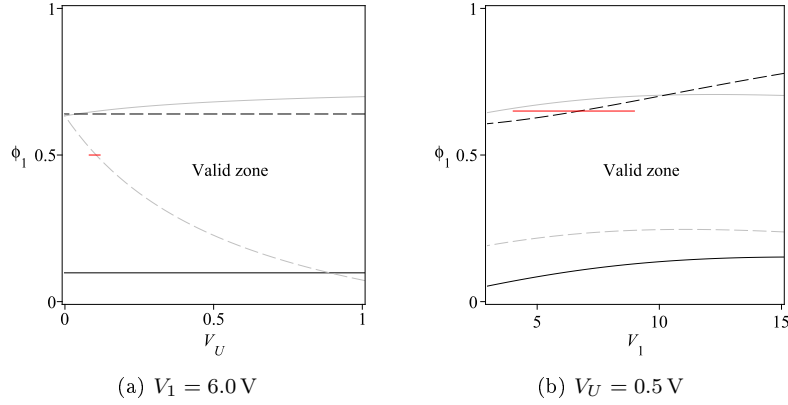
Figure 5.7. Validity curves from (5.24) (black) and (5.25) (grey) for $N = 2$. Solid and dashed lines correspond to the conditions for the phase intervals one and two respectively. The parameters are in Table 5.2.

(a) $V_1 = 6.0\,\text{V}$

(b) $V_1 = 6.0\,\text{V}$ and $V_U = 0.104\,\text{V}$
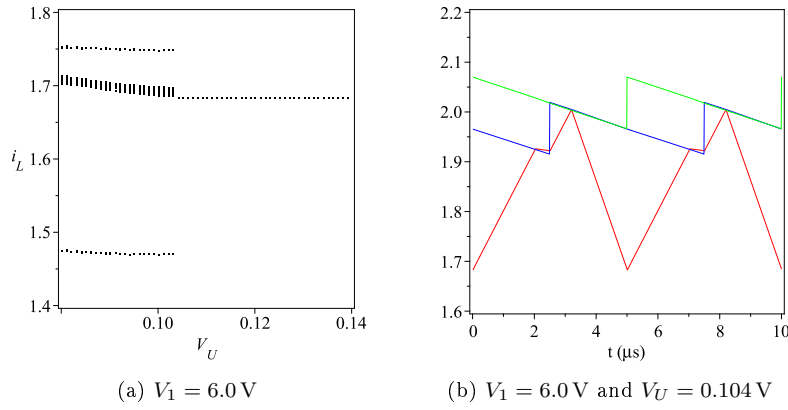
Figure 5.8. Plots obtained with the PSIM simulator for $N = 2$: $i_L(t)$ (red), $I_r^1(t)$ (blue) and $I_r^2(t)$ (green) evolution. The parameters are in Table 5.2.

two respectively. The red line added in Fig. 5.7a represent the parameter variations of the bifurcation diagrams depicted in Fig. 5.8a, where some scenarios have been found in the real system when crossing any of these boundaries. In Fig. 5.8b, the scenario around the bifurcation has been plotted to illustrate the coincidence of both modulated signals. In Fig. 5.9 some scenarios have been plotted to illustrate the nearby of (5.24) condition, taking parameters along the red line in Fig. 5.7b.

In the first case, the bifurcation diagram has been obtained varying the parameter V_U. As it can be appreciated, the diagram in Fig. 5.8a shows a jump in the state variable from a stable one-periodic orbit to a chaotic attractor when the condition (5.25) from the phase two is fulfilled. This kind of non-smooth bifurcation occurs in discontinuous maps (maps with a jump in the state), with which this dynamics could be modeled if
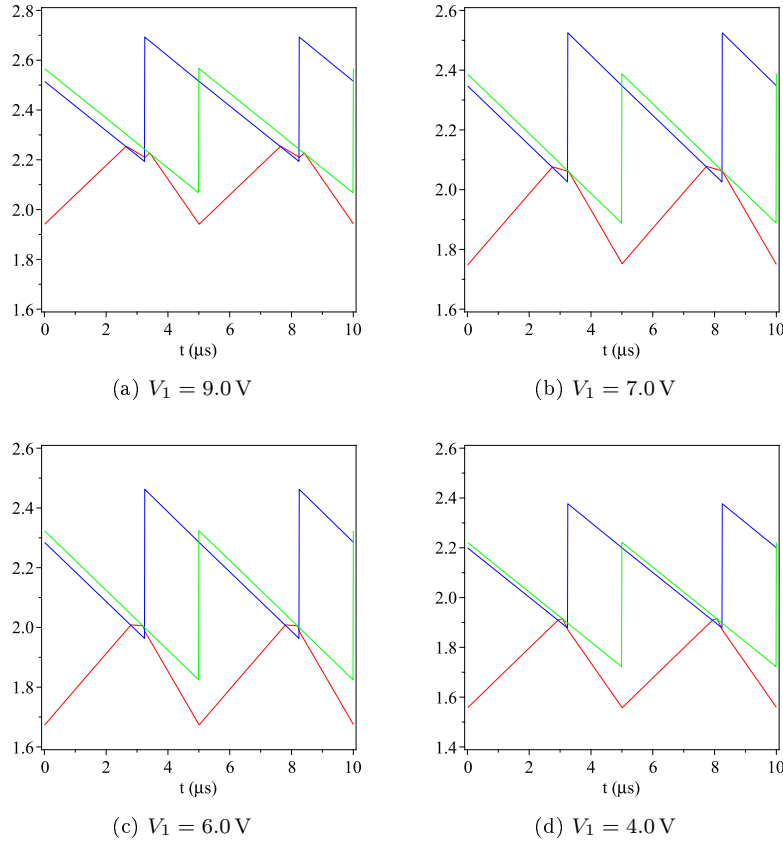
Figure 5.9. Plots obtained with the PSIM simulator for $N = 2$: $i_L(t)$ (red), $I_r^1(t)$ (blue) and $I_r^2(t)$ (green) evolution. The parameters are in Table 5.2 except: $\phi_1 = 0.65$, $\phi_2 = 1 - \phi_1$. In (c) and (b), the two switchings take place in the same phase interval.

the complete map has been taken into consideration. Notice also the equivalence of this bifurcation with the bifurcation seen in the previous chapter when the slope of the intermediate state reaches the slope of the ramp signal.

The second case studied has been depicted in Fig. 5.9. In this situation, four diagrams have been shown to illustrate the persistence scenario of the fixed point when crossing the boundary (5.24). Notice that in Fig. 5.9c and Fig. 5.9d, after crossing the boundary, both asynchronous switchings take place in the same phase interval. Therefore, the dynamics cannot be predicted with the map proposed. When the fixed point is unstable after crossing the boundary, other scenarios can appear, as such the non-smooth period-doubling.

5.3.3 Main mode of the map, fixed point and stability analysis

Taking into account the two trams in each submapping, the map (5.15) can have up to 2^N trams. However, those trams that imply saturation of the duty cycle are not of interest for a real system, thus in practical applications, the configuration to which the relevant fixed point belongs is the one with no duty cycle saturated. This configuration will be called the *main* mode and is analyzed in detail below. In order to simplify the analysis, the (unsaturated) map is rewritten in terms of variations regarding the fixed point of the main mode. From (5.16) and (5.22)

$$i^{k+1} - i^{*^{k+1}} = i^k - i^{*^k} + (\Delta\texttt{ion} - \Delta\texttt{ioff}^k)(d_k - \overline{d}_k)$$

and from (5.20) and (5.21) the variation of the duty cycle is:

$$d_k - \overline{d}_k = -\frac{i^k - i^{*^k}}{\Delta\texttt{ion} - \Delta\texttt{ir}}$$

then, from the above two expressions, the submapping results

$$i^{k+1} - i^{*^{k+1}} = (1 - \alpha_k)(i^k - i^{*^k}) \tag{5.26}$$

where a new set of coefficients $\{\alpha_k, \; k = 1..N\}$ is defined

$$\alpha_k = \frac{\Delta\texttt{ion} - \Delta\texttt{ioff}^k}{\Delta\texttt{ion} - \Delta\texttt{ir}}. \tag{5.27}$$

Finally, the iterative map applied to the variation of current is obtained by the iteration ($k = 1..N$) of submapping (5.26).

$$i_{n+1} - i^* = \prod_{k=1}^{N}(1 - \alpha_k)(i_n - i^*)$$

To simplify the notation, a new parameter λ, which takes into account the effect of all phases in the main mode, is defined

$$\lambda = \prod_{k=1}^{N}(1 - \alpha_k) \tag{5.28}$$

then the map in the main mode, which will be denoted P_m can be expressed as

$$i_{n+1} = P_m(i_n) = \lambda i_n + (1 - \lambda)i^* \tag{5.29}$$

The main fixed point, which will be called i_m and it is obtained applying the condition $i = P_m(i)$, is therefore $i_m = i^*$, in accordance to the conditions imposed in the map definition.

(a) (ρ_1, ρ_2): $(1, 2.5)$ (black), $(-0.5, 2.5)$ (grey)   (b) (ρ_1, ρ_2, ρ_3): $(0.5, 4, 8)$
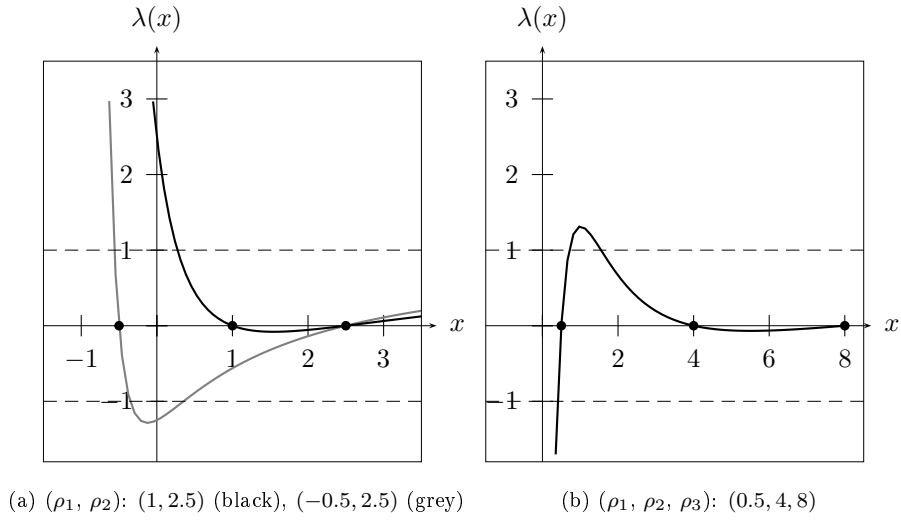
Figure 5.10. Function $\lambda(x)$ for $N = 2$ (a) and $N = 3$ (b).

(a) $V_U = 0.52\,\text{V}$ with $i(0) = 0.0\,\text{A}$ (red) and $i(0) = 4.105\,\text{A}$ (blue)   (b) $V_U = 0.45\,\text{V}$
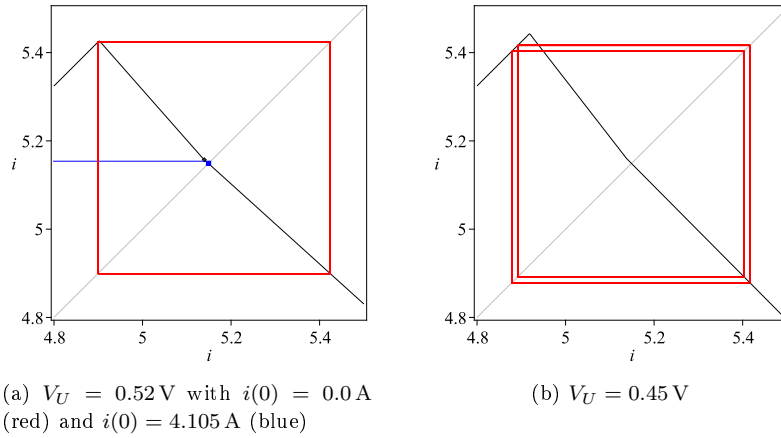
Figure 5.11. Cobweb diagrams around a flip bifurcation. In (a) two different values of $i(0)$ (initial conditions) are used to show the existence of two attractors: the main fixed point and a period-two orbit. Variable parameters shared in both diagrams are: $V_1 = 2.0\,\text{V}$ and $V_2 = -15.0\,\text{V}$.

Due to the linearity of P_m, the asymptotic stability is straight given by the condition

$$|\lambda| < 1 \tag{5.30}$$

In order to describe the feasible scenarios, which can appear in the dynamics of the map as the ramp amplitude is varied, the parameter λ defined in (5.28), in which the coefficients α_k are in (5.27), can be expressed as a function of some dimensionless

(a) Increasing V_U

(b) Decreasing V_U
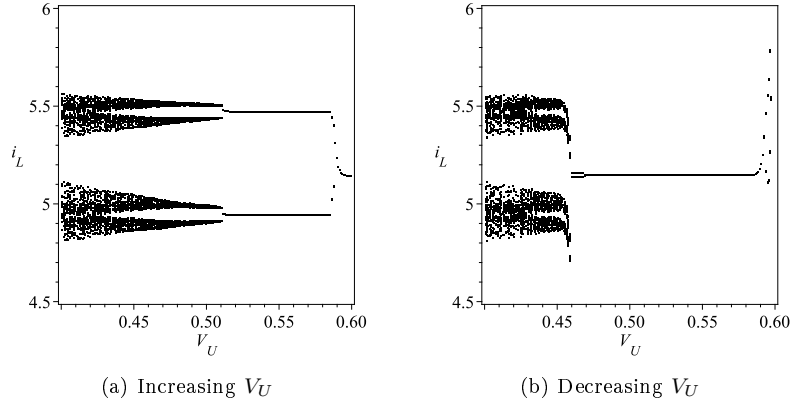
Figure 5.12. Bifurcation diagrams obtained with the PSIM simulator using V_U as the varying parameter. The parameters are in Fig. 5.11.

(a) $V_U = 0.23\,\text{V}$

(b) $V_U = 0.15\,\text{V}$ and $i(0) = 0.0\,\text{A}$ (blue) and $i(0) = 4.1\,\text{A}$ (red)
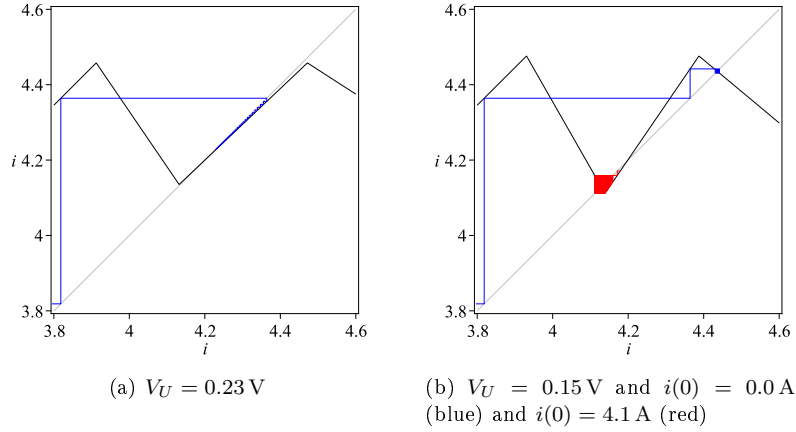
Figure 5.13. Cobweb diagrams around a non-smooth pitchfork bifurcation. After the bifurcation in (b), the main fixed point is unstable and two new attractors coexist: a new fixed point (placed in the fourth tram) and a chaotic attractor. Variable parameters shared in both diagrams are: $V_1 = -V_2 = 12\,\text{V}$.

terms as follows

$$\lambda(x) = \frac{1}{(x+1)^N} \prod_{k=1}^{N} (x - \rho_k), \tag{5.31}$$

where x is defined as

$$x = \frac{V_D L}{(V_{IN} - r_L I_Q) r_S T} \tag{5.32}$$

and

$$\rho_k = \frac{|V_k| - b_k V_{IN} + r_L I_Q}{V_{IN} - r_L I_Q}. \tag{5.33}$$

(a) Flip bifurcation

(b) Non-smooth pitchfork bifurcation
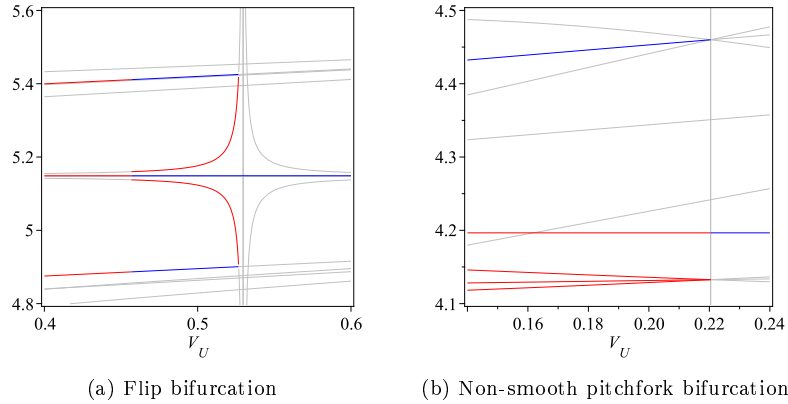
Figure 5.14. Bifurcation diagram obtained analytically using V_U as the varying parameters. The curves represent the stable (blue), unstable (red) and virtual (grey) one and two-periodic orbits. The parameters for (a) are in Fig. 5.11 and for (b) in Fig. 5.13.

(a) Decreasing V_U

(b) Increasing V_U
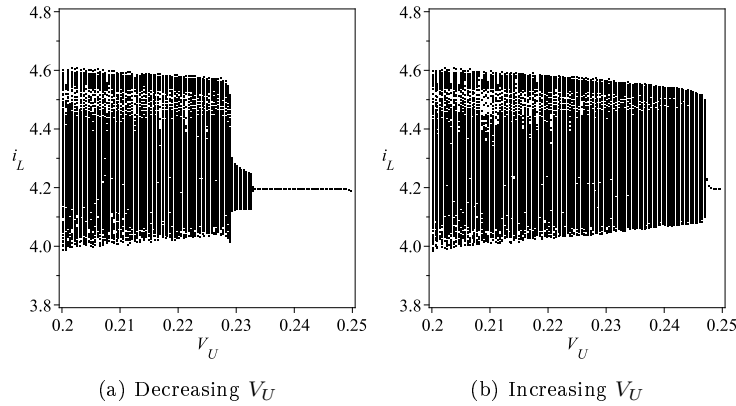
Figure 5.15. Bifurcation diagrams around the pitchfork bifurcation obtained with the PSIM simulator using V_U as the varying parameter. The parameters are in Fig. 5.13 but $g = 0.01$ and $\tau = 200\,\mu s$.

Figure 5.10 shows the function $\lambda(x)$ for $N = 2$ (Fig. 5.10a), $N = 3$ (Fig. 5.10b) and different sets of parameters. This representation accounts for the influence of the ramp amplitude in the stability of the map. Notice that $\lambda(x)$ shows asymptotic behavior ($\lambda(x) \rightarrow 1$ if $x \rightarrow \infty$) and has the singular point $x = -1$, which is located in a non-physical area, considering that the slope of the ramp cannot be inverted ($V_D > 0$).

The map will be unstable if $\lambda < -1$ or $\lambda > 1$, thus provoking two types of bifurcations: period-doubling (see Fig. 5.11) or non-smooth pitchfork (see Fig. 5.13).

In the cobweb diagrams shown in these figures a different number of trams of the map can be observed. The first tram is associated to saturation in both intervals ($x_{n+1} = x_n + \Delta$ion), the second tram (and the fourth in Fig. 5.13) has one interval saturated, and the third tram corresponds to the main mode (no saturation at all). More details above these trams are given below also for the two-output converter ($N = 2$).

In Fig. 5.11a, $\lambda = 0.907$ and hence, i_m is stable. Furthermore, it is shown in the same figure the coexistence with a stable period-two orbit. It will be proved below that this scenario, in which these two attractors coexist, is always given in the neighborhood of a flip bifurcation in our system. On the other hand, in the diagram depicted in Fig. 5.11b, i_m is unstable ($\lambda = 1.010 > 1$) and a two-piece chaotic orbit exits in which all the trams of the map are involved. Cobweb diagrams in Fig. 5.13 are related to a pitchfork bifurcation. In this case, after the bifurcation (see Fig. 5.13b), two new fixed points appear in the second and forth trams. The first fixed point is unstable whereas the last one is stable and coexists with a chaotic orbit, which involves the second and third trams of the map.

Finally, Fig. 5.14 shows the one and two periodic orbits using V_U as the varying parameter. Blue and red lines stand for stable and unstable orbits whereas grey lines represent virtual orbits. Notice in the diagrams the coexistence of the attractors. The basin of attraction in Fig. 5.14a is determined by an unstable period-2 orbit, whereas in Fig. 5.14b, the boundary is given by the unstable main fixed point.

The validity of this analysis has been proved in Fig. 5.12 and Fig. 5.15, showing that the bifurcation points varying V_U are close to the predicted values.

5.3.4 Stability analysis of the main fixed point in a SITITO dc-dc converter

In this section, we will study deeply the dynamics of the two-output case with opposite polarity converter. As it is mentioned above and show in Fig. 5.11 and Fig.5.13, the one-dimensional map can have up to four trams. The diagrams in Fig. 5.16 show the waveforms of the inductor current ($i_L(t)$) and the two references during a period. The different waveforms correspond to a varying initial condition ($i_L(0)$). The continuous line corresponds to a generic initial value in the main mode and the dotted lines are the critical cases associated to the border of the trams. In Fig. 5.16a there are only two borders and consequently, the map is defined with three trams, whereas in Fig. 5.16b there are three borders corresponding to four trams.

The relative value of dimensionless parameters $\{x, \rho_1, \rho_2\}$ defined previously can help us to determine the number of pieces and their slope, which applies for intervals with increasing values of the inductor current in accordance to the following rules:

- The first and simplest tram corresponds to the complete saturation, $i_{n+1} = i_n + \Delta \texttt{ion}$, then it has a unit slope.

- The second tram corresponds to the saturation of the first phase, therefore the slope of this tram of the map is given by the expression $(x - \rho_2)/(x + 1)$, which will result positive if $x > \rho_2$ (negative otherwise).

- The third tram corresponds to the main mode or unsaturated operation. Its slope can be obtained from (5.31) for $N = 2$ and is expressed as

$$\lambda(x) = \frac{(x - \rho_1)(x - \rho_2)}{(x + 1)^2} \tag{5.34}$$

and this is positive if x is outside the interval (ρ_1, ρ_2) or negative if x is inside this interval.

- The fourth tram exists only if the time-slope of the inductor current in the first phase is more negative than the slope of the ramp $(x < \rho_1)$, thus enabling the saturation in the second phase. The slope of this tram of the map is therefore given by the expression $(x - \rho_1)/(x + 1)$, which will always be negative.

(a) Three pieces (b) Four pieces
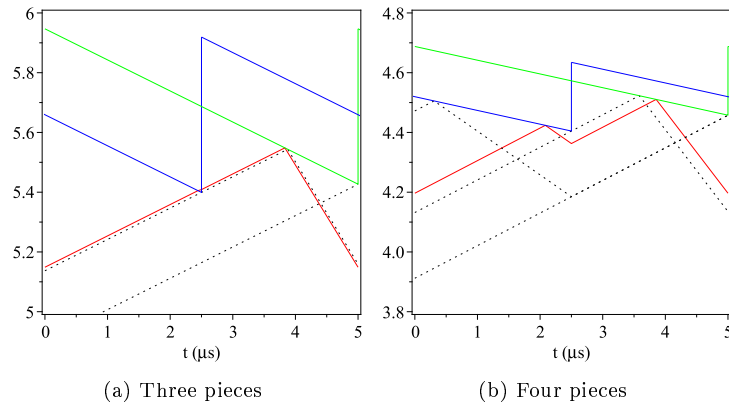
Figure 5.16. Evolution of the inductor current (fixed point and critical values) and references (see Fig. 5.8 for color code). The parameters are in Fig. 5.11 (a) and Fig. 5.13 (b).

In what follows, we will consider as the first phase the one corresponding to the lower time-slope of $i_L(t)$, such that $\rho_1 < \rho_2$. This criterion cannot modify the final conclusions, the only difference lies in the values of the fixed points. Notice also that, in general, due to the asymmetry in the expression of parameters (5.33), the first channel will likely correspond to the positive output $(V_1 > 0)$ and this is necessarily true if $\rho_1 < 0$. In addition, the following restrictions apply to these parameters: $\rho_1 > -1$ and $\rho_2 > 0$.

To sum up, the highest zero of $\lambda(x)$ will be placed always in the positive axis, whereas the lowest one can be positive or negative, but not less than -1. Moreover, the function $\lambda(x)$ will present always a minimum value at

$$x_{MIN} = \frac{\rho_1 + \rho_2 + 2\rho_1\rho_2}{2 + \rho_1 + \rho_2}, \qquad (5.35)$$

in which the value of λ is

$$\lambda_{MIN} = \frac{-(\rho_2 - \rho_1)^2}{4(1 + \rho_1)(1 + \rho_2)}. \qquad (5.36)$$

Therefore, a flip bifurcation is possible if $\lambda_{MIN} <= -1$ and at the two critical values of x

$$x_{FLIP} = \frac{1}{4}\left(\rho_1 + \rho_2 - 2 \pm \sqrt{(\rho_1 - \rho_2)^2 - 4(1 + \rho_1)(1 + \rho_2)}\right). \qquad (5.37)$$
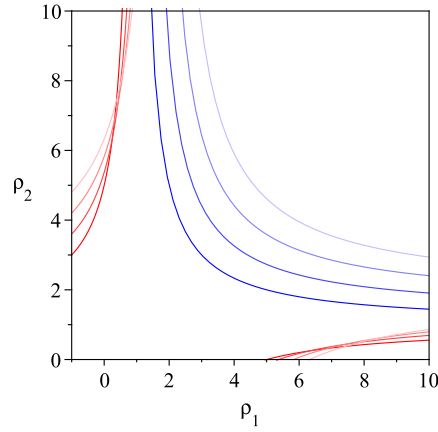
Figure 5.17. Flip (red) and non-smooth pitchfork (blue) bifurcation curves in the parameter space $\{\rho_1, \rho_2\}$ for different values of x.

A second possible bifurcation appears for $\lambda(x) = 1$. In this case the slope of the map in the main fixed point is positive and the scenario is more similar to a pitchfork bifurcation with non-smooth features. Notice that the second iteration of a map with a parameter set that a flip bifurcation occurs will deal with such a kind of bifurcation. The relevance of our map is that it is composed by two submappings, and it is the composition of the two submappings that fits the threshold condition ($\lambda = 1$). Considered separately, the first submapping would have a tram with a negative slope $-1 < (x - \rho_1)/(x + 1) < 0$ and the second submapping with a more negative slope $(x - \rho_2)/(x + 1) < -1$. The critical value for this bifurcation is

$$x_{PFORK} = \frac{\rho_1\rho_2 - 1}{2 + \rho_1 + \rho_2}, \qquad (5.38)$$

which always satisfies the inequality $x_{PFORK} < \rho_1$. From a practical point of view, this bifurcation will not occur if $x_{PFORK} < 0$ or equivalently if $\rho_1 < 1/\rho_2$. Therefore,

a sufficient but not necessary condition to avoid this bifurcation is that the positive output reference be inferior to the input voltage ($V_1 < V_{IN}$). In Fig. 5.10a, $\lambda(x)$ is depicted using two different set of parameters.

To obtain a more general picture of the region of parameters for which these non-smooth bifurcations (flip and pitchfork) can appear, two set of two-dimensional bifurcation diagrams in (ρ_1, ρ_2) space are depicted in Fig. 5.17. The lateral (red) set of curves are those obeying the flip condition $\lambda(\rho_1, \rho_2, x) = -1$, in which x is the variable parameter. The envelope of these curves are two straight lines that obey condition $\lambda_{MIN} = -1$ in (5.36) and can explicitly be expressed as

$$\rho_2 = (3 \pm 2\sqrt{2})\rho_1 + 2(1 \pm \sqrt{2}). \tag{5.39}$$

The central (blue) set corresponds to the parametric curves $\lambda(\rho_1, \rho_2, x) = 1$. Notice that if $x = 0$, the expression of the curve is: $\rho_1\rho_2 = 1$. The main fixed point (i_m) is stable in the inner part of the diagram bounded by the pitchfork and the two flip curves for each value of the parameter x.

5.3.5 Non-smooth bifurcations of the main fixed point

As it is explained above, the definition of the duty cycles must take into account the presence of *boundaries* in the model. One of these limits is analyzed in (5.19). Another limit that has to be accounted for is the presence of the discontinuous conduction mode (DCM). These limits can formally be expressed as

- **High duty cycle saturation**: The first set of boundaries is given when in a generic phase k, the duty cycle becomes equal to that phase (ϕ_k). Therefore, bifurcation curves $\Pi_1^k(i_m)$ are defined as follows

$$\Pi_1^k(i_m) = \phi_k - d_k(i_m^k) \qquad k = 1..N. \tag{5.40}$$

  It is important to remark that, although the main fixed point cannot cross any of the boundaries in a physical set of parameters, (5.40) take relevance in the non-smooth bifurcation of higher periodic orbits.

- **Discontinuous conduction mode**: The second set of boundaries is given when the inductor current drops to zero, therefore, bifurcation curves $\Pi_2^k(i_m)$ are defined as follows

$$\Pi_2^k(i_m) = i_m^k \qquad k = 1..N. \tag{5.41}$$

5.4 Higher dimensional discrete-time model

5.4.1 Definition of the map

A more accurate map, which considers the evolution of all the state variables of the system, is presented in this section. Though the evolution of the inductor current $(i_L(t))$ will be also considered linear in each topology, the higher variations of i_L during a cycle influence significantly the evolution of the capacitor voltages, even the integral variable, in such a way that nonlinear terms must be taken it into account. Therefore, the one-dimensional PWL map (P) will be redefined below as a $(2N+1)$-dimensional piecewise-smooth (PWS) map, which, as before, can be expressed as a composition of the k-submappings (f^k):

$$P(\mathbf{x}) = f^N \circ f^{N-1} \circ ... \circ f^2 \circ f^1(\mathbf{x}) \tag{5.42}$$

$$\mathbf{x}^{k+1} = f^k(\mathbf{x}^k) \tag{5.43}$$

where $\mathbf{x}^1 = \mathbf{x}$, $\mathbf{x}^{N+1} = P(\mathbf{x})$ and, generally, $\mathbf{x}^k$ corresponds to the value of the vector of state variables $\mathbf{x} = (i, vo_1, vo_2, ..., vo_N, \sigma_1, \sigma_2, ..., \sigma_N)$ at the beginning of the interval phase k, and thus

$$i^{k+1} = i^k + (\Delta\texttt{ion} - \Delta\texttt{ioff}^k)d_k + \Delta\texttt{ioff}^k\phi_k$$

$$vo_j^{k+1} = vo_j^k + \left(\delta\texttt{va}_j^k + \frac{1}{2}\delta\texttt{vb}_j^k\right)\delta_j^k + \delta\texttt{vc}_j^k\phi_k$$

$$\sigma_j^{k+1} = \sigma_j^k + \frac{T}{\tau_j}\left((vo_j^k - V_j)\phi_k + \left(\frac{1}{2}\delta\texttt{va}_j^k + \frac{1}{6}\delta\texttt{vb}_j^k\right)(\delta_j^k)^2 + \frac{1}{2}\delta\texttt{vc}_j^k\phi_k^2\right)$$

being $j = 1..N$.

As in the one-dimensional approach, parameters $\Delta\texttt{ion}$ and $\Delta\texttt{ioff}^k$ are defined in (5.17) and (5.18) and d_k in (5.19) and (5.20). To make more understandable the expressions of the map, the variables $\delta\texttt{va}_j^k$, $\delta\texttt{vb}_j^k$ and $\delta\texttt{vc}_j^k$ have been included, which are associated with the variations of the capacitor voltage and the integral term and are defined as follows

$$\delta\texttt{va}_j^k = \frac{T}{C_j}\texttt{sign}(V_j)(i^k + \Delta\texttt{ion}\ d_k),$$

$$\delta\texttt{vb}_j^k = \frac{T}{C_j}\texttt{sign}(V_j)\Delta\texttt{ioff}^k(\phi_k - d_k),$$

$$\delta\texttt{vc}_j^k = -\frac{vo_j^k}{R_jC_j}T.$$

The duty ratio δ_j^k is defined so as to take into account the fact that every capacitor (C_j) is only loaded during its corresponding interval (j):

$$
\delta_j^k = \begin{cases} \phi_k - d_k & \text{if } k = j, \\ 0 & \text{if } k \neq j. \end{cases}
$$

One of the most significant improvements of this redefinition of the map is that the members of the set $\{I_p^k\}$, which are used to obtain d_k' from (5.20), are no longer constant, but function of the state variables. Hence, in accordance to the definition of the modulating signal in (5.1), these terms must be calculated as follows.)

$$
I_p^k = \frac{1}{r_S} \left(V_U - \sum_{j=1}^{N} \alpha_{k,j} g_j \text{sign} \left(V_j \right) \left(vo_j^k - V_j + \sigma_j^k \right) \right) + \Delta \text{ir}(1 - \phi_k).
$$

5.4.2 Study of the fast scale dynamics for $N = 2$

The one-dimensional map can predict bifurcations related to the ripple of the inductor current. The major advantage of this map is the relatively reduced number of parameters to deal with the analysis. In fact, the stability of the fixed point can be verified using the polynomial fraction function (5.31), which has a number of roots (non-dimensional parameters defined in (5.33)) equal to the outputs (N), applied to the non-dimensional parameter x defined in (5.32) and tunable by means of the amplitude of the ramp.

Roughly, those bifurcations are more or less accurately predicted by the simplest map depending on the ripple of the capacitor and integral voltages and also of the weight of these terms in the feedback. Two-dimensional bifurcation diagrams (mostly in the $\{T, V_U\}$ parameter space) in Figs. 5.18 and 5.19 show the deviation of the one-dimensional map of a SITITO dc-dc converter in some illustrative cases, which account for a selection of parameters neglected in the one-dimensional map but considered in the five-dimensional map. In general, a set of bifurcation curves are plotted in these diagrams and therefore, three parameters have been considered at once. The red lines have been obtained by means of the one-dimensional map approach whereas each continuous grey line uses a variable intensity to identify the value of the parameter among those predefined in the set. Figure 5.18 deals with flip bifurcation curves whereas Fig. 5.19 does with a case in which a non-smooth pitchfork bifurcation curve is found with the one-dimensional approach.

Concerning the deviation of the prediction of the flip bifurcation, two sets of flip bifurcation curves using different values of the PI gain (g_k), have been depicted in Fig. 5.18a and Fig. 5.18b fixing the values of the time constants of the PI terms to 200 µs and 50 µs respectively. An enlargement of both plots, between which no quantitative

(a) $\tau = 200\,\mu s$

(b) $\tau = 50\,\mu s$

(c) Zoom view of (a) and (b)

(d) $\tau = 50\,\mu s$, $g = 0.1$ (grey), $g = 0.02$ (black)
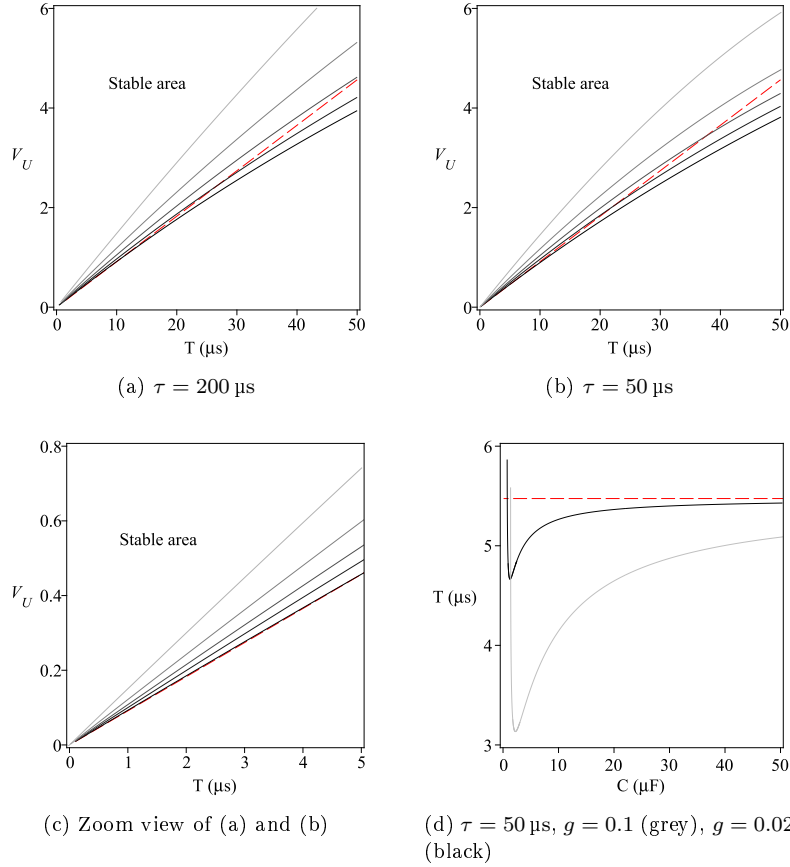
Figure 5.18. Flip bifurcation curves using (5.15) (dashed red line) and (5.42) (solid grey line) maps for the values of g: 0.5 (light), 0.2, 0.1, 0.05 and 0.01 (dark). The parameters are in Table 5.2 except: $V_1 = 2.0\,V$ and $V_2 = -15.0\,V$. The stability of the main fixed point is reached at high values of V_U and low values of C.

difference can be appreciated, has also been included. Notice that (see Fig. 5.18c) for low values of g_k, these curves tend to the one-dimensional approach. It can also be appreciated that the bifurcation curves do not tend to the one-dimensional approach as the period of the modulated signal is decreased. Diagram in Fig. 5.18d reveals the influence of the ripple of the capacitor voltages; in this case ($\{C, V_U\}$) is used as parameter subspace. Notice that the prediction of the flip bifurcation is worsened as the value of g_k is increased.

Similar analysis has been developed in the range of parameters for which the one-dimensional approach predicts a non-smooth pitchfork bifurcation. It is relevant to note here that we have found the equivalence of the pitchfork bifurcation curve in the one-dimensional map to Neimark-Sacker bifurcation curves (related with a pair of complex eigenvalues crossing the unit circle) in the five-dimensional map. Hence,

(a) $\tau = 50\,\mu s$

(b) $\tau = 200\,\mu s$

(c) Zoom view of (a)

(d) Zoom view of (b)
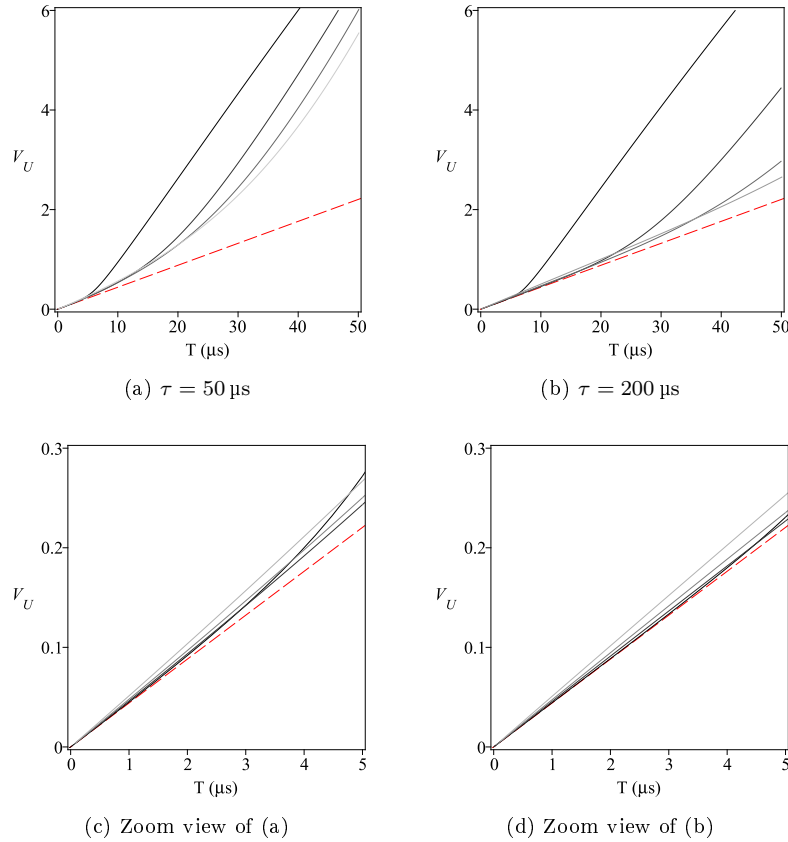
Figure 5.19. Neimark-Sacker/Pitchfork bifurcation curves using (5.15) (dashed red line) and (5.42) (solid grey line) maps for different values of g: 0.2 (light), 0.1, 0.05 and 0.01 (dark). The parameters are in Table 5.2 except: $V_1 = -V_2 = 12.0\,V$. The stability of the main fixed point is reached at high values of V_U.

Fig. 5.19 shows the comparison between both bifurcation curves by using the two approaches. In contrast to the flip bifurcation curves, as the period is increased, the curves suffers a completely change in their tendency, moving away of the one-dimensional approach. Conversely, for low values of T, the deviation between the two curves is similar to the deviation in the prediction of the flip bifurcation. Therefore, the higher-dimensional map predicts a significantly reduced region in which the main mode is stable, especially when g is decreased.

Finally, similar results are found in Fig. 5.20 using the time constant in the PI blocks (τ). In this range of parameters, it can be observed that when the period of the modulation (T) is increased, the range of values for the ramp amplitude is increased (showing a stable main fixed point), while in the Neimark-Sacker bifurcation this range is decreased.

(a) 200 µs (dark), 50 µs, 25 µs and 20 µs (light). Neimark-Sacker: 25 µs (dark) and 20 µs (light).

(b) 200 µs (dark) and 50 µs (light).
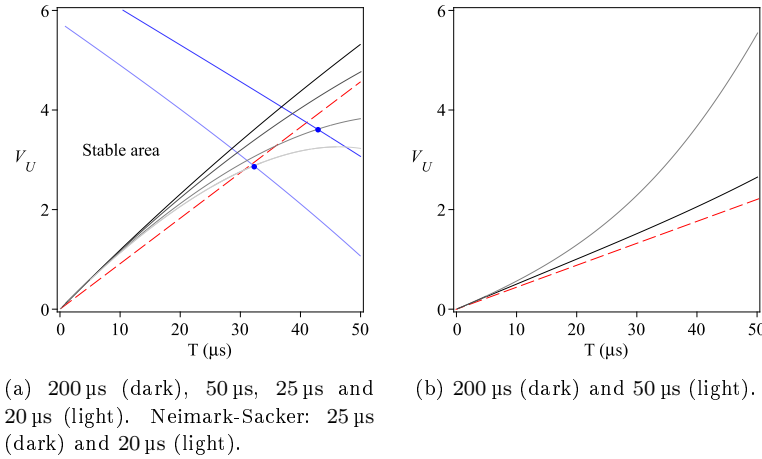
Figure 5.20. Flip (red and grey) and Neimark-Sacker (blue) (a) and Neimark-Sacker / Pitchfork (b) bifurcation curves using (5.15) (dashed red line) and (5.42) (solid grey or blue lines) maps for different values of τ_k. The parameters are in Table 5.2 except: $V_1 = 2.0$ V and $V_2 = -15.0$ V (a) and $V_1 = -V_2 = 12$ V (b). The stability of the main fixed point is reached at higher values of V_U.

Notice that Fig. 5.20a also shows another smooth bifurcation, a Neimark-Sacker, when the parameter τ is reduced. In contrast to the Neimark-Sacker bifurcation seen above which was related with the non-smooth Pitchfork bifurcation, this instability cannot be predicted by means of the one-dimensional map because it is related with the low frequency dynamics. As it can be appreciated in the figure, the stable zone is reduced drastically as the parameter τ is decreased, adding a higher critical value of V_U.

5.5   Conclusions

In this chapter, an interleaved control has been proposed to regulate a generalized SIMIMO converter, which can provide multiple output voltages with different polarities. The dynamics has been analyzed by means of averaged models and discrete-time models using different approaches.

Firstly, expressions for the generalized averaged model have been obtained, including the Jacobian matrix, whose eigenvalues determine the stability of the equilibrium point. Similarly to the results obtained in the previous chapter, the averaged model provides simple expressions for the equilibrium point, which correspond to limit cycles in the real system, and the duty cycles. These results can help us to determine the available region of the converter and are required to establish the expressions for the one-dimensional map. No deep analysis has been developed using this model because averaged models are not able to predict the bifurcations associated to the current ripple and most of the non-smooth bifurcations.

The analysis of a generalized one-dimensional map has permitted to obtain simple expressions useful to determine the stability of the main mode of operation. Moreover, though the discrete-time model does not include all modes of operation of the converter, the boundaries of the validity of the proposed model have also been established. The crossing of any of these boundaries is known to yield a border-collision bifurcation, which can imply several scenarios ranging from sudden jump to chaos to persistence. Furthermore, the values of the phase intervals ϕ_j can be properly selected to avoid any of these non-smooth bifurcations.

Due to the fact that the dynamics of the converter can be modeled with a three-piece linear map in a determined region of the parameters, the result obtained in chapter 3 can be useful to reduce the possible scenarios that can appear in the dynamics of the converter. One of the most relevant results is the proof of the coexistence of the one and two-periodic orbit in the neighborhood of a flip bifurcation.

Concerning the stability, in contrast to the non-interleaved control seen in the previous chapter, in which stability is lost only under the occurrence of the eigenvalue crossing the critical value -1, the analysis of the interleaved control has revealed that the instability is prompts to appear also if the eigenvalue crosses the critical value 1. In this last case, numerical simulations from the switched model show that behavior of the converter in the neighborhood of this bifurcation is similar to a Neimark-Sacker bifurcation. Higher-dimensional discrete-time models prove that the bifurcation of the real system is actually a Neimark-Sacker.

Nevertheless, when the ripples of the capacitor and integral voltages cannot be neglected, the accuracy of the predictions that are obtained with the one-dimensional map is not satisfying and higher-dimensional discrete-time models are required. In this case, the higher complexity of the expressions and, consequently, the time increment of the numerical simulations is made up for the accuracy in the prediction of the instability. Otherwise, non-smooth bifurcations can be properly determined by using the expressions given by a one-dimensional PWL map.

Chapter 6

Experimental measurements

In this chapter, several experimental measurements obtained with a SITITO prototype will be presented. The use of a micro-controller to generate the driven signals of the switches has permitted to study the two different strategies of control presented in this dissertation. Different dynamics of the converter will be measured including the normal operation regime, periodic orbits and chaos.

6.1   Description of the system

A prototype of a SITITO DC-DC converter has been implemented to prove the validity of the regulator and to confirm the results of the study realized in the previous chapters. Figure 6.1 shows the physical implementation of both the power and the control stages. In order to manage with different strategies of control, the regulation of the converter has been realized by means of a micro-controller (LPC2138), which computes the switching instants by processing the value of inductor current and both capacitor voltages acquired periodically, according to the specific strategy of control. In this stage, the algorithm implemented reproduces the analogical controls SPC and IC explained in Chapters 4 and 5.

The power circuit is regulated by two command signals. These voltages are previously adapted by two dedicated MOS inverting drivers from MAXIM (MAX626), and then applied to the MOSFET IRF9Z34S (p channel) and IRL530N (n channel). The diodes

(a) Power stage   (b) Control stage
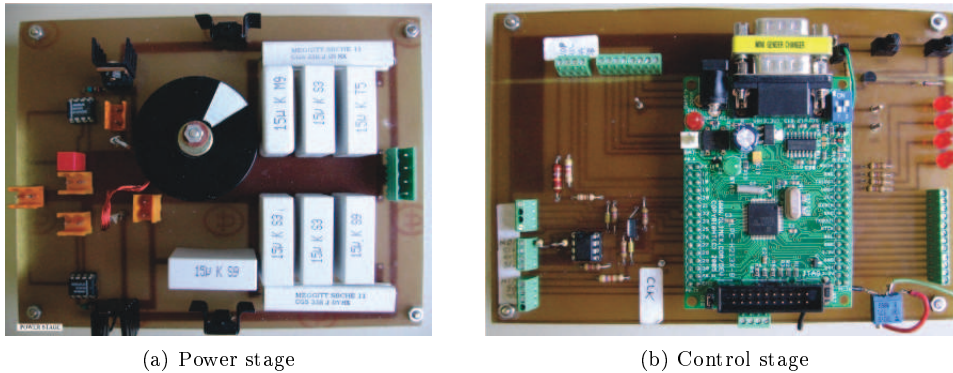
Figure 6.1. Prototype of a SITITO converter composed by the power and control boards.

are two Schottky barrier diodes (6CWQ04FN) and the inductor current is sensed using the current probe PR30. Concerning the value of parameters of the power stage, both capacitors and resistors can be selected to find a specific dynamics. The value of the inductance is determined by an algorithm implemented in the micro-controller before starting the regulation of the converter. According with this experimental measures, the value of the inductor used in the numerical simulations has been fixed to $640\,\mu H$. Finally, its parasitic resistance r_L has been estimated about $0.7\,\Omega$.

Let us now summarize the technical capabilities of the circuit of control. The parameters of this stage, such as the amplitude of the modulating signal, the voltage references, the gains and time constants of the integral control, are configured in the algorithm and loaded into the micro-controller memory. All these parameters can be varied during the experimental measurements. Despite the micro-controller can operate up to $60\,MHz$, the A/D conversions of V_{IN}, i_L and both capacitor voltages, which need around of $2.6\,\mu s$, and the number of operations required to predict the switching instants fix the maximum frequency of the modulated signal about $10\,kHz$. Moreover, the operations needed in the initial part of every period force that the first switching cannot be programmed before the 20% of that period. Notice that this restriction can be relevant in the transient regime and in critical conditions, even during the normal regime, in the presence of noise. These limitations have resulted more crucial in the normal functioning of the converter in case of the interleaved control, due to the fact that the algorithms are more complex and, besides this, the first switching is given early.

Concerning the algorithms used to simulate the two controls, the duty cycles of both switches are established by using the analytical expressions similar to those obtained in the development of the one-dimensional discrete-time models. Nevertheless, there exist some differences. The most relevant one deals with the value of the peak references, which must be known in order to predict the switching instants and their value cannot be computed exactly with the expressions developed in the analysis of

Parameter	Value	Parameter	Value
V_{IN}	6.0 V	V_L	0.0
L	640 µH	V_U	variable
r_L	0.7 Ω	V_P	variable
C_P	45 µF	V_N	-7.0 V
C_N	45 µF	$\tau_P = \tau_N$	200 µs
R_P	22 Ω	$g_P = g_N$	0.02
R_N	33 Ω	r_S	1 Ω
$f_s = 1/T$	10 kHz		

Table 6.1. Parameter values used in the experimental and numerical results.

the one-dimensional map. Therefore, the complete expressions given by the switched models of both strategies of control are used. These are functions of the capacitor voltages, whose real value is acquired periodically, and the integral terms. Due to the limitations in the computing time of the micro-controller, the evaluation of the integral state variables has been simplified, considering the voltages as constant values in each period. This strategy reduces the number of operations but can modify the dynamics of the converter. As it will be observed bellow, one of the main consequences of this method concerns the mean value of the capacitor voltages. Due to the action of the integral control implemented here, the mean value of the capacitor voltages is forced to be equal to its corresponding voltage reference in successive instants of acquisition of the voltage instead of the whole period. Besides this, more complex deviations in the dynamics can be produced and will be analyzed in future works.

6.2   Single-Phase Control

In this section, several dynamical behaviors of the SITITO converter driven by the SPC control are presented. The fixed parameters chosen in the different experimental measurements and numerical simulations are summarized in Table 6.1. Notice that V_U and V_P will be the unique varying parameters in this section.

6.2.1   Normal operation regime

Concerning the normal operation regime, two different sets of parameters, according to the technical limitations of the prototype, have been chosen to illustrate the steady-state response of the SITITO converter regulated by the control SPC when the converter operates in the modes $\mathcal{M}_P$ and $\mathcal{M}_N$ described in Chapter 4.

(a) i_L (b) i_L

(c) v_P (d) v_P

(e) v_N (f) v_N
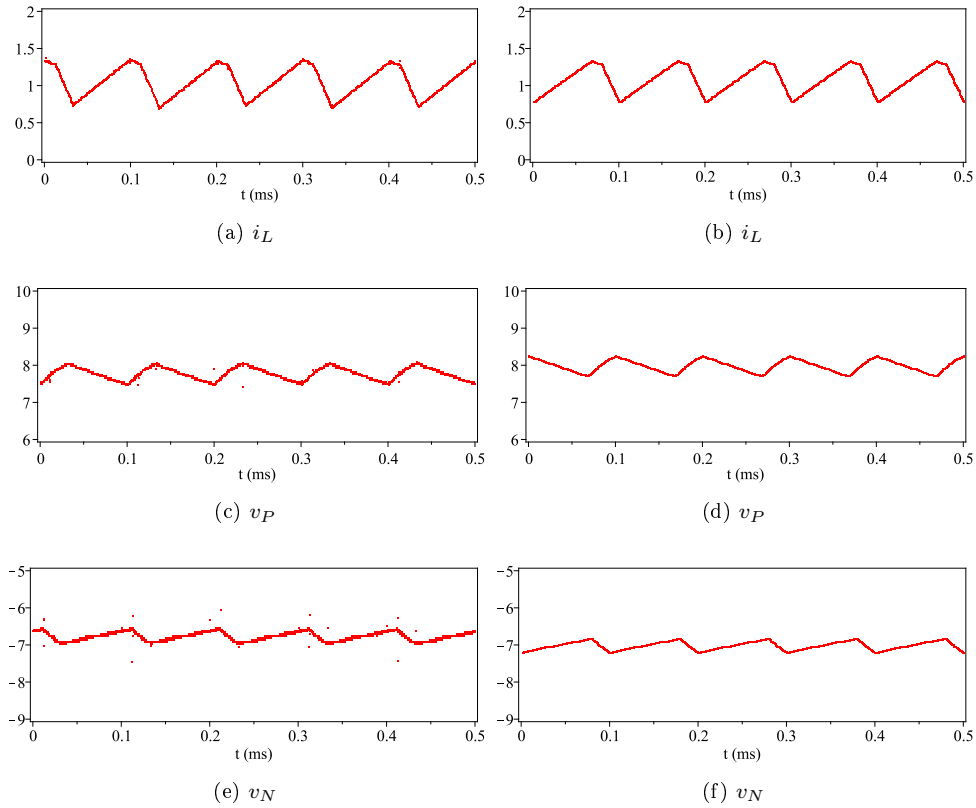
Figure 6.2. Waveforms of the inductor current and the capacitor voltages obtained experimentally (left) and by simulation (right). The varying parameters are $V_P = 8.0\,\mathrm{V}$ and $V_U = 1.5\,\mathrm{V}$.

Mode $\mathcal{M}_P$

When the positive reference voltage is set to $8.0\,\mathrm{V}$ (while $V_N = -7.0\,\mathrm{V}$), the normal mode of operation is $\mathcal{M}_P$. Figure 6.2 shows the evolution of the inductor current

(a) S_B and i_L (b) S_A and i_L
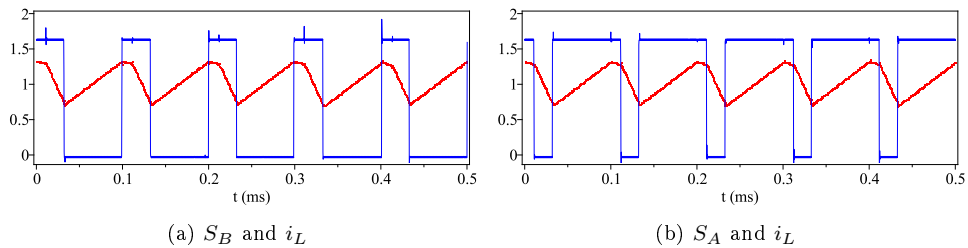
Figure 6.3. Waveforms of the inductor current and driven signals of S_B (a) and S_A (b) obtained in the prototype of SITITO converter. The parameters are in Fig. 6.2.

(a) i_L (b) i_L
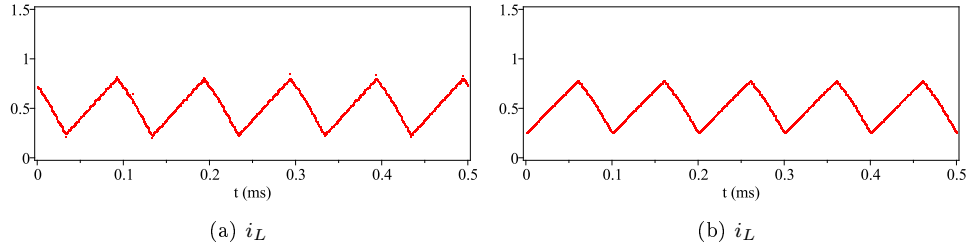
Figure 6.4. Evolution of the inductor current obtained experimentally (left) and with the PSIM simulator (right). The varying parameters are $V_P = 2.0\,\text{V}$ and $V_U = 1.5\,\text{V}$.

(a) S_A and i_L (b) S_B and i_L
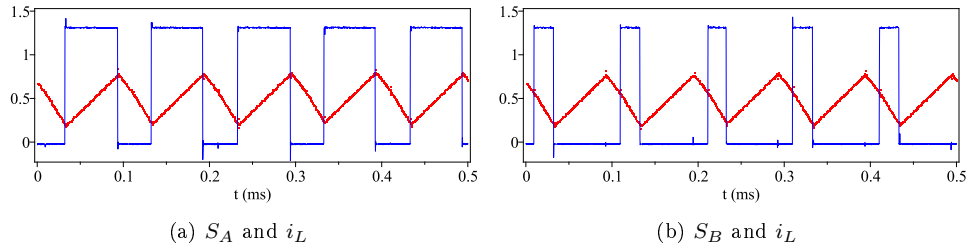
Figure 6.5. Evolution of the inductor current and the driven signals of S_A (left) and S_B (right). The parameters are in Fig. 6.4.

and capacitor voltages obtained experimentally (left) and with the PSIM simulator (right). As it can be observed, experimental measurements are in good agreement with expected results. Figure 6.3 shows the signals which drive the switches S_A (Fig. 6.3a) and S_B (Fig. 6.3b), whose edges force the switching instants of the MOSFET's. It has to be taken into account that the logic levels of these signals, which have been pondered in Fig. 6.3 for the sake of clarity, operates in an opposite way and have been inverted by intermediate drivers. Therefore, S_A is open or closed at low or high levels of its corresponding driven signal respectively whereas S_B is open or closed at high or low levels respectively.

Mode $\mathcal{M}_N$

Stable dynamical behavior has been also obtained when $V_P = 2.0\,\text{V}$ ($V_N = -7\,\text{V}$), so that the converter operates in the mode $\mathcal{M}_N$ (see Fig. 6.4). In this case (see Fig. 6.5), the switching of S_A becomes earlier than S_B and therefore, $d_A < d_B$.

6.2.2 Bifurcation analysis

In this section, preliminary experimental results of the nonlinear phenomena of the SITITO converter are presented. For the sake of clarity, a two-dimensional bifurcation
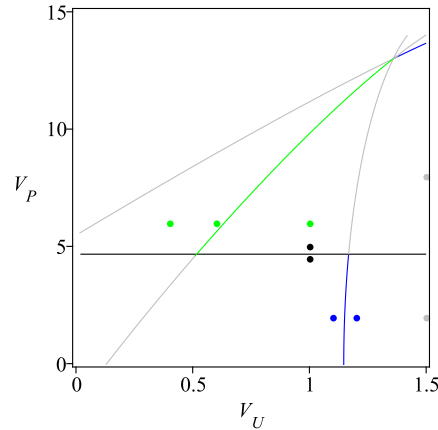
Figure 6.6. (a) Stability (green), ISL (blue) and MOC (black) codimension-one bifurcation curves in the parameter space $\{V_U, V_P\}$. The curves have been obtained by using the one-dimensional discrete-time model. The parameters are in Table 6.1.

diagram in the parameter space $\{V_U, V_P\}$ has been depicted in Fig. 6.6, in which the stability (green) and the Mode Operation Change (MOC) (black) and Intermediate Slope Limit (ISL) (blue) non-smooth bifurcation curves have been represented by using the one-dimensional map obtained in Chapter 4. Three nonlineal phenomena will be shown: period-doubling, MOC and ISL bifurcations by means of temporal plots of the inductor current. Notice that the specific parameters used in these representations have been marked in the Fig. 6.6 as blue (ISL), green (flip) and black (MOC) dots. In the diagrams obtained with the PSIM simulator and depicted in Fig. 6.7, the period doubling (Fig. 6.7a) and ISL (Fig. 6.7b) bifurcation can be appreciated.

Flip bifurcation

Two waveforms of the inductor current have been obtained (see Fig. 6.8) at the values $V_P = 6.0$ V and $V_U = 1.0$ V (Fig. 6.8a), $V_U = 0.6$ V (Fig. 6.8b) and $V_U = 0.4$ V (Fig. 6.8c) by means of experimental measurements. The normal dynamics represented in Fig. 6.7a becomes a period-two orbit after a flip bifurcation, as it can be appreciated in Fig. 6.8b. In the range of the parameters selected, as the value of V_U is decreased, the two-periodic orbit presents a non-smooth bifurcation and a four-periodic orbit appears, which becomes a chaotic attractor after another BC bifurcation. Due to the presence of noise, the dynamics in Fig. 6.8c cannot be clearly distinguished, which can correspond to a four-periodic orbit or a chaotic attractor. Anyway, a further decrease of the parameter V_U shows chaotic dynamics.

(a) $V_P = 6.0\,\text{V}$

(b) $V_P = 2.0\,\text{V}$

(c) $V_U = 1.0\,\text{V}$
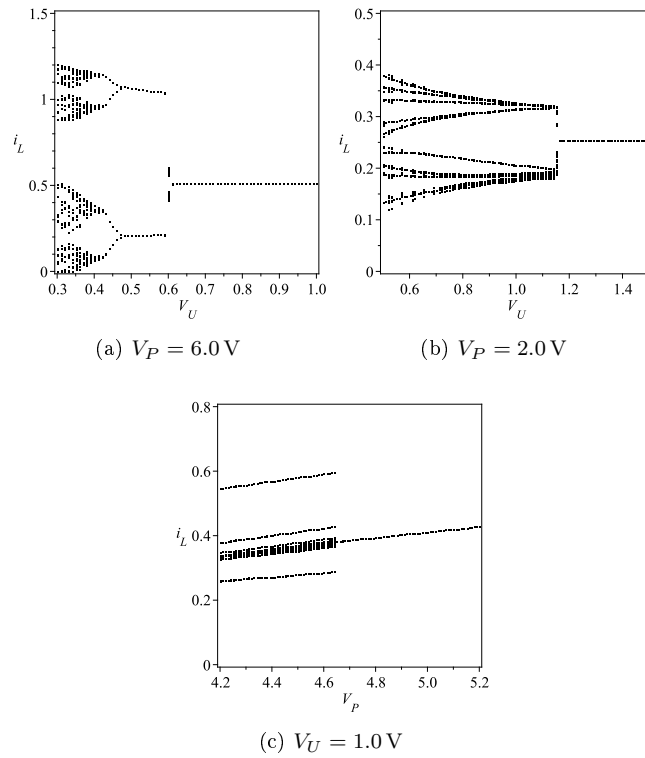
Figure 6.7. Bifurcation diagrams obtained with the PSIM simulator. The inductor current synchronized with the clock is the variable represented.

(a) $V_P = 6.0\,\text{V}$, $V_U = 1.0\,\text{V}$

(b) $V_P = 6.0\,\text{V}$, $V_U = 0.65\,\text{V}$

(c) $V_P = 6.0\,\text{V}$, $V_U = 0.40\,\text{V}$
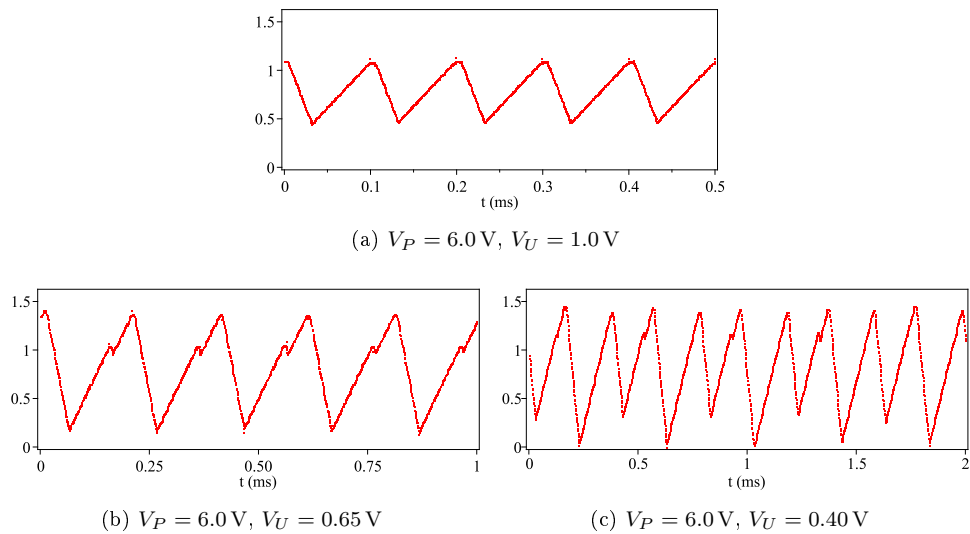
Figure 6.8. Experimental measurements of the waveform of the inductor current after a flip bifurcation has undergone.

(a) $V_P = 2.0\,\text{V}$, $V_U = 1.2\,\text{V}$ (b) $V_P = 2.0\,\text{V}$, $V_U = 1.1\,\text{V}$
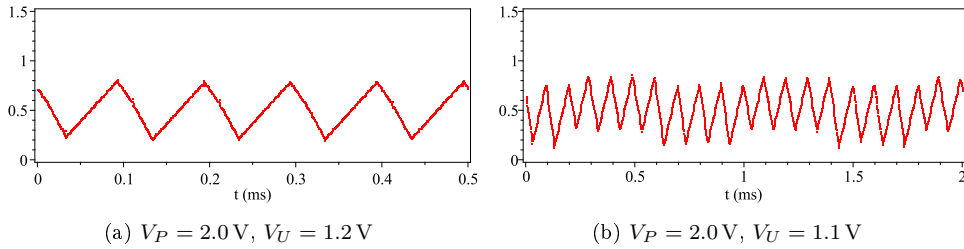
Figure 6.9. Evolution of the inductor current around a ISL non-smooth bifurcation.

(a) $V_P = 5.0\,\text{V}$, $V_U = 1.0\,\text{V}$ (b) $V_P = 4.5\,\text{V}$, $V_U = 1.0\,\text{V}$
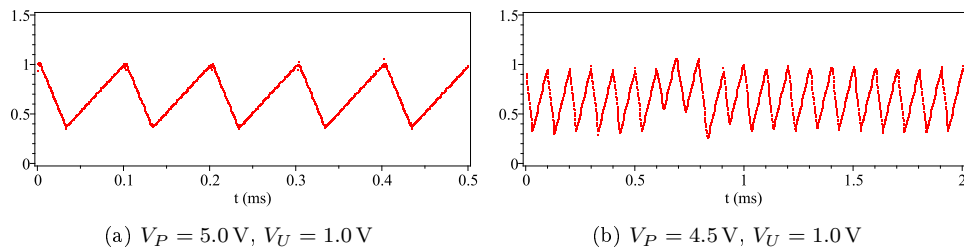
Figure 6.10. Evolution of the inductor current in the neighborhood of a MOC bifurcation.

ISL and MOC non-smooth bifurcations

ISL and MOC border-collision bifurcations can be seen in Fig. 6.9 and Fig. 6.10 respectively, where experimental waveforms of the inductor current have been obtained in both sides of the ISL and MOC bifurcations. Notice that the critical values of the parameters V_U and V_P are in agreement with the numerical results obtained with the one-dimensional map and the PSIM simulator (see Fig. 6.7b and Fig. 6.7c).

6.3 Interleaved Control

Let us now show some of the experimental measurements obtained in the same prototype but driven by the IC control. Similarly, the normal operation behavior and a preliminary bifurcation study are presented in this section. The value of parameters are given in Table 6.1, considering the indexes 1 and 2 equal to P and N respectively. The parameter ϕ_1 (notice that $\phi_2 = 1 - \phi_1$) is specified in each diagram.

6.3.1 Normal operation regime

Firstly, in order to compare the dynamical properties of both controls, the normal operation regime has been illustrated with a set of parameters equals to those used in the previous section. Figure 6.11 shows the evolution of the inductor current and the capacitor voltages obtained experimentally and by using the PSIM simulator.
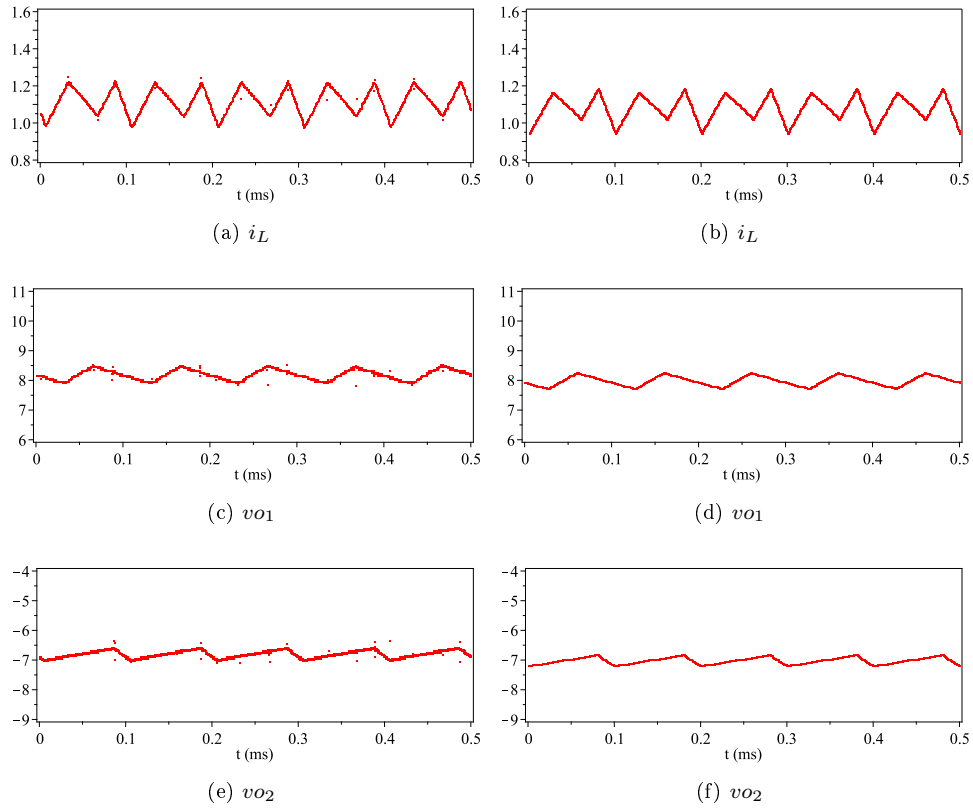
Figure 6.11. Waveforms of the inductor current and capacitor voltages obtained experimentally (left) and numerically with the PSIM simulator (right). The parameters are the same that in Fig. 6.2 and $\phi_1 = 0.60$.
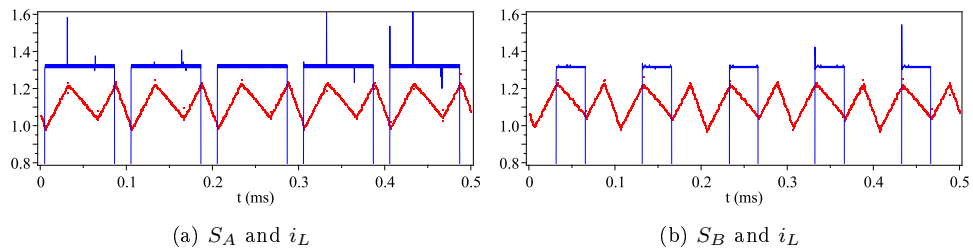
Figure 6.12. Waveforms of the inductor current and the driven signals of S_A (a) and S_B (b) obtained experimentally. The set of parameters corresponds to Fig. 6.11.

(a) Decreasing V_U (b) Increasing V_U
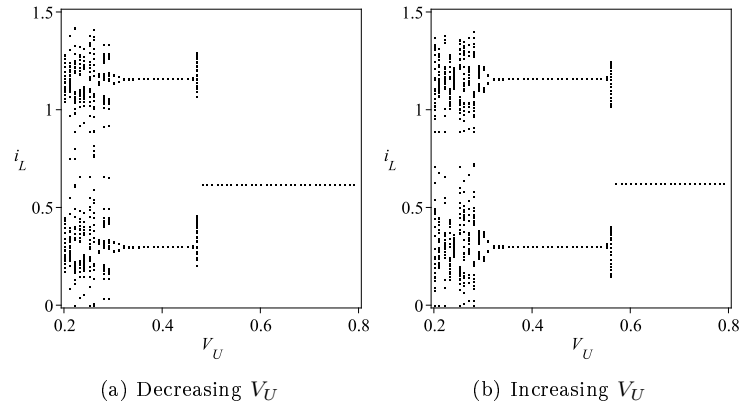
Figure 6.13. Bifurcation diagrams obtained with the PSIM simulator using V_U as the varying parameter. The parameters are in Table 6.1 except: $V_1 = 3.0\,\text{V}$, $V_2 = -15.0\,\text{V}$, $R_1 = 33\,\Omega$, $R_2 = 68\,\Omega$ and $\phi_1 = 0.45$.

Complementary, the driven signals of the switches have also been depicted in Fig. 6.12.

Notice that ϕ_1 has been set to 0.6. As it has been mentioned above, the first switching instant cannot be programmed before a minimum value due to computing time required in its estimation. However, the critical situation can be avoided, when possible, by increasing ϕ_1.

6.3.2   Bifurcation analysis

To conclude, some smooth and non-smooth bifurcations have been detected in the real system. Diagrams showing the dynamics around a flip bifurcation and the border-collision bifurcations related with the delay applied between both modulated signals are described bellow.

Flip bifurcation

In the range of parameters selected above, the normal operation regime does not present any flip bifurcation as the parameter V_U is varied. As it was concluded in Chapter 5, the flip bifurcation takes place in areas in which the parameters related with channels 1 and 2 are highly asymmetric. Therefore, the voltage references V_1 and V_2 have been set to $3.0\,\text{V}$ and $-15.0\,\text{V}$ respectively and the resistors $R_1 = 22\,\Omega$ and $R_2 = 33\,\Omega$ have been replaced by $R_1 = 33\,\Omega$ and $R_2 = 68\,\Omega$. In Fig. 6.13, two bifurcation diagrams have been depicted. The hysteresis phenomenon associated with the flip bifurcation explained in Section 5.3.3 can been observed in the figure. Two waveforms are depicted in Fig. 6.14, which illustrates one and two-periodic orbits at

(a) $V_U = 0.9\,\mathrm{V}$ (b) $V_U = 0.5\,\mathrm{V}$
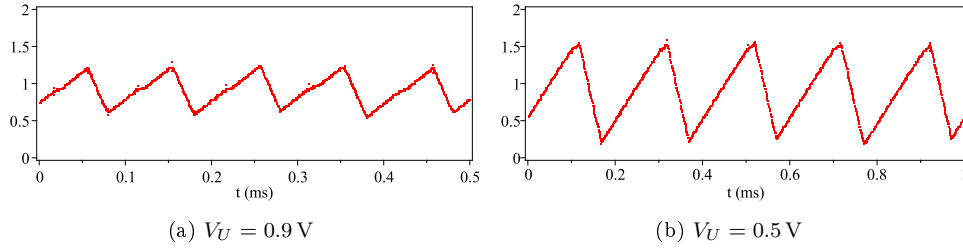
Figure 6.14. Waveforms of the inductor current obtained experimentally. The parameters are in Fig. 6.13.

(a)   (b) $\phi_1 = 0.55\,\mathrm{V}$.
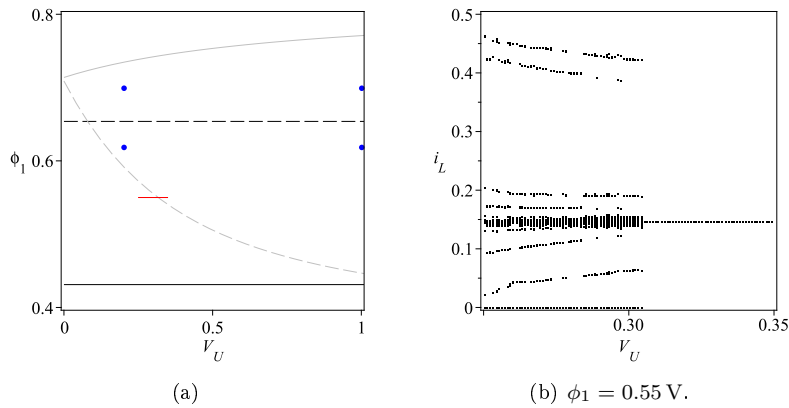
Figure 6.15. (a) Validity curves from (5.24) (black) and (5.25) (grey) for $N = 2$. Solid and dashed lines corresponds to the conditions for the phase intervals one and two respectively. (b) Bifurcation diagram using V_U as the varying parameter. The parameters are in Table 6.1 except $V_1 = 4.0\,\mathrm{V}$, $V_2 = -8.0\,\mathrm{V}$, $R_1 = 33\,\Omega$ and $R_2 = 68\,\Omega$.

the values of $V_U = 0.9\,\mathrm{V}$ (a) and $V_U = 0.5\,\mathrm{V}$ (b) respectively. Unfortunately, in the region of the parameter V_U in which both attractors coexist, the presence of noise in the system makes difficult the stabilization of both dynamics separately which, from time to time, flips between the two attractors.

Border-collision bifurcations

Let us now focus in the validity conditions of the discrete-time models proposed in Section 5.3.2. In the two-dimensional bifurcation diagram depicted in Fig. 6.15a in the parameter space $\{V_U, \phi_1\}$, four validity curves obtained with the five-dimensional map have been plotted under parameters in Table 6.1 and $V_1 = 4.0\,\mathrm{V}$, $V_2 = -8.0\,\mathrm{V}$, $R_1 = 33\,\Omega$ and $R_2 = 68\,\Omega$. As it was explained above, the interleaved control was considered with two kinds of boundaries due to the fact that each switching can only be produced in its own phase interval. The first anomaly occurs when the relative position of the peak references avoids one of the switchings (grey curves) whereas the

(a) $V_U = 0.35\,\mathrm{V}$

(b) $V_U = 0.25\,\mathrm{V}$

(c) $V_U = 0.35\,\mathrm{V}$

(d) $V_U = 0.25\,\mathrm{V}$
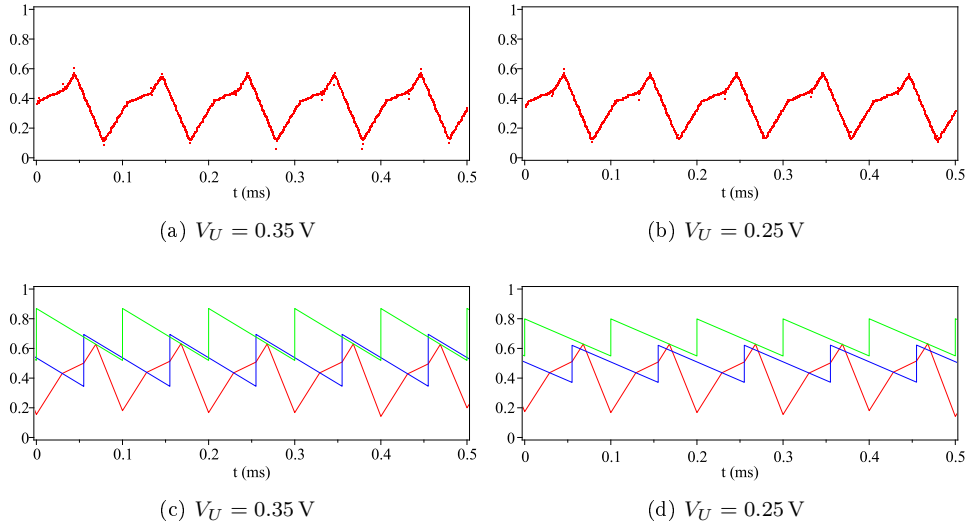
Figure 6.16. (a,b) Waveforms of the inductor current obtained experimentally. (c,d) Reconstructions of the experimental waveforms of the inductor current depicted in (a) and (b) respectively including the current peak references I_r^1 (blue) and I_r^2 (green) with data supplied by the micro-controller. The parameters are in Fig. 6.15 and $\phi_1 = 0.55$.

second case deals with two switchings produced in the same phase interval, so that would be $d_1 = 0$ or $d_2 = 0$ (black curves). Solid and dashed lines distinguishes the two conditions for the phases 1 and 2 respectively. The red line represents the varying range of the parameter V_U used in the bifurcation diagram shown in Fig. 6.15b and the blue dots correspond to the different set of parameters used in Figs. 6.17 and 6.18.

Notice that, in the first case, the normal operation regime undergoes a border-collision bifurcation when the second switching is skipped, with the control proposed in Chapter 5. Nevertheless, this non-smooth bifurcation can be easily avoided by a slightly different programme in control. The experimental results are shown in Figs. 6.16a and 6.16b. To facilitate the comprehension of this option, new plots obtained by means of data supplied by the micro-controller have been depicted in Figs. 6.16c and 6.16d to show the waveforms of the inductor current and the two peak reference currents. The reconstructions of these signals have been made using the periodically acquired values of the inductor current and capacitor voltages together with the predicted values for the duty cycles and the peak references. All this variables are obtained as auxiliary outputs of the micro-controller. Notice in Fig. 6.16d, that the switching of S_2 is permitted (the switching condition for S_1 is ignored), which avoids the border-collision provoked by the relative position between both current peak references. Actually, the new algorithm is simpler and requires less memory and computing time.

(a) $V_U = 1.0\,\text{V}$ and $\phi_1 = 0.62$

(b) $V_U = 1.0\,\text{V}$ and $\phi_1 = 0.7$

(c) $V_U = 1.0\,\text{V}$ and $\phi_1 = 0.62$

(d) $V_U = 1.0\,\text{V}$ and $\phi_1 = 0.7$
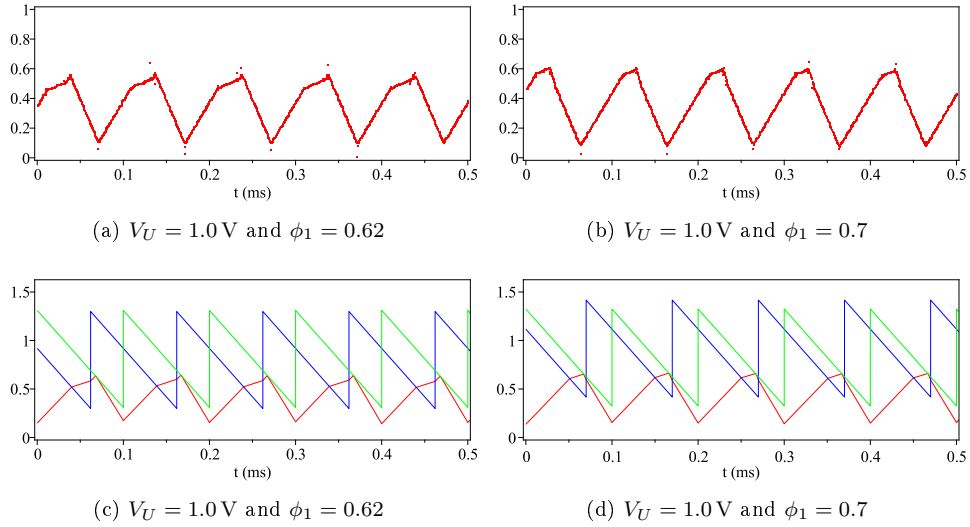
Figure 6.17. (a,b) Waveforms of the inductor current obtained experimentally showing a persistence scenario. (c,d) Reconstructions of the experimental waveforms of the inductor current plotted in (a) and (b) respectively and the current peak references I_r^1 (blue) and I_r^2 (green). The parameters are in Fig. 6.15.

Concerning the second case, Figs. 6.17 and 6.18 show the inductor current obtained experimentally at different values of V_U and ϕ_1, in the neighborhood of this non-smooth bifurcation. The dynamics observed in the diagrams of Figs. 6.17a and 6.17b correspond to an one-periodic orbit and therefore, the scenario given at the critical point is persistence. Notice in the reconstructed waveforms depicted in Fig. 6.17c that the one-periodic orbit at $V_U = 0.62\,\text{V}$ has the two switchings in different interval phases (normal regime) whereas in Fig. 6.17d both switchings are produced in the first interval. Conversely, in Fig. 6.18, a two-periodic orbit appears due to a non-smooth period-doubling bifurcation (see Fig. 6.18b). This two-periodic orbit links a sequence of different patterns per period of the modulating signal: the pattern of the normal operation and the two switchings in the first subinterval for the second period. A detailed analysis of this scenario, which requires to model the dynamics of the converter when both switchings are produced in the first interval phase, will be realized in future works.

6.4 Conclusions

Several experimental measurements realized in a prototype of a SITITO converter regulated by the two controls proposed in this dissertation (SPC and IC) have been presented. The ranges of parameters have been chosen according to the limitations of the system, in order to show several dynamical behaviors produced in the experiments.

(a) $V_U = 0.2\,\mathrm{V}$ and $\phi_1 = 0.62$

(b) $V_U = 0.2\,\mathrm{V}$ and $\phi_1 = 0.7$
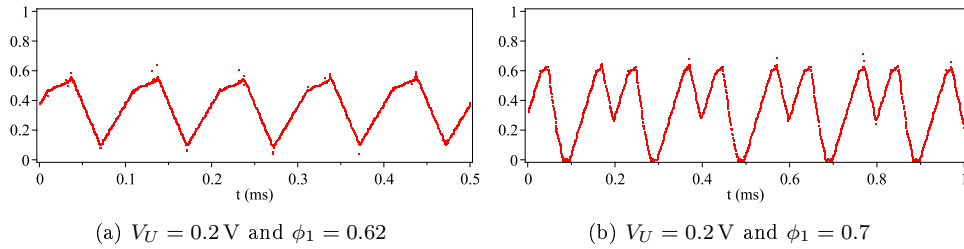
Figure 6.18. Waveforms of the inductor current obtained experimentally showing non-smooth period doubling scenario. The parameters are in Fig. 6.15.

Concerning the first strategy of control, the main bifurcations analyzed in the Chapter 4 have also been detected in the physical system at the critical values predicted. Nevertheless, bifurcations involving the parameters of the integral terms have been postponed due to the need of a previous dynamical study of the system with the simplified integral control programmed.

More difficulties have arisen in the IC control implementation. The lower limit of the duty cycle forced by the micro-controller implies a significant reduction in the possible range of the parameters. It has to be remarked that this limitation not only affects to the one-periodic orbit but even more to higher periodic orbits, quasiperiodicity and chaos. Nevertheless, when the normal operation regime is available, this dynamics is stable in a wide range of parameters.

It has been proved in this Chapter that one of the border-collision bifurcations can be avoided under a simple modification of the algorithm of control. This fact leads us to consider in the future others variant of controls, some of them simpler, indeed. The use of these algorithms could imply the increasing of the frequency of the modulating signal.

Chapter 7

Conclusions and future works

Static and dynamics properties of a Single-Inductor Multiple-Input Multiple-Output (SIMIMO) dc-dc converter have been determined by means of averaged and discrete-time models. The results that have been obtained prove the ability of the converter to regulate several outputs with different polarities when the parameters are properly selected. The analysis include not only the determination of instability conditions, but also the limit or boundary conditions and the different dynamics that arise beyond them. Experimental measurements have also been added to prove the viability of these converters and dynamics properties in a specific range of parameters.

In order to reach our objective, different models have been developed with a tunable degree of accuracy. Firstly, the usefulness of the averaged models has been validated. Besides the characterization of the equilibrium situation and the duty cycle of each channel, these models provide information of the stability related with the slow scale dynamics. However, the averaged models are also known to be unable of detecting phenomena related with the fast scale dynamics, in which mainly the ripple of the inductor current is involved. This restriction covers not only the prediction of instability, but also the detection of some of the non-smooth bifurcations, which are conditioned by the evolution of the inductor current during a period. This leads to the requirement of using discrete-time models to deal with these dynamics unpredicted by averaged models.

Discrete-time models with different number of state variables have been proposed to deal with the dynamics of the dc-dc converter driven by two different strategies of control: Single Phase Control (SPC) and Interleaved Control (IC), which have been

capable of regulating a Single-Inductor Two-Input Two-Output (SITITO) converter. The one-dimensional model is obtained when only the evolution of the inductor current is taken into consideration. In both SPC or IC, the analysis of these models has permitted to obtain simple analytical expressions to characterize the stability and the non-smoothness of the system. Higher dimensional maps have also been obtained to improve the accuracy in these predictions. In the IC control, numerical results have revealed a relevant deviation in the prediction of the Flip bifurcation.

Besides the analysis of both controls, another contribution given in this dissertation has dealt with the dynamical study of a three-piece piecewise-linear (PWL) map. The discrete analysis of both controls has shown that the one-dimensional PWL map which describes the evolution of the inductor current is characterized by having three pieces, in case of the SPC, or three or four pieces for the alternative IC. Therefore, the study of a normalized one-dimensional PWL map has helped us to account for the feasible scenarios in which one and two-periodic orbits are involved.

7.1 Differences in the operation of the converter under both strategies of control

To sum up, we will present a list of relevant differences in the operation of the controls SPC and IC. Due to the fact that the control SPC has not been generalized to several outputs, only dynamics of SITITO dc-dc converters are evaluated.

- Concerning the main mode of operation, in the SPC the two capacitors are simultaneously loaded in the last part of the OFF interval, whereas in the IC, only one capacitor is loaded in the corresponding phase. As it was appreciated in the experimental measurements, this fact implies that the possible low saturation of the duty cycle, given when the duty cycles reach the 0 value, is more likely in the IC control due to the fact that more time is required to load both capacitors. On the other hand, high saturation of the duty cycles involving one-periodic orbits cannot be given in any of the controls.

- We have found that during the transient multiple patterns of switching are possible. Unlike the one-dimensional model for SPC that takes into consideration all feasible configurations, the method used in the generalization in IC control limits the number of configurations that the model account for. Due to this fact, the number of validity conditions is higher in IC regarding SPC.

- Averaged models have been proved to be equivalent in both controls due to the fact that the evolution of the inductor current is not taken into consideration in the models.

- The one-dimensional discrete-time analysis has revealed that the instability of the SITITO converter driven by SPC can only be given when the eigenvalue

becomes -1, thus producing a flip bifurcation. Otherwise, in case of the IC, the instability can also appear when the eigenvalue becomes $+1$. Nevertheless, it should be remarked that, despite this increment in the unstable conditions in the IC, the flip bifurcation appears only in odd regions of parameters.

- Another important difference deals with the deviation in the predictions of the flip bifurcation. It has been shown that the converter driven by the IC is more sensible to the variation of ripples of the capacitor voltages. Hence, an increase in the feedback gains or a reduction in the time constants of the PI terms implies a greater deviation in the critical value predicted by the one-dimensional model.

7.2 Proposals of future works

Some future proposals are listed below:

- Concerning the characterization of the non-smooth phenomena in a three-piece piecewise-linear map, a further study could be directed to extend the analysis to the complete range of parameters. Moreover, our study has been restricted to the existence and stability of one and two-periodic orbits and, therefore, a complete description of the scenarios involving higher periodic orbits could also be of interest.

- It has been shown that averaged models fail in the prediction of some smooth bifurcations. More complete averaged models, which include information of the evolution of the inductor current, could be developed in order to detect the unpredicted Neimark-Sacker bifurcations.

- It has been observed that the experimental system has important limitations due to the presence of noise and hence, a significant reduction in the noise level should be achieved in order to increase the range of parameters available. Once having reduced it, the data acquisition system that is added to the control circuit could be reprogrammed to obtain periodic measurements of the state variables so that it would be capable of representing experimental bifurcation diagrams.

- Due to the fact that the algorithm of control can be reprogrammed easily, simpler digital controls, which reduces significantly the computing time in the prediction of the switching instants, can be chosen to regulate the converter. This improvement could permit an increase in the frequency of the modulated signal.

Appendix A

Five-dimensional map of the SITITO converter with SPC

In this appendix, the five-dimensional discrete-time model which describes the dynamics of a SITITO converter regulated by the SPC control is developed. Due to the symmetry between $\mathcal{M}_P$ and $\mathcal{M}_N$, only the mode of operation $\mathcal{M}_P$ will be explained in detail.

Let us define the following map:

$$f(\mathbf{x}) = \mathbf{x}_{n+1} \tag{A.1}$$

where $\mathbf{x}_n = [i, vp, vn, \sigma p, \sigma n]^T$ and $\mathbf{x}_{n+1} = [i_{n+1}, vp_{n+1}, vn_{n+1}, \sigma p_{n+1}, \sigma n_{n+1}]^T$.

Notice that the subindex n has been eliminated from the discrete state variable $\mathbf{x}$ to make the reading clearer.

Similarly to the definition of the one-dimensional map, (A.1) can be divided into the submappings:

$$f(i, vp, vn, \sigma p, \sigma n, \phi) = \begin{cases} f_1(i, vp, vn, \sigma p, \sigma n, \phi) & \text{if } H_0(vp, vn, \phi) > 0, \\ f_2(i, vp, vn, \sigma p, \sigma n, \phi) & \text{if } H_0(vp, vn, \phi) < 0, \end{cases}$$

where $f : \mathbb{R}^5 \times \mathbb{R}^{19} \mapsto \mathbb{R}^5$ and the surface H_0 is given by

$$H_0(vp, vn, \phi) = \frac{vp}{R_P} - \frac{vn}{R_N},$$

and ϕ refers to the set of parameters

$$\phi = \{V_{IN}, r_L, L, V_P, V_N, R_P, R_N, V_U, V_L, T, C_P, C_N, r_S, g_{PA}, g_{PB}, g_{NA}, g_{NB}, \tau_P, \tau_N\}.$$

For the sake of simplicity, g_{FA} and g_{FB} have been considered 0 in these analysis.

In the next section, expressions for i_{n+1}, vp_{n+1}, vn_{n+1}, σp_{n+1} and σn_{n+1} are presented for both submappings.

A.1   Mode of operations $\mathcal{M}_P$, $\mathcal{M}_{SP}$ and $\mathcal{M}_0$

It is important the remark that the sequence of topologies in the mode $\mathcal{M}_P$ is $\mathcal{T}_1 \rightarrow \mathcal{T}_2 \rightarrow \mathcal{T}_4$, whereas in $\mathcal{M}_{SP}$ and $\mathcal{M}_0$ the sequences correspond to $\mathcal{T}_1 \rightarrow \mathcal{T}_2$ and $\mathcal{T}_1$ respectively.

Obtaining i_L

	S_A	S_B	Δi	
$\mathcal{T}_1$	ON	ON	$\Delta \mathtt{i}_1$	$\dfrac{V_{IN} - r_L I_Q}{L}T$
$\mathcal{T}_2$	ON	OFF	$\Delta \mathtt{i}_2$	$\dfrac{V_{IN} - vp - r_L I_Q}{L}T$
$\mathcal{T}_3$	OFF	ON	$\Delta \mathtt{i}_3$	$\dfrac{vn - r_L I_Q}{L}T$
$\mathcal{T}_4$	OFF	OFF	$\Delta \mathtt{i}_4$	$\dfrac{vn - vp - r_L I_Q}{L}T$

Table A.1. Definition of the increment currents of the SITITO converter in CCM.

The assumptions considered in the development of the one-dimensional map are also valid here. Therefore, according to (4.30),(4.32),(4.33) and (4.34), i_{n+1} can be expressed as

$$i_{n+1} = \begin{cases} i + \Delta \mathtt{i}_1 & \text{if } \mathbf{x} \in S_A, \\ i + \Delta \mathtt{i}_1 d_B + \Delta \mathtt{i}_2 (1 - d_B) & \text{if } \mathbf{x} \in S_B, \\ i + \Delta \mathtt{i}_1 d_B + \Delta \mathtt{i}_2 d_{AB} + \Delta \mathtt{i}_4 (1 - d_A) & \text{if } \mathbf{x} \in S_C. \end{cases} \quad (A.2)$$

Nevertheless, there exist some differences. Firstly, the increment currents $\{\Delta \mathtt{i}_j, \ j = 1..4\}$, which are summarized in Table A.1, depend on the state variables vp and vn. Moreover, $d_{AB} = d_A - d_B$ is not considered as constant value and the duty cycle d_A is approached similarly to d_B. In addition, both duty cycles are found using the

complete expressions for the peak references. Therefore, according to (4.35) and (4.3), the duty cycle d_B is given by

$$d_B = \frac{(V_U + g_{PB}(V_P - vp - \sigma p) + g_{NB}(vn - V_N + \sigma n))/r_S - i}{\Delta \mathtt{i}_1 - \Delta \mathtt{ir}}.$$

Similarly, taking into account the evolution of inductor current during $\mathcal{T}_1$ and $\mathcal{T}_2$, from (4.39) and (4.2) d_A can be expressed as

$$d_A = \frac{(V_U + g_{PA}(V_P - vp - \sigma p) + g_{NA}(vn - V_N + \sigma n))/r_S - (i + (\Delta \mathtt{i}_1 - \Delta \mathtt{i}_2)d_B)}{\Delta \mathtt{i}_2 - \Delta \mathtt{ir}}.$$

Obtaining v_P

According to (4.9), the evolution of the positive voltage during the topologies $\mathcal{T}_1$ is described by the state equation

$$\frac{\mathrm{d}v_P}{\mathtt{dt}} = \frac{-1}{R_P C_P} v_P, \tag{A.3}$$

whereas in the topology $\mathcal{T}_2$ and $\mathcal{T}_4$, the expression is given by

$$\frac{\mathrm{d}v_P}{\mathtt{dt}} = \frac{-1}{R_P C_P} v_P + \frac{i_L}{C_P}.$$

Therefore, it can be considered that the evolution of the capacitor voltage has two contributions: the discharge of the capacitor through the resistor, which acts during the entire period, and the charge acting only during $\mathcal{T}_2$ and $\mathcal{T}_4$. Considering that these two contributions will be approached separately, it can be define the following approached function $\widehat{v_P}(t)$ as follows:

$$v_P(t) \approx \widehat{v_P}(t) = vp_d(t) + vp_c(t).$$

$vp_d(t)$ gives the information about the discharge and its evolution can be approached by the first element of the Taylor series of (A.3). Therefore,

$$vp_d(t) = vp - \frac{vp}{C_P R_P} t,$$

where vp corresponds to the capacitor voltage at the beginning of the period ($vp = v_P(0)$).

In order to estimate the second contribution, we assume the following approximation of the evolution of the inductor current, $\widehat{i_L}(t)$, in the mode $\mathcal{M}_P$, as it has been developed

in Chapter 4:

$$i_L(t) \approx \widehat{i_L}(t) = \begin{cases} i + \Delta\mathtt{i}_1\dfrac{t}{T} & \text{if } t \leq d_B T, \\ i' + \Delta\mathtt{i}_2\left(\dfrac{t}{T} - d_B\right) & \text{if } d_B T \leq t < d_A T, \\ i'' + \Delta\mathtt{i}_4\left(\dfrac{t}{T} - d_A\right) & \text{if } t > d_A T, \end{cases} \qquad \text{(A.4)}$$

where i, i', and i'' correspond to the initial conditions of the inductor current in the different topologies $\mathcal{T}_1$, $\mathcal{T}_2$ and $\mathcal{T}_4$ respectively. Defining $d_1 = d_B$, $d_2 = d_A$, $\Delta\mathtt{i} = \Delta\mathtt{i}_2$ and $\Delta d = d_{AB}$, the inial conditions are given by

$$i = i_L(0) \quad i' = i + \Delta\mathtt{i}_1 d_1 \quad i'' = i' + \Delta\mathtt{i}\Delta d.$$

During the topology $\mathcal{T}_1$, there is no charge in the capacitor. Conversely, during $\mathcal{T}_2$ the charge of the capacitor, which is proportional to the area of the inductor current, can be approached by

$$\int_{d_B T}^{t} \frac{i_L}{C_P}\mathtt{dt} \approx \frac{T}{C_P}\left(i'\left(\frac{t}{T} - d_B\right) + \frac{\Delta\mathtt{i}_2}{2}\left(\frac{t}{T} - d_B\right)^2\right),$$

whereas during the last topology $\mathcal{T}_4$, the approach is given by

$$\int_{d_A T}^{t} \frac{i_L}{C_P}\mathtt{dt} \approx \frac{T}{C_P}\left(\delta\mathtt{vp}_1 d_{AB} + i''\left(\frac{t}{T} - d_A\right) + \frac{\Delta\mathtt{i}_4}{2}\left(\frac{t}{T} - d_A\right)^2\right),$$

where the function $\delta\mathtt{vp}_1$, together with all the auxiliary functions used in this chapter, is defined in Table A.2. Finally, the function $vp_c(t)$ is given by the function

$$vp_c(t) = \frac{T}{C_P}\begin{cases} 0 & \text{if } t \leq d_B T, \\ i'\left(\dfrac{t}{T} - d_B\right) + \dfrac{\Delta\mathtt{i}_2}{2}\left(\dfrac{t}{T} - d_B\right)^2 & \text{if } d_B T < t < d_A T, \\ \delta\mathtt{vp}_1 d_{AB} + i''\left(\dfrac{t}{T} - d_A\right) + \dfrac{\Delta\mathtt{i}_4}{2}\left(\dfrac{t}{T} - d_A\right)^2 & \text{if } t > d_A T. \end{cases}$$

Then, applying $vp_{n+1} = \widehat{v_P}(T)$, we obtain

$$vp_{n+1} = vp_d(T) + vp_c(T) = vp + \Delta\mathtt{vp} + \delta\mathtt{vp}_1 d_{AB} + \delta\mathtt{vp}_2\left(1 - d_A\right).$$

Easier analysis can be done so as to find expressions of vp_{n+1} for the remainder modes of operation $\mathcal{M}_{SP}$ and $\mathcal{M}_0$. It can be proved easily that

$$vp_{n+1} = \begin{cases} vp + \Delta\mathtt{vp} & \text{if } \mathbf{x} \in S_A, \\ vp + \Delta\mathtt{vp} + \delta\mathtt{vp}_1\left(1 - d_B\right) & \text{if } \mathbf{x} \in S_B, \\ vp + \Delta\mathtt{vp} + \delta\mathtt{vp}_1 d_{AB} + \delta\mathtt{vp}_2\left(1 - d_A\right) & \text{if } \mathbf{x} \in S_C. \end{cases} \qquad \text{(A.5)}$$

$\Delta\mathtt{vp}$	$\dfrac{T}{C_P}\left(-\dfrac{vp}{R_P}\right)$	$\Delta\mathtt{vn}$	$\dfrac{T}{C_N}\left(-\dfrac{vn}{R_N}\right)$
$\delta\mathtt{vp}_1$	$\dfrac{T}{C_P}\left(i' + \dfrac{\Delta\mathtt{i}\Delta d}{2}\right)$	$\delta\mathtt{vn}_1$	$\dfrac{T}{C_P}\left(i' + \dfrac{\Delta\mathtt{i}\Delta d}{2}\right)$
$\delta\mathtt{vp}_2$	$\dfrac{T}{C_P}\left(i'' + \dfrac{\Delta\mathtt{i}_4(1-d_2)}{2}\right)$	$\delta\mathtt{vn}_2$	$\dfrac{T}{C_N}\left(i'' + \dfrac{\Delta\mathtt{i}_4(1-d_2)}{2}\right)$
$\delta\mathtt{vp}_3$	$\dfrac{T}{2C_P}\left(i' + \dfrac{\Delta\mathtt{i}\Delta d}{3}\right)$	$\delta\mathtt{vn}_3$	$\dfrac{T}{2C_N}\left(i' + \dfrac{\Delta\mathtt{i}\Delta d}{3}\right)$
$\delta\mathtt{vn}_4$	$\dfrac{T}{2C_P}\left(i'' + \dfrac{\Delta\mathtt{i}_4(1-d_2)}{3}\right)$	$\delta\mathtt{vn}_4$	$\dfrac{T}{2C_N}\left(i'' + \dfrac{\Delta\mathtt{i}_4(1-d_2)}{3}\right)$
$\delta\mathtt{vp}_5$	$\delta\mathtt{vp}_3\Delta d + \delta\mathtt{vp}_1(1-d_2)$	$\delta\mathtt{vn}_5$	$\delta\mathtt{vn}_3\Delta d + \delta\mathtt{vn}_1(1-d_2)$

Table A.2. Definition of the auxiliary functions. d_1, d_2, $\Delta\mathtt{i}$ and Δd correspond to d_B, d_A, $\Delta\mathtt{i}_2$ and d_{AB} respectively in the modes $\mathcal{M}_P$ and $\mathcal{M}_{SP}$ and d_A, d_B, $\Delta\mathtt{i}_3$ and $-d_{AB}$ in $\mathcal{M}_N$ and $\mathcal{M}_{SN}$.

Obtaining v_N

The evolution of the negative capacitor voltage can be obtained similarly. Taking into account the differential equations of $v_N(t)$ in the topologies $\mathcal{T}_1$ and $\mathcal{T}_2$ and $\mathcal{T}_4$ and that there exists charge in the negative capacitor only during the topology $\mathcal{T}_4$, it is easy to prove that

$$vn_{n+1} = \begin{cases} vn + \Delta\mathtt{vn} & \text{if } \mathbf{x} \in T_A, \\ vn + \Delta\mathtt{vn} & \text{if } \mathbf{x} \in T_B, \\ vn + \Delta\mathtt{vn} - \delta\mathtt{vn}_2\,(1-d_A) & \text{if } \mathbf{x} \in T_C. \end{cases} \tag{A.6}$$

Obtaining σp and σn

From (4.4) and (4.5), the state equations of the integral terms are given by

$$\frac{\mathrm{d}\sigma_P}{\mathrm{dt}} = \frac{1}{\tau_P}\left(v_P(t) - V_P\right) \quad \text{and} \quad \frac{\mathrm{d}\sigma_N}{\mathrm{dt}} = \frac{1}{\tau_N}\left(v_N(t) - V_N\right).$$

Considering the approached evolution of the positive capacitor voltage $\widehat{v_P}(t)$ found above, $\sigma_P(t)$ can be simplified as

$$\widehat{\sigma p}(t) = \frac{1}{\tau_P}\int_{-\infty}^{t}(\widehat{v_P}(t) - V_P)\mathrm{dt} = \sigma p + \frac{1}{\tau_P}\int_{0}^{t}(\widehat{v_P}(t) - V_P)\mathrm{dt}.$$

Therefore, σp_{n+1} can be expressed as follows

$$\sigma p_{n+1} = \widehat{\sigma p}(T) = \sigma p + \frac{1}{\tau_P}\left(\int_{0}^{T} vp_d(t)\mathrm{dt} + \int_{0}^{T} vp_c(t)\mathrm{dt} - V_P T\right),$$

where

$$\int_0^T vp_d(t)\mathtt{dt} = \left(vp + \frac{\Delta\mathtt{vp}}{2}T\right)T,$$

$$\int_0^T vp_c(t)\mathtt{dt} = \int_{d_B T}^{d_A T} vp_c(t)\mathtt{dt} + \int_{d_A T}^T vp_c(t)\mathtt{dt}.$$

Taking into consideration the expressions of the inductor current in the different intervals, the solutions of the integrals are given by and

$$\int_{d_B T}^{d_A T} vp_c(t)\mathtt{dt} = \delta\mathtt{vp}_3 d_{AB}^2 T$$

and

$$\int_{d_A T}^T vp_c(t)\mathtt{dt} = \delta\mathtt{vp}_1 d_{AB}(1 - d_A)T + \delta\mathtt{vp}_4(1 - d_A)^2 T.$$

Then, vp_{n+1} is given by

$$\sigma p_{n+1} = \sigma p + \frac{T}{\tau_P}\left(vp + \frac{\Delta\mathtt{vp}}{2} + \delta\mathtt{vp}_5 d_{AB} + \delta\mathtt{vp}_4(1 - d_A)^2 - V_P\right).$$

Finally, the complete expressions for σp_{n+1} and σn_{n+1} in all the modes of operations are given by

$$\sigma p_{n+1} = \begin{cases} \sigma p + \dfrac{T}{\tau_P}\left(vp + \dfrac{\Delta\mathtt{vp}}{2} - V_P\right) & \text{if } \mathbf{x} \in S_A, \\[2ex] \sigma p + \dfrac{T}{\tau_P}\left(vp + \dfrac{\Delta\mathtt{vp}}{2} + \delta\mathtt{vp}_3(1 - d_B)^2 - V_P\right) & \text{if } \mathbf{x} \in S_B, \\[2ex] \sigma p + \dfrac{T}{\tau_P}\left(vp + \dfrac{\Delta\mathtt{vp}}{2} + \delta\mathtt{vp}_5 d_{AB} + \delta\mathtt{vp}_4(1 - d_A)^2 - V_P\right) & \text{if } \mathbf{x} \in S_C, \end{cases}$$

(A.7)

and

$$\sigma n_{n+1} = \begin{cases} \sigma n + \dfrac{T}{\tau_N}\left(vn + \dfrac{\Delta\mathtt{vn}}{2} - V_N\right) & \text{if } \mathbf{x} \in T_A, \\[2ex] \sigma n + \dfrac{T}{\tau_N}\left(vn + \dfrac{\Delta\mathtt{vn}}{2} - V_N\right) & \text{if } \mathbf{x} \in T_B, \\[2ex] \sigma n + \dfrac{T}{\tau_N}\left(vn + \dfrac{\Delta\mathtt{vn}}{2} - \delta\mathtt{vn}_4(1 - d_A)^2 - V_N\right) & \text{if } \mathbf{x} \in T_C. \end{cases}$$

(A.8)

A.2   Functions f_1 and f_2

Let us now provide the complete expressions for the submappings f_1 and f_2, which can be obtained directly from (A.2), (A.5), (A.6), (A.7) and (A.8). Considering the

the following redefinition of f_1:

$$f_1(i, vp, vn, \sigma p, \sigma n, \phi) = \begin{cases} F_A(i, vp, vn, \sigma p, \sigma n, \phi) & \text{if } \mathbf{x} \in S_A, \\ F_B(i, vp, vn, \sigma p, \sigma n, \phi) & \text{if } \mathbf{x} \in S_B, \\ F_C(i, vp, vn, \sigma p, \sigma n, \phi) & \text{if } \mathbf{x} \in S_C. \end{cases}$$

where the submappings $\mathbf{F}_A$, $\mathbf{F}_B$ and $\mathbf{F}_C$ are defined as

$$\mathbf{F}_A(\mathbf{x}) = \begin{bmatrix} i + \Delta\mathbf{i}_1 \\[2mm] vp + \Delta\mathbf{vp} \\[2mm] vn + \Delta\mathbf{vn} \\[2mm] \sigma p + \dfrac{T}{\tau_P}\left(vp + \dfrac{\Delta\mathbf{vp}}{2} - V_P\right) \\[2mm] \sigma n + \dfrac{T}{\tau_N}\left(vn + \dfrac{\Delta\mathbf{vn}}{2} - V_N\right) \end{bmatrix},$$

$$\mathbf{F}_B(\mathbf{x}) = \begin{bmatrix} i + \Delta\mathbf{i}_1 d_B + \Delta\mathbf{i}_2(1 - d_B) \\[2mm] vp + \Delta\mathbf{vp} + \delta\mathbf{vp}_1(1 - d_B) \\[2mm] vn + \Delta\mathbf{vn} \\[2mm] \sigma p + \dfrac{T}{\tau_P}\left(vp + \dfrac{\Delta\mathbf{vp}}{2} + \delta\mathbf{vp}_3(1 - d_B)^2 - V_P\right) \\[2mm] \sigma n + \dfrac{T}{\tau_N}\left(vn + \dfrac{\Delta\mathbf{vn}}{2} - V_N\right) \end{bmatrix},$$

$$\mathbf{F}_C(\mathbf{x}) = \begin{bmatrix} i + \Delta\mathbf{i}_1 d_B + \Delta\mathbf{i}_2 d_{AB} + \Delta\mathbf{i}_4(1 - d_A) \\[2mm] vp + \Delta\mathbf{vp} + \delta\mathbf{vp}_1 d_{AB} + \delta\mathbf{vp}_2(1 - d_A) \\[2mm] vn + \Delta\mathbf{vn} - \delta\mathbf{vn}_2(1 - d_A) \\[2mm] \sigma p + \dfrac{T}{\tau_P}\left(vp + \dfrac{\Delta\mathbf{vp}}{2} + \delta\mathbf{vp}_5 d_{AB} + \delta\mathbf{vp}_4(1 - d_A)^2 - V_P\right) \\[2mm] \sigma n + \dfrac{T}{\tau_N}\left(vn + \dfrac{\Delta\mathbf{vn}}{2} - \delta\mathbf{vn}_4(1 - d_A)^2 - V_N\right) \end{bmatrix}.$$

Similarly, the five-dimensional submapping f_2 is described bellow. The expressions can be obtained easily taking into account that the sequence in the mode $\mathcal{M}_N$ is

$\mathcal{T}_1 \to \mathcal{T}_3 \to \mathcal{T}_4$, whereas in $\mathcal{M}_{NP}$, the sequence corresponds to $\mathcal{T}_1 \to \mathcal{T}_3$. Let us redefine the submapping:

$$f_2(i, vp, vn, \sigma p, \sigma n, \phi) = \begin{cases} G_A(i, vp, vn, \sigma p, \sigma n, \phi) & \text{if } \mathbf{x} \in T_A, \\ G_B(i, vp, vn, \sigma p, \sigma n, \phi) & \text{if } \mathbf{x} \in T_B, \\ G_C(i, vp, vn, \sigma p, \sigma n, \phi) & \text{if } \mathbf{x} \in T_C, \end{cases}$$

where the functions $\mathbf{G}_A$, $\mathbf{G}_B$ and $\mathbf{G}_C$ are also redefined as

$$\mathbf{G}_A(\mathbf{x}) = \mathbf{F}_A(\mathbf{x}),$$

$$\mathbf{G}_B(\mathbf{x}) = \begin{bmatrix} i + \Delta\mathtt{i}_1 d_A + \Delta\mathtt{i}_3 (1 - d_A) \\[2mm] vp + \Delta\mathtt{vp} \\[2mm] vn + \Delta\mathtt{vn} - \delta\mathtt{vn}_1(1 - d_A) \\[2mm] \sigma p + \dfrac{T}{\tau_P}\left(vp + \dfrac{\Delta\mathtt{vp}}{2} - V_P\right) \\[2mm] \sigma n + \dfrac{T}{\tau_N}\left(vn + \dfrac{\Delta\mathtt{vn}}{2} + \delta\mathtt{vn}_3(1 - d_A)^2 - V_N\right) \end{bmatrix},$$

$$\mathbf{G}_C(\mathbf{x}) = \begin{bmatrix} i + \Delta\mathtt{i}_1 d_A - \Delta\mathtt{i}_3 d_{AB} + \Delta\mathtt{i}_4 (1 - d_B) \\[2mm] vp + \Delta\mathtt{vp} + \delta\mathtt{vp}_2(1 - d_B) \\[2mm] vn + \Delta\mathtt{vn} + \delta\mathtt{vn}_1 d_{AB} - \delta\mathtt{vn}_2(1 - d_B) \\[2mm] \sigma p + \dfrac{T}{\tau_P}\left(vp + \dfrac{\Delta\mathtt{vp}}{2} + \delta\mathtt{vp}_4(1 - d_B)^2 - V_P\right) \\[2mm] \sigma n + \dfrac{T}{\tau_N}\left(vn + \dfrac{\Delta\mathtt{vn}}{2} + \delta\mathtt{vn}_5 d_{AB} - \delta\mathtt{vn}_4(1 - d_B)^2 - V_N\right). \end{bmatrix}.$$

Finally, the duty cycles are given by

$$d_A = \frac{(V_U + g_{PA}(V_P - vp - \sigma p) + g_{NA}(vn - V_N + \sigma n))/r_S - i}{\Delta\mathtt{i}_1 - \Delta\mathtt{ir}}$$

and

$$d_B = \frac{(V_U + g_{PB}(V_P - vp - \sigma p) + g_{NB}(vn - V_N + \sigma n))/r_S - (i + (\Delta\mathtt{i}_1 - \Delta\mathtt{i}_3)d_A)}{\Delta\mathtt{i}_3 - \Delta\mathtt{ir}}.$$

Bibliography

[1] A. A. Andronov, S. E Khaikin, and A. A. Vitt. *Theory of oscillators.* Pergamon Press, 1965.

[2] F. Angulo, E. Fossas, and G. Olivar. Transition from periodicity to chaos in a pwm-controlled buck converter with zad strategy. *International Journal of Bifurcation and Chaos*, 15(10):3245–3264, 2005.

[3] V. Avrutin and M. Schanz. Border-collision period doubling scenario. *Physical Review E*, 70(2):026222, Aug 2004.

[4] V. Avrutin and M. Schanz. Period-doubling scenario without flip bifurcations in a one-dimensional map. *International Journal in Bifurcation and Chaos*, 15:1267–1284, 2005.

[5] V. Avrutin, M. Schanz, and S. Banerjee. Multi-parametric bifurcations in a piecewise-linear discontinuous map. *Nonlinearity*, 19(3):1875–1906, 2006.

[6] J. Baillieul, R. W. Brockett, and R. B. Washburn. Chaotic motion in nonlinear feedback systems. *IEEE Transactions on Circuits and Systems*, 27:990–997, 1980.

[7] S. Banerjee. Robust chaos. *Physics Review Letters*, (80):3049–3052, 1998.

[8] S. Banerjee and K. Chakrabarty. Nonlinear modeling and bifurcations in the boost converter. *IEEE Transactions on Power Electronics*, 13(2):252–260, 1998.

[9] S. Banerjee and C. Grebogi. Border collision bifurcations in two-dimensional piecewise smooth maps. *Physics Review E*, (59):4052–4061, 1999.

[10] S. Banerjee, M. S. Karthik, G. H. Yuan, and J. A. Yorke. Bifurcations in one-dimensional piecewise smooth maps-theory and applications in switching circuits. *IEEE Transactions on Circuits and Systems I*, 47(3):389–394, 2000.

[11] S. Banerjee and G. C. Verghese. *Nonlinear Phenomena in Power Electronics: Bifurcations, Chaos, Control, and Applications.* Wiley-IEEE Press, New York, 2001.

[12] R. Barabás, B. Buti, J. Hamar, and I. Nagy. Control characteristics, simulation and test results of a dual channel dc-dc converter family. In *Power Electronics Electrical Drives Automation and Motion Conference (SPEEDAM'04)*, Capri, Italy, 16-18 June 2004.

[13] L. Benadero, A. El Aroudi, G. Olivar, E. Toribio, and E. Gómez. Two-dimensional bifurcation diagrams background pattern of fundamental dc-dc converters with pwm control. *International Journal of Bifurcation and Chaos*, 13(2):427–451, 2003.

[14] L. Benadero, R. Giral, A. El Aroudi, and J. Calvente. Stability analysis of a single inductor dual switching dc-dc converter. *Mathematics and Computers in Simulation*, 71(4):256–269, 2006.

[15] L. Benadero, V. Moreno-Font, A. El Aroudi, and R. Giral. Single inductor multiple outputs interleaved converters operating in ccm. In *Proc. 13th Power Electronics and Motion Control Conference (EPE-PEMC'8)*, Poznan, Poland, 2008.

[16] R. W. Brockett and J. R. Wood. Understanding power converter chaotic behavior mechanisms in protective and abnormal modes. In *Proceedings of 11th Annual International Power Electronics Conference (Powercon'84)*, pages E–14–E–15, Dallas, USA, 1984.

[17] B. Brogliato. *Impacts in mechanical systems: analysis and modelling.* Springer-Verlag, 1999.

[18] B. Brogliato. *Nonsmooth Mechanics: Models, dynamics and control.* Springer-Verlag, 1999.

[19] B. Buti, I. Nagy, and E. Masada. Stability analysis of pwm-controlled dual channel resonant buck & boost converter using pi controller. In *12th International Power Electronics and Motion Control Conference*, volume 1, pages 869–876, 2006.

[20] J. Calvente, F. Ginjoan, L. Martínez-Salamero, and A. Poveda. Subharmonics bifurcations and chaos in a sliding mode controlled boost switching regulator. In *International Symposium on Circuits and Systems (ISCAS'96)*, pages 573–576, Atlanta, USA, 1996.

[21] V. Carmona, E. Freire, E. Ponce, and F. Torres. On simplifying and classifying piecewise linear systems. *IEEE Transactions on Circuits and Systems I: Fundamental Theory and Applications*, (49):609–420, 2002.

[22] V. Carmona, E. Freire, E. Ponce, and F. Torres. The continuous matching of two stable linear systems can be unstable. *Discrete and continuous dynamical systems*, 16(3):689–703, 2006.

[23] K. W. E. Cheng, M. Liu, and J. Wu. Chaos study and parameter space analysis of dc-dc buck-boost converter. *IEEE Proceedings Electronic Power Applications*, 150(2):126–138, 2003.

[24] L. O. Chua. Special issue on chaos in electronic systems; contains many tutorial and description articles for the non-specialists. *Proceedings IEEE*, 75(8), 1987.

[25] H. Dankowicz and A. B. Nordmark. On the origin and bifurcations of stick-slip oscillations. *Phys. D*, 136:280–302, 1999.

[26] J. H. B. Deane and D. C. Hamill. Analysis, simulation and experimental study of chaos in the buck converter. In *IEEE Power electronics Specialist Conferences (PESC'90)*, pages 491–498, Texas, 1990.

[27] J. H. B. Deane and D. C. Hamill. Instability, subharmonic and chaos in power electronic systems. *IEEE Transactions on Power electronics*, 5(3):260–268, 1990.

[28] K. Deimling. *Multivalued Differential Equations*. Walter de Gruyter, 1992.

[29] M. di Bernardo, C. Budd, A. Champenys, and B. Kowalczyk. *Piecewise-Smooth Dynamical Systems: Theory and Applications*. Springer-Verlag, 2008.

[30] M. di Bernardo, C.J Budd, A. R. Champneys, P. Kowalczyk, A. B. Nordmark, G. Olivar, and P. T. Piiroinen. Bifurcations in nonsmooth dynamical systems. *SIAM Review*, 50(4):629–701, 2008.

[31] M. di Bernardo, M.I. Feigen, S.J. Hogan, and M.E. Homer. Local analysis of c-bifurcations in n-dimensional piecewise smooth dynamical systems. *Chaos, Solitons and Fractals*, 11(10):1881–1908, 1999.

[32] M. di Bernardo, F. Garofalo, L. Glielmo, and F. Vasca. Switchings, bifurcations and chaos in dc/dc converters. *IEEE Transactions on Circuits and Systems I: Fundamental Theory and Applications*, 45(2):133–141, 1998.

[33] M. di Bernardo, F. Garofalo, L. Ianelli, and F. Vasca. Bifurcations in a piecewise-smooth feedback systems. *International J. Control*, 75:1243–1259, 2002.

[34] M. di Bernardo and C. K. Tse. *Chaos in power electronics: An overview*, volume 11, chapter 16, pages 317–340. World Scientific, June 2002.

[35] M. di Bernardo and F. Vasca. Discrete-time maps for the analysis of bifurcations and chaos in dc/converters. *IEEE Transactions on Circuits and Systems I*, 47(2):130–173, 2000.

[36] I. Dénes and I. Nagy. Two models for the dynamic behavior of a dual-channel buck and boost dc-dc converter. *Electromotion*, 10(4):556–561, 2003.

[37] P. S. Dutta, B. Routroy, S. Banerjee, and S. S. Alam. On the existence of low-period orbits in n-dimensional. *Nonlinear Dynamics*, 53:369–380, 2008.

[38] A. El Aroudi, M. Debbat, G. Olivar, L. Benadero, E. Toribio, and R. Giral. Bifurcations in dc-dc switching converters: Review of methods and applications. *International Journal of Bifurcation and Chaos*, 15(5):1549–1578, 2005.

[39] A. El Aroudi, M. B. Debbat, R. Giral, and L. Martínez-Salamero. Stability analysis and bifurcations of switching regulators with pi and sliding mode control. In *10th International Power Electronics and Motion Control Conference (EPE-PEMC'02)*, Dubrovnik, Croatia, 2002.

[40] A. El Aroudi, V. Moreno, and L. Benadero. Nonsmooth pitchfork bifurcation in a dc-dc converter: coexisting attractors and intermittency. In *6th International Multi-Conference on Systems, Signals and Devices*, Djerba, Tunisia, 2009.

[41] A. El Aroudi, V. Moreno-Font, and L. Benadero. Dynamical analysis of an interleaved single inductor tito switching regulator. *Mathematical Problems in Engineering*, 2009(Article ID 946245):19 pages, 2009.

[42] A. El Aroudi, B. G. M. Robert, A. Cid-Pastor, and L. Martínez-Salamero. Modeling and design rules of a two-cell buck converter under a digital controller. *IEEE Transactions on Power Electronics*, 23(2):859–870, 2008.

[43] R. W. Erickson and D. Maksimovic. *Fundamentals of Power Electronics*. Springer, 2001.

[44] M. I. Feigin. Doubling of oscillation period with c-bifurcations in piecewise continuous systems (in russian). *Prikladnaya Matematika i Mekhanika*, 34:861–869, 1970.

[45] M. I. Feigin. On the generation of sets of subharmonics in a piecewise continuous system (in russian). *Prikladnaya Matematika i Mekhanika*, 38:810–818, 1974.

[46] M. I. Feigin. On the structure of c-bifurcation boundaries of piecewise continuous system (in russian). *Prikladnaya Matematika i Mekhanika*, 42:820–829, 1978.

[47] M. I. Feigin. Forced oscillations in systems with discontinuous nonlinearities. *Nauka, Moscow*, 38:810–818, 1994.

[48] A. F. Filippov. *Differential equations with discontinuous righthand sides*. Kluwer Academic Publishers, 1988.

[49] E. Fossas and G. Olivar. Study of chaos in the buck converter. *IEEE Transactions on Circuits and Systems I: Fundamental Theory and Applications*, 43(1):13–25, 1996.

[50] E. Freire, E. Ponce, F. Rodrigo, and F. Torres. Bifurcation sets of continuous piecewise linear systems with two zones. *International Journal Bifurcation and Chaos*, (8):2073–2097, 1998.

[51] D. Giaouris, S. Banerjee, B. Zahawi, and V. Pickert. Stability analysis of the continuous-conduction-mode buck converter via filippov's method. *IEEE Transactions on Circuits and Systems I: Regular Papers*, 2008.

[52] R. Giral, J. Calvente, R. Leyva, A. El Aroudi, G. Arsov, and L. Martinez-Salamero. Symmetrical power supply for 42 v automotive applications. *Facta universitatis (NIS) Ser., Elec. Energ.*, 17:363–374, 2004.

[53] J. Hamar and I. Nagy. Asymmetrical operation of dual channel resonant dc-dc converters. *IEEE Transactions on Power electronics*, 18(1):83–94, 2003.

[54] J. Hamar, I. Nagy, P. Stumpf, H. Ohsaki, and E. Masada. New dual channel quasi resonant dc-dc converter topologies for distributed energy utilization. In *13th International Power Electronics and Motion Control Conference*, volume 1, pages 1778–1785, 2008.

[55] J. Hamar, Z. Suto, and I. Nagy. Signal processing by mutimedia in nonlinear dynamics and power electronics: review. *Transactions on engineering, computing and technology*, 13:34–44, 2006.

[56] D. C. Hamill and D.J. Jefferies. Subharmonics and chaos in a controlled switched-mode power converter. *IEEE Transactions on Circuits and Systems I*, 35(8):1059–1061, 1988.

[57] W. Heemels and B. Brogliato. The complementarity class of hybrid dynamical systems. *European J. Control*, 9:311–319, 2003.

[58] S. J. Hogan, L. Higham, and T. C. L. Griffin. Dynamics of a piecewise linear map with a gap. *Proc. R. Soc. A*, 463:49–65, 2006.

[59] Y. Huang, H. H. C. Iu, and C. K. Tse. Boundaries between fast- and slow-scale bifurcations in parallel-connected buck converters. *Int. J. Circ. Theor. Appl.*, 2008.

[60] H. H. C. Iu and C. K. Tse. Bifurcation behavior in parallel-connected buck converters. *IEEE Transactions on Circuits and Systems I: Fundamental Theory and Applications*, 48(2):233–240, 2000.

[61] H. H. C. Iu and C. K. Tse. Study of low-frequency bifurcation behavior phenomena of parallel-connected buck converter via simple averaged models. *IEEE Transactions on Circuits and Systems I: Fundamental Theory and Applications*, 50(5):679–686, 2003.

[62] A. Cellina J. Aubin. *Differential Inclusions, Set-Valued Maps And Viability Theory*. Springer - Verlag, 1984.

[63] D. J. Jefferies, J. H. Deane, and G. G. Johnstone. An introduction to chaos. *Electronics and Communication Journal*, pages 115–123, 1989.

[64] J. G. Kassakian, M. Schlecht, and G. C. Verguese. *Principles of power electronics.* Addison-Wesley, 1991.

[65] J. P. Keener. Chaotic behaviour in piecewise continuous difference equations. *Trans. American Mathematical Society*, 261:589–604, 1980.

[66] J. P. Keener and J. Sneyd. *Mathematical physiology.* Springer-Verlag, 1998.

[67] W. H. Ki and D. Ma. Single-inductor multiple-output switching converters. In *Power Electronics Specialists Conference (PESC)*, volume 1, pages 226–231, 16-18 June 2001.

[68] L. E. Kollar, G. Stepan, and J. Turi. Dynamics of piecewise linear discontinuous maps. *International Journal of Bifurcations and Chaos*, 14:2341–3351, 2004.

[69] P. T. Krein. *Elements of Power electronics.* Oxford University Press, 1998.

[70] P. T. Krein and R. M. Bass. Multiple limit cycle phenomena in switching power converters. In *IEEE Applied Power Electronic Conference*, pages 143–148, 1990.

[71] P. T. Krein and R. M. Bass. Types of instability encountered in simple power electronic circuits: Unboudness, chattering and chaos. In *IEEE Applied Power Electronic Conferences Record (APEC'90)*, pages 191–194, 1990.

[72] M. Kunze. *Non-smooth dynamical systems.* Lecture Notes in Math. 1744, Springer-Verlag, 2000.

[73] Y. Kuznetsov, S. Rinaldi, and A. Gragnani. One-parameter bifurcation in filippov systems. *International Journal in Bifurcation and chaos*, 13:2157–2188, 2003.

[74] Y. A. Kuznetsov. *Elements of applied bifurcation theory.* Springer, 2004.

[75] H. P. Le, C. S. Chae, K. C. Lee, S. W. Wang, and G. H. A Cho. Single-inductor switching dc-dc converter with five outputs and ordered power-distributive control. *IEEE Journal of Solid-State Circuits*, 47(12):2706–2714, 2007.

[76] R. Leine and H. Nijmeijer. *Dynamics and bifurcations of non-smooth dynamical systems.* Lect. Notes Appl. Comput. Mech. 18, Springer-Verlag, 2004.

[77] T. LoFaro. Period-adding bifurcations in a one parameter family of interval maps. *Math. Comput. Modell.*, 24:27–41, 1996.

[78] D. Ma, W. H. Ki, and C. Y. Tsui. A pseudo-ccm/dcm simo switching converter with freewheel switching. *IEEE Journal of Solid-State Circuits*, 38(6):1007–1014, 2003.

[79] D. Ma, W. H. Ki, C. Y. Tsui, and P. K. T. Mok. A 1.8 v single-inductor dual-output switching converter for power reduction techniques. *Symposium on VLSI Circuits Digest of Technical Papers*, pages 137–140, 2001.

[80] D. Ma, W. H. Ki, C. Y. Tsui, and P. K. T. Mok. Single-inductor multiple-output switching converters with time-multiplexing control in discontinuous conduction mode. *IEEE Journal of Solid-State Circuits*, 38(1):89–100, 2003.

[81] S. K. Mazumder, A. H. Nayfeh, and D. Boroyevich. A nonlinear approach to the analysis of stability and dynamics of standalone and parallel dc-dc converters. In *Proceedings of IEEE applied Power Electronics Conference and Exposition*, pages 784–790, 2001.

[82] R. D. Milddlebrok and S. Ćuk. A general unified approach to modelling switching-converter power stages. *IEEE Power Electronics Specialists Conference Record*, pages 18–34, 1976.

[83] N. Mohan, T. M. Undeland, and W. P. Robins. *Power Electronics: Converters, Applications and Design*. John Wiley & Sons, 2003.

[84] V. Moreno and L. Benadero. Investigating stability of a single inductor current mode controlled dual switching dc-dc converter. In *11th European Conference on Power Electronics and Applications*, Dresden, Germany, 11-14 September 2005.

[85] V. Moreno, L. Benadero, A. El Aroudi, R. Giral, and J. Calvente. Three dimensional discrete map for a single inductor current mode controlled dual switching dc-dc converter. In *12th International Power Electronics and Motion Control*, pages 2008–2013, Portoroz, Slovenia, 2006.

[86] V. Moreno-Font, L. Benadero, and A. El Aroudi. Pws maps of interleaved single-inductor multiple-input multiple-output dc-dc converter. In preparation, 2009.

[87] V. Moreno-Font, M. di Bernardo, and L. Benadero. Border-collision bifurcations in a three-pieces linear map. In *Nolineal*, Barcelona, Spain, 16-19 June 2008.

[88] V. Moreno-Font, A. El Aroudi, L. Benadero, R. Giral, and J. Calvente. Dynamics and stability issues of a single inductor dual switching dc-dc converter. IEEE Transactions on Circuits and Systems I. In press, 2009.

[89] H. E. Nusse and J. A Jorke. Border collisions bifurcations including period-two to period-three for piecewise smooth systems. *Physics D*, (57):39–57, 1992.

[90] H. E. Nusse and J. A Jorke. Border collisions bifurcations for piecewise smooth one-dimensional maps. *International Journal Bifurcation and Chaos*, (5):189–207, 1995.

[91] H. E. Nusse, E. Ott, and J. A Jorke. Border collisions bifurcations: An explanation for observed bifurcation phenomena. *Physics Review Letter E*, (49):1073–1076, 1994.

[92] G. Olivar, M. di Bernardo, and F. Angulo. Discontinuous bifurcations in dc-dc converters. In *Proceedings of IEEE International Conference on Industrial Technology (ICIT)*, 2003.

[93] S. Banerjee P. Jain. Border collision bifurcations in one-dimensional discontinuous maps. *International Journal of Bifurcations and Chaos*, 13:3341–3351, 2003.

[94] S. Parui and S. Banerjee. Border collision bifurcations at the change of the state-space dimension. *Chaos*, (12):1054–1069, 2002.

[95] P. Patra, S. Samanta, A. Patra, C. Amit, and S. Chattopadhyay. A novel control technique for single-inductor multiple-output dc-dc buck converters. *IEEE Int. Conf. on Industrial Technology*, pages 807–811, 2006.

[96] F. Peterka. Part 1: Theoretical analysis of n-multiple (1/n)-impacts solutions. *CSAV Acta Technica*, 19:462–473, 1974.

[97] S. X. Qu, S. Wu, and D. R. He. A multiple devils staircase in a discontinuous map. *Phys. Lett. A*, 231:152–158, 1997.

[98] S. X. Qu, S. Wu, and D. R. He. Multiple devils staircase and type-v intermittency. *Phys. Rev. E*, 57:402–411, 1998.

[99] B. Robert and A. El Aroudi. Discrete time model of a multi-cell dc/dc converter: Non linear approach. *Mathematics and Computers in Simulation*, 71(4):310–319, 2006.

[100] A. Sharma and Y. S. Pavan. A single inductor multiple output converter with adaptive delta current mode control. *IEEE Int. Symposium on Circuits and Systems*, pages 5643–5646, 2006.

[101] Z. T. Zhusubaliyev E. Soukhoterin and E. Mosekilde. Border collisions bifurcations on a two-dimensional torus. *Chaos Solitons and Fractals*, (13):1889–1915, 2003.

[102] Z. Suto and I. Nagy. Recurrence plot based study of direct torque controlled induction machines. In *Chaos (IFAC)*, 2006.

[103] D. Trevisan, P. Mattavelli, and P. Tenti. Digital control of single-inductor multiple-output step-down dc-dc converters in ccm. *IEEE Transactions on Industrial Electronics*, 55(9):3476–3483, 2008.

[104] D. Trevisan, W. Stefanutti, P. Mattavelli, and P. Tenti. Fpga control of simo dc-dc converters using load current estimation. In *32nd Annual Conf. of IEEE Industrial Electronics Society*, pages 2243–2248, 2005.

[105] C. K. Tse. Chaos from a buck switching regulator operating in discontinuous mode. *International Journal of Circuit Theory and Applications*, 22:263–278, 1994.

[106] C. K. Tse. Flip bifurcation and chaos in three-state boost switching regulators. *IEEE Transactions on Circuits and Systems I*, 41:16–23, 1994.

[107] C. K. Tse and M. di Bernardo. Complex behavior in switching power converters. *Proceedings IEEE*, 90(5):768–781, 2002.

[108] V. I. Utkin. *Sliding Modes in Control Optimization*. Springer, 1992.

[109] S. Wiggins. *Introduction to applied nonlinear dynamical systems and chaos*. Springer-Verlag, 2on edition edition, 2003.

[110] Y. Xi and P.K. Jain. A forward converter topology with independent and precisely regulated multiple outputs. *IEEE Transactions on Power Electronics*, 18(2):648–658, 2003.

[111] G. Yuan, S. Banerjee, E. Ott, and J.A Jorke. Border-collision bifurcations in the buck converter. *IEEE Transactions on Circuits and Systems I: Fundamental Theory and Applications*, 45(7):707–716, 1998.

[112] Z. T. Zhusubaliyev and E. Mosekilde. *Bifurcation and chaos in piecewise-smooth dynamical systems*. World Scientific, 2003.

[113] Z. T. Zhusubaliyev, E. A. Soukhoterin, and E. Mosekilde. Quasi-periodicity and border-collision bifurcations in a dc-dc converter with pulsewidth modulation. *IEEE Transactions On Circuits And Systems I*, 50(8):1047–1057, 1998.